UC Riverside
UC Riverside Electronic Theses and Dissertations

Title

Biophotovoltaic System Built From Renewable Carbon: Integration of Graphene Hybrids and the Phototrophic Protein Bacteriorhodopsin

Permalink

https://escholarship.org/uc/item/26s4m8br

Author

Chaves Villarreal, Claudia Maria

Publication Date

2018

Copyright Information

Peer reviewed|Thesis/dissertation

UNIVERSITY OF CALIFORNIA
RIVERSIDE

Biophotovoltaic System Built From Renewable Carbon: Integration of
Graphene Hybrids and the Phototrophic Protein Bacteriorhodopsin

A Dissertation submitted in partial satisfaction
of the requirements for the degree of

Doctor of Philosophy

in

Materials Science and Engineering

by

Claudia M. Chaves Villarreal

December 2018

Dissertation Committee:
     Dr. Ashok Mulchandani, Chairperson
     Dr. Juchen Guo
     Dr. Alfredo Martinez

The Dissertation of Claudia M. Chaves Villarreal is approved:

Committee Chairperson

University of California, Riverside

Acknowledgments

overcome the difficult challenges that graduate school poses in the physical and emotional health of any

student.

DEDICATION

Dedicated to Pachamama, our mother Earth to whom we all belong

Dedicated to my parents Luz Marina Villarreal Vargas and Manuel Ángel Chaves Trejos

ABSTRACT OF THE DISSERTATION

Biophotovoltaic System Built From Renewable Carbon: Integration of Graphene Hybrids and the Phototrophic Protein Bacteriorhodopsin

by

Claudia M. Chaves Villarreal

Doctor of Philosophy, Graduate Program in Materials Science and Engineering
University of California, Riverside, December 2018
Dr. Ashok Mulchandani, Chairperson

Solar energy has the highest potential of the Earth´s renewable energy sources. Its conversion into electrical power to meet the demand of our economy is an ongoing effort. The leading technology, silicon, and the emerging alternative technologies, like CdTe and perovskites, require energy intensive manufacturing processes, toxic chemicals and/or non-abundant minerals that cause problems thorough their life cycle such as pollution and social conflicts. **Since the negative impacts of PV technology are mainly derived from material selection and manufacturing processes, new advanced technology that uses abundant, renewable and biodegradable materials, as well as cleaner fabrication processes needs to be developed for the sustainable future of solar energy.** Carbon is an abundant element that exhibits a broad assortment of allotropic forms and electrical behavior, and can make up an infinite variety of functional biomolecules when combined with other plentiful elements. We propose the combination of graphene-ZnO hybrids with a phototrophic protein, bacteriorhodopsin (bR), to develop a bio-sensitized solar cell. The graphene is used to replace the tin oxide transparent conductor in the photanode, while the bR is used to replace the traditional synthetic dyes that absorb the visible sunlight. Two different morphologies and fabrication approaches of nano-ZnO are investigated to create graphene heterostructures for photoanode platform: commercial nanoparticles and vertical nanorods *in situ* grown by electrodeposition. The immobilization of the bR on the
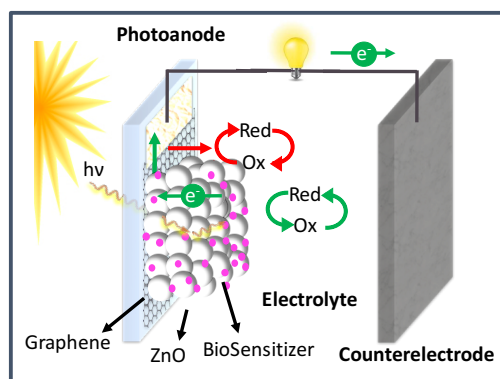
ZnO and the mediator selection are optimized in function of the photoelectric response of the system. We investigate the structure, energy alignment and electrical behavior at the different interfaces of the device, graphene/ZnO/bR/electrolyte, and correlate them to processing parameters. The photovoltaic performance, internal resistance and electron kinetics of the cells are characterized by photo-electrochemical methods. The introduction of heterostructures using carbon nanomaterials and biomolecules derived from renewable sources together with low cost, non-toxic semiconductors constitute the beginning of a new era for sustainable bio-photovoltaics, which is supported by the latest advances in genetic engineering and nanotechnology. This work demonstrates the viability of sustainable alternatives to replace traditional costly and harmful materials and provides a framework to the design of novel bio-nanointerfaces for future technological applications.

RESUMEN

La energía solar presenta el mayor potencial entre las fuentes de energía renovable en el planeta Tierra. Por ello, su conversión a energía eléctrica para suplir la demanda de nuestra economía es una esfuerzo continuo. La tecnología que predomina actualmente, el silicio, y las tecnologías alternativas emergentes, como el CdTe y las perovskitas, requieren consumo intensivo de energía, sustancias tóxicas y materiales poco abundantes para su manufactura, que generan problemas a lo largo de su ciclo de vida como contaminación y conflictos sociales. Ya que los impactos negativos de la tecnología fotovoltaica se derivan principalmente de la selección de materiales y su manufactura, es necesario el desarrollo de nuevas tecnologías avanzadas que utilicen materiales abundantes, renovables y biodegradables, así como procesos de manufactura más limpios para asegurar un futuro sostenible de la energía solar. El carbono es un elemento abundante que exhibe una amplia diversidad de formas alotrópicas y propiedades eléctricas, y puede constituir una variedad infinita de biomoléculas funcionales cuando se combina con otros elementos abundantes. En este trabajo se propone combinar materiales híbridos de grafeno y ZnO con la proteína

fototrófica bacteriorhodopsina (bR) para desarrollar una celda solar bio-sensibilizada. El grafeno reemplaza los conductores transparentes tradicionales basados en óxido de estaño y la bR reemplaza los colorantes sintéticos tradicionales que absorben la luz visible del sol. Se comparan dos morfologías de nano-ZnO que se sintetizan con métodos distintos: nanopartículas comerciales y nanobarras por electrodeposición in situ. La inmobilización de la bR en el ZnO y el diseño del electrolito se estudian para optimizar la función fotoeléctrica del dispositivo. Investigamos la estructura, la alineación de los niveles energéticos y el comportamiento eléctrico en cada una de las interfaces de dispositivo, grafeno/ZnO/bR/electrolito, y se correlacionan a los parámetros del proceso. El desempeño fotovoltaico, la resistencia interna y la cinética de las cargas eléctricas de los dispositivos se caracterizan por métodos foto-electroquímicos. La introducción de estructuras compuestas que utilizan nanomateriales de carbono y biomoléculas derivadas de recursos renovables, así como semiconductores no tóxicos de bajo costo, constituye el inicio de una nueva era para la tecnología bio-fotovoltaica sostenible, que se apoya en los avances más reciente en ingeniería genética y nanotecnología.Este trabajo demuestra la viabilidad de alternativa sostenibles para reemplazar los materiales tradicionales costosos y dañinos, y provee un marco de trabajo para el diseño de nuevas bio-nanointerfaces para futuras aplicaciones.

Table of Contents

Table of Figures

Introduction

Chapter I

Chapter II

Chapter III

List of Tables

Introduction:

The Route to Biophotovoltaic Systems Using Renewable Carbon

1.1. Impacts of Current Photovoltaic Technology on the Environment and Human Life

Environmental pollution and climate disruption caused by anthropogenic increase of greenhouse gases (GHG) are two challenges that threaten the stability of human society, and have been largely caused by energy generation since the industrial revolution[1]. Solar energy is the most abundant and sustainable energy source for humanity, reaching the Earth in a reliable and distributed way at a rate of ~120,000 TW, significantly higher than the current worldwide energy consumption of ~15 TW-year[2,3]. Despite of the great potential of photovoltaics (PV) energy generation to avoid GHG by replacing fossil fuels, current technologies face many challenges and pose negative impacts to the environment and human life. The first stages in the life cycle of commercial and emerging PV technologies, mining, extraction and refining, are especially problematic, because they are very energy intensive and cause significant pollution, for example, from the use of 2,4,6-Trinitrotoluene (TNT), a toxic and recalcitrant chemical considered a priority for removal from polluted sites by the US Environmental Protection Agency [4,5].

Si technology, also called first generation PV, continues to dominate the current market, as illustrated in **Figure 1.1 (a)**. Si PV account for 94.7% of the global annual production of 2016 in terms of nominal power, whether mono- or polycrystalline, and in very small percentage amorphous[6]. According to life cycle assessment, the GHG emissions from silicon PV technology are notably lower than the use of fossil fuels, but are still larger than other renewable energy sources like wind, hydroelectric and biomass, as illustrated in **Figure 1.1 (b)**. The time to recover the total energy invested and the GHG emissions of Si PV currently manufactured ranges from 1.5 to 15.5 years, with more than 85% occupied by the manufacturing of the cells and ~40% corresponding exclusively to solar grade silicon production [7,8]. The tenth position in terms

of global environmental impact amongst all metallurgical mining and refining processes is occupied by Si [9].

Older Si PV manufacturing technologies and scale resulted in even lower energy usage efficiency. For the above reasons, the global PV installations made for last 40 years are barely starting to avoid GHG emissions today, as they have been mostly paying back for the emissions caused by their manufacturing during all these years[10].

(a)

(b)
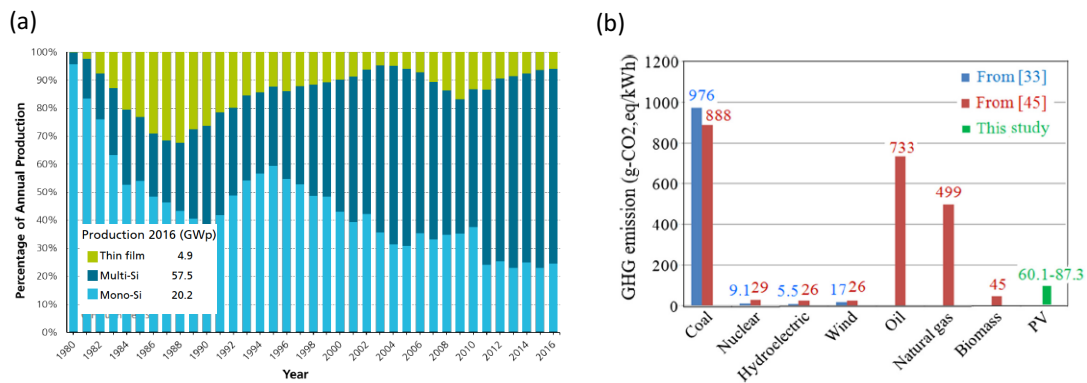
Figure 1.1. **(a) Percentage of Global Annual PV Production by Technology (ISE)[6]. (b) Comparison of life cycle GHG emissions of various power sources. PV life-cycle assessment done with average data of state-of-the-art crystalline Si systems produced and installed in China [7], Reprinted from Applied Energy, Vol 164, Hou, G *et al*., Life cycle assessment of grid-connected photovoltaic power generation from crystalline silicon solar modules in China, 882-890, Copyright 2016, with permission from Elsevier**

Thin film PV technology, also known as second generation PV, accounts for the remaining 5.3% annual production, comprised by Cd-Te and CI(G)S[6]. A wide variety of emergent PV technologies, i.e. third generation PV, are being investigated, including organic, multi-junction and sensitized solar cells. Mining of heavy metals like Cu, Sn, Pb, Te, Ru and Cd used in second and third generation PV causes pollution of water and soil, increasing the health risks of workers and the exposure of surrounding communities to toxic compounds, for example by consumption of edible plants [11-13]. Trace metals from historical mining sites have been demonstrated to remain bioavailable even centuries after their emission [14]. Furthermore, these activities are in many cases linked to social problems and political conflicts in areas where they are held, such as the financing of terrorist groups in Democratic Republic of Congo [15]. A special mention must be given to perovskites which appeared only a couple of years ago and have experienced the fastest power

2

conversion efficiency (PCE) improvement in the last years [16, 17]. However, perovskites have raised much controversy due to the presence of lead, a heavy metal pollutant for which many efforts have been directed to eliminate from consumer products[18].

Another concerning aspect of PV cells containing heavy metals, petrochemicals, toxic or non-biodegradable compounds is their release to the environment as hazardous waste once the device reaches the end of its life cycle. Because of their extended lifetime and relative recent incorporation of the technology to the market, PV waste has not become a significant component of the waste stream yet. However, their destiny as electronic waste (e-waste) is very discouraging. Most e-waste produced in the US is currently being shipped illegally to developing regions of Asia and Africa where the technology for properly managing their hazardous compounds does not exist. As a result, waste mining for valuable metals like gold results in an alarming pollution and health issues in those regions.

Considering that the negative impacts of PV technology are mainly derived from material selection and manufacturing processes, **new advanced technology that uses abundant, renewable and biodegradable materials, as well as cleaner processing needs to be developed for the sustainable future of solar energy conversion**.

1.2. Sensitized Solar Cells and the Promise of Greener and Affordable Photovoltaics

During the years between of 1968-1990, much interest was payed to the development of photoelectrochemical cells, composed of a semiconducting photoanode and a metal counter electrode connected via a solution of redox system and supporting electrolyte. The development of photoelectrochemical cells was triggered by the discovery of the Honda-Fujishima effect, i.e. water splitting on the surface of illuminated TiO_2[19]. Sensitization, i.e the use of photoactive molecules to expand the absorbance range of semiconductors like TiO_2, ZnO and CdS, was studied in fully aqueous electrolytes during that time[20-22]. The introduction of high surface area-electrodes using sintered ZnO powders[23] and

carboxylated bipyridine complex of Ru(II) as a sensitizer[24] lead to PCE improvements in these cells. The

sensitized solar cell (SC) as a third generation PV technology we know today is attributed to the report of

Grätzel in 1991[25]. Their milestone PCE of 12% was achieved by using a ruthenium tris(bipyridine) dye as

sensitizer and aprotic organic solvents with I^-/I_3^- redox mediator in the electrolyte. Because the first

sensitizers used were dyes, the common term dye-sensitized solar cell (DSC) was initially coined.

The SC structure is illustrated in **Figure 1.2(a)**. The photoanode, on which we will center our attention,

is based on a sensitizer, immobilized on the surface of a nanostructured wide-bandgap semiconductor,

usually TiO_2 or ZnO nanoparticles (NPs), spread on a transparent conductor (TC) such as fluorine-doped tin

oxide (FTO). The limited solar spectrum range that ZnO or TiO_2 absorbs in the UV is expanded by sensitizing

the photoanodes with photoactive materials that absorb in the visible range of the sun spectrum, such as

organic and metalorganic dyes [26] quantum dots [27], plasmonic nanoparticles [28], perovskites [17, 29] and

photosynthetic biomolecules [30, 31]. The sensitizer absorbs light and its electrons are excited from the highest

occupied molecular orbital (HOMO) into its lowest unoccupied molecular orbital (LUMO), as illustrated in

the energy level diagram in **Fig.1.2(b)**. From there, the electron is injected into the conduction band of the

semiconductor and finally transferred into the TC. The sensitizer is regenerated by the oxidation of the

redox mediator in the electrolyte, such as the I^-/I_3^- pair, and the charge transfer cycle is completed with the

mediator reduction in the counter electrode. The maximum open circuit voltage is the difference between

the Fermi level of the semiconductor and the redox potential of the mediator. The PCE of the device relies

critically on the kinetic competition of the forward processes (green arrows in **Figure 1.2(a)**) and the

recombination reactions (red arrows in **Figure 1.2(a)**), since both paths are thermodynamically allowed for

the charges. To date, the highest PCE achieved in DSC has been 13% [26].
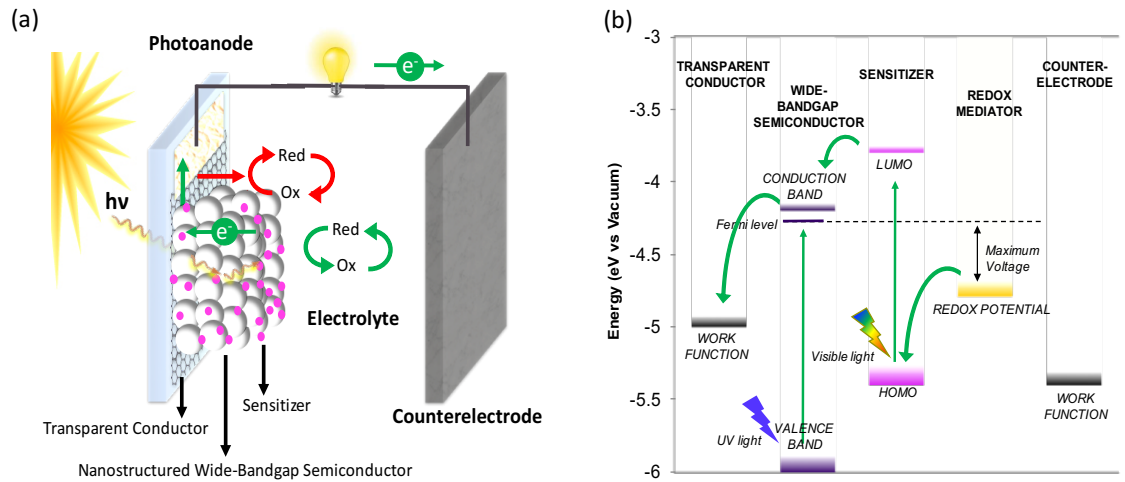
Figure 1.2.   (a) Schematics of a SC (b) energy levels in the SC

Some of the advantages of SCs are that they have good performance under diffuse light conditions[32], they can be made flexible for portable and rollable applications[33] and transparent to be used as windows in buildings[34]. Most importantly, their manufacturing consumes significant lower energy than Si PV, which results in reduction of cost and GHG emissions. The semiconductor is an oxide that does not need to be reduced or to have high crystallinity, and it is deposited using well-known thick film techniques, like spraying and screen-printing. Second generation PV technologies have production costs below $1/W_{peak}, therefore, emerging technologies need to aim at production costs below $0.5/W_{peak} to be competitive for large-scale electricity production, a milestone that SC technology has the potential to achieve [35, 36]. As illustrated in **Fig.1.3**, DSSCs have one of the lowest average GHG emissions amongst PV technologies, outranked only by CdTe technology[37], which has drawbacks as it is composed by Cd, one of the heavy metals with the highest toxicity, environment mobility and bioconcentration factor[38, 39].
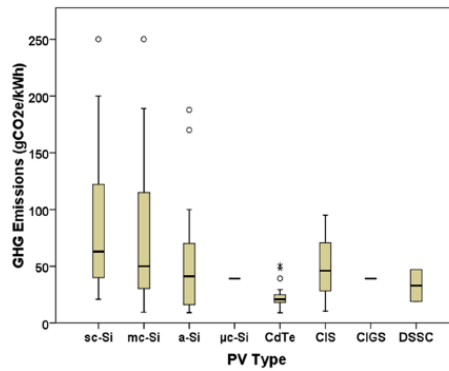
Figure 1.3. GHG emissions from PV electricity generation systems by [Kommalapati, R.](#) is licensed under CC BY 2.0 [CC by 4.0](#) [37]

Some improvements to make SCs cheaper, safer and more sustainable are: replacement of tin oxides as TCs[40], replacement of volatile organic solvents with aqueous electrolytes[41], elimination of toxic chemicals in the electrolyte[42, 43], replacement of Pt as counter electrode catalyst[44], use of green synthesis method for the nanostructured semiconductor [45, 46], application of non-toxic sealants [47] and the use of abundant metals for contacts [48].

1.3. Graphene Hybrids as Functional Components for Sustainable Sensitized Solar Cells

Graphene is a flexible thin layer of sp^2 hybridized carbon that could be synthesized from a variety of organic materials and wastes sources such as methane and biomass[49, 50], and, even though its mass production is still relatively costly, it is expected to drop in the near future [51]. The use of graphene can help in fixing GHGs from the atmosphere, such as methane, into long lasting solid state. It is a promising alternative to make more affordable and environmentally friendly technologies while meeting industry's needs of advanced electronic materials. Graphene, graphene oxide (GO) and its reduced form (rGO) hybridized with semiconductor NPs and quantum dots (QDs), carbon nanotubes (CNTs) and metal NPs can play distinct roles in SCs. **Table 1.1** summarizes the performance of different SCs incorporating graphene reported in literature.

Table 1.1.   Summary of SCs performance using graphene hybrids

Electrode with graphene hybrid	J_{sc} (mA/cm^2)	V_{oc} (V)	FF (%)	PCE (%)	Reference
PA: N719/ TiO$_2$/graphene	7.8	0.63	40	2.0	[52]
PA: N719/ TiO$_2$/graphene-Pt grid	2.9	0.43	32	0.4	[53]
PA: N3/TiO$_2$/rGO	1.0	0.70	36	0.3	[54]
PA: N719/TiO$_2$-GO/FTO	13.1	0.77	71	7.3	[55]
PA: N3/TiO$_2$-rGO/FTO	16.3	0.69	NA	7.0	[56]
PA: N719/ TiO$_2$-graphene nanofibers/FTO	16.2	0.71	66	7.6	[57]
PA: Graphene QD/TiO$_2$/FTO	0.2	0.48	58	NA	[58]
PA: ZnO-graphene QD/Cs$_2$CO$_3$/Al	0.2	0.99	24	2.3	[59]
PA: (TNS-rGO-CdS QD)$_{10}$/FTO	0.9	1.00*	41	0.4	[60]
PA: MWCNT-rGO-TiO2/FTO	11.3	0.78	70	6.1	[61]
EL: Graphene-SWCNTs-ionic liquid	7.3	0.59	44	2.5	[62]
CE: CuInS$_2$-rGO/FTO	16.6	0.74	51	6.2	[63]
CE: Cu$_2$S-rGO-PVA binder/FTO	18.4	0.52	46	4.4	[64]
CE: SWCNT-rGO/FTO	12.8	0.90	76	8.4	[65]
CE: MWCNT-rGO/FTO	16.1	0.75	63	7.6	[66]
CE: TiN-rGO-CNT/FTO	14.0	0.64	46	4.1	[67]
CE: rGO-CNT/FTO	11.4	0.77	53	4.7	[68]
CE: rGO-CNT/FTO	15.2	0.68	51	5.3	[69]
CE: CNT-rGO/graphite paper	12.9	0.78	61	6.2	[70]
CE: rGOnanoribbons-CNT/FTO	16.7	0.73	67	8.2	[71]
CE: VACNT-graphene paper	14.2	0.68	62	6.1	[72]
CE: Pt NPs/graphene nanosheets/FTO	18.2	0.72	65	8.5	[73]
CE: graphene nanoplateletes-Pt NPs/FTO	14.3	0.73	62	6.5	[74]

PA: Photoanode, **CE**: Counter electrode, **EL**: Electrolyte

J$_{sc}$: Short circuit current density, **V$_{oc}$**: Open circuit voltage, **FF**: Fill factor, **PCE**: Power conversion efficiency

*V vs Ag/AgCl

Due to graphene´s superior optoelectronic properties, it can be used as TC in the photoanode to substitute tin oxides and overcome their disadvantages, such as high cost, environmental impact, and low transmittance in the UV and near-infrared range [75]. Reports of TiO$_2$ DSCs incorporating CVD-graphene and rGO as TC demonstrate its feasibility for fabricating tin-oxide free photoanodes, although, equal or better TC performance of graphene compared to tin oxides has not been demonstrated yet [52-54]. Hybrids of graphene and semiconductor NPs have been used in the photoanode, where graphene acts as electrical bridge for faster extraction of photoinduced electrons and recombination supression. In a stacked structure of titania nanosheets, rGO and CdS QD, graphene provided additional paths for electrons to be collected in the photoanode and a faster hole transport to the electrolyte[60, 76]. Graphene also increases porosity for improved light scattering, with just 0.6% weight load of rGO providing the best PCE[56, 57]. Combining

graphene and CNT reduces aggregation between graphene sheets for increased dye adsorption and lower recombination [61]. Graphene QDs display semiconductor properties, electrons can be photoexcitated from the HOMO to the LUMO, therefore, they can be applied as sensitizers in the photoanode. In a DSC incorporating ZnO/graphene quasi-core-shell QDs, the excited electrons in the conduction band of ZnO are rapidly transferred into graphene's LUMO, quickly making ZnO available for new photoelectric events [59].

Graphene can also be part of the electrolyte and counter electrode to improve redox activity and act as electrical bridge, as it does in the photoanode. The combination of graphene and CNT with ionic liquids in a quasi-solid state electrolyte increased the PCE of the cell from 0.16 up to 2.5%, because the carbon nanomaterials act as charge transporters in the ionic liquid and as catalysts for the electrochemical reduction of I^{3-} [62]. Graphene/semiconductor hybrids, such as graphene-CuInS$_2$ and rGO/Cu$_2$S, are feasible substitutes for Pt in the counter electrode. Graphene's large surface area promotes stabilization and dispersion of nanoparticles, provides high number of reactive sites for capturing electrons from the redox mediator, and rapidly shuttles electrons across the counter electrode interfaces. Graphene hybrids may exhibit higher photocatalytic activity than Pt towards certain mediators like polysulfide [63, 64, 77]. Graphene-CNT incorporation in the counter electrode demonstrated that CNTs bridged gaps between graphene flakes, improved the electrical conductivity and provided good catalytic and electrical properties, yielding PCE that are competitive with Pt, with lower cost and better mechanical flexibility[70-72]. In graphene-Pt hybrids the graphene can act as an electrical contact between Pt and FTO or as a co-catalyst[74, 78]. The use of Ni NPs anchored on graphene provided a Pt-free counter electrode with a higher PCE than Pt [79].

The diversity, versatility and performance of graphene variants provides a promising future for its application in DSCs. Recently, a semitransparent and flexible solar cell fabricated with all-graphene electrodes was reported [80]. The use of graphene hybrids in DSCs can result in reduced manufacturing costs and increased sustainability for up-scaling of SC technology, while opening possibilities for light-weight flexible devices.

1.4. Natural Phototropic Systems as Bio-Sensitizers

The Earth's solar-based ecosystem has a 3-billion-year record of success. Two types of *phototrophic* systems are responsible for harvesting the solar energy for almost all life on Earth: (1) light-induced charge separation followed by electron transport chains, used in **photosynthesis**, and (2) photo-isomerization, used in **proton pumping**. Both phototropic mechanisms occur in membranes across which an electrochemical gradient is established and ultimately drives ATP synthesis, photosynthesis occurring in the thylakoid, and proton pumping in the cell membrane. However, the PCE of photosynthesis come within a factor of 2 or 3 of the photovoltaic benchmark, mainly because the driving force of evolution is reproduction, and not maximum PCE[81]. Scientists have been discussing the coupling of natural phototropic systems with electrodes via redox mediators as an strategy to surpass their low PCE as far back as 1974[82]. The fabrication of biophotoelectrochemical devices using phototrophic biosytems is a more environmental route than merely mimicking them in fully-artificial devices, but it is also more challenging, due to their complexity and instability outside of the organism[83]. Biophotoelectrochemical cells consist on the natural chromophore immobilized on a photoanode, connected to a cathode via an electrolyte solution, and their development has been examined in several reviews [84-87]. Diffusional electron transfer mediators dissolved in the electrolyte are used for most biophotoelectrochemical cells, but the mediator can also be fixed on the electrode [88, 89]. The photoanode platform can be the TC itself, or the TC coated with a wide-bandgap semiconductor for a SC configuration, and the power generation mechanism is slightly different for each. Biosystems are a biocompatible, biodegradable, non-toxic and environmentally friendly alternative to the expensive synthetic dyes used in SCs.

Extensive research has been devoted to device integration of chromophores from photosynthesis[90]. The reaction center of **oxygenic photosynthetic systems** from Plantae and cyanobacteria, photosystems (PS) I[89] and II [91-96], have been integrated in photoelectrochemical devices, whether as a whole or some parts of them. The use of chlorophyll *a* in SC was first reported by Gratzel in 1993 [97] and derivatives of it were

later used to improve its attachment to the TiO_2 substrate[98, 99]. The entire chloroplasts[100] and thylakoid[101, 102], as well as accessory pigments like chlorophyll *b* and *c*[103], carotenoids[104, 105], anthocyanins[106-108], curcuminoids[106] and xanthophylls[109] have been reported as photoactive components and co-sensitizers in photoelectrochemical cells. The integration of the reaction center from **anoxygenic photosynthetic systems** in devices has been widely explored too [110], including a device with the capacity of autonomous regeneration capacity[111]. Bacteriochlorophyll from purple sulfur bacteria is of great interest because it absorbs further into the near infrared spectrum compared to oxygenic chlorophyll[112]. Performance improvement has been demonstrated by immobilizing redox mediators like cytochrome *c* and quinone on the bacteriochlorophyll electrode [113, 114]. Several kinds of active photosynthetic microorganisms have been incorporated in **photosynthetic microbial fuel cells**[115], like cyanobacteria[116-118], purple sulfur bacteria[119] green algae[120-122] and plants [123, 124], with advantages like self-repair, improved stability, less laborious purification processes and power generation in dark and in light. In complete bioelectrochemical cells, the products of the bio-photoanode are consumed in a bio-cathode functionalized, for example, with proteins that reduce oxygen like bilirubin oxidase [88, 125] or protons like hydrogenase[126], as well as heterotrophic microorganisms[127]. The internal quantum efficiency of charge separation in photosynthesis is ~100% and the charge carrier recombination time is $>10^{-1}$ for PSII stacked membrane converter, much more efficient and with long-lasting excited states than $<10^{-3}$ for Si PV. Furthermore, carbon dioxide can be stripped off from the atmosphere in bio-electrochemical cells that produce carbohydrates [128]. Despite of high yield of primary charge separation and relative high potential in biophotoelectrochemical cells based on photosynthetic systems (~0.21V[110]), their PCE remains low (~0.002 %[110]) due to low photocurrent outputs.

The photo-isomerization used by Archaea is a rather rare phototropic mechanism in nature, and has received less attention for device integration. It is evolutionarily younger than photosynthesis, and quite different, as it does not result in carbohydrate synthesis but direct proton pumping[129]. Amongst light-activated proton pumps studied in photoelectric devices, **bacteriorhodopsin** (bR), the retinal-containing

protein from Halobacteria, stands as the most explored to date. It has advantages over photosynthethic systems in terms of long term stability against thermal, chemical, and photochemical degradation and its large-scale production is relatively easy and cost-effective[130, 131]. Its integration in synthetic devices has been attempted in multiple ways, but the highest efficient PCE has been obtained when bR is incorporated in photoelectrochemical cells, rather than in thin film solid-state devices. The photovoltage of solid–state devices of bR films packed between electrodes is in the order of 10^{-1}-10^{1} V [132], although some studies reported photovoltages as high as 300mV [133]. However, the poor conductivity of BR in solid state (10^{-7} S/cm) [134] results in low PCE with photocurrents in the order of nA and pA [135]. The BR photocycle seems to occur faster in aqueous media than solid, for example, it has been found 10-20 times faster cycle in suspension than in a polymer matrix[136]. bR photoelectrochemical devices initially were developed following the membrane physiology of the organisms, where porous membranes separate two chambers containing aqueous solutions, and the bR is whether fixed in the membrane [137, 138] or suspended in one of the chambers [139]. The addition of plasmonic Ag NPs to such membrane-separated photoelectrochemical cells resulted in faster BR cycle and improved photocurrent[140], however, their PCE still remains low.

Recently, the concept of bR-sensitized solar cells (bR-SCs) have gained more attention, as this protein complies with the technical requirements for a sensitizer of good stability and extended excited state lifetime [141]. The first TiO$_2$ bR-SC was reported in 2009, a design based on the energy alignment of the bR LUMO with the CB of TiO$_2$, and the HOMO with the redox potential of the I$^-$/I$_3^-$ pair. The wild type protein was compared to a mutant variant designed promote binding to the TiO$_2$ and favor electron transfer, from which the mutant bR-SC had a better performance, but it was also less chemically and thermally stable than the wild type[30]. bR sensitized photoanodes have been studied to produce solar H$_2$ and shown photocurrents significantly higher than previous studies [142, 143]. Several variables to improve the cell performance have been studied like the treatment of the TiO$_2$ with TiCl$_4$ to increase the porosity of the NPs [144], the use of nanofiber scattering layer to enhance the optical path length, the time and temperatures of bR incubation

on TiO_2 [145], the combination of BR and the bacterioruberin pigment from the same organism [146], the immobilization of BR by Langmuir-Blodgett method on ZnO NP [147], comparison of TiO_2 NPs and nanotubes [148] and the substitution of liquid triiodide redox electrolyte by gel electrolyte [149]. The bR-SC with the highest PCE of 0.49%[149] and stability for more than 3 months[145] demonstrates that bR can yield performance comparable to synthetic dyes when the platform is properly designed.

The bR-SC power generation mechanism is based on the heterojunction between the donor (bR) and the acceptor (ZnO, TiO_2), a mechanism different than the proton pumping that takes place in the native organism, and yet has provided the highest PCE amongst the different device configurations. The electrochemical gradient generated by bR in the living bacteria is only 200mV [150], while values up to 670mV were obtained in bR-SC[149], demonstrating how rational design can expand the natural capabilities of biosystems. A proposed advance is the combination of bR with QDs to improve cell performance[151]. **However, few reports of bR as sensitizer in SCs have been published to date, compared to dyes and photosynthetic chromophores. More research is needed to overcome the low PCE of bR-SCs, and biophotoelectrochemical cells in general, a technology that is still primitive.**

Biophotoelectrochemical cells produce photovoltage of several hundred millivolts, therefore their low PCE is mostly a result of limited photocurrent, ascribed to different factors. The first factor is poor electrical connection of the bio-cromophores with the electrode, as the electron donating group is commonly deeply buried in the biomolecules, and biological materials display low conductivity. Furthermore, the electron transport pathway is vectorial in phototropic systems, therefore proper orientation is key for their efficient functioning. The use of electrical nanowires[152] and controlling orientation, for example with polyhistidine tags and Ni^+-NTA system[153], helps to solve this problem. The second factor is the low surface density of photoactive molecules, which can be improved by increasing the surface area of the electrode by roughening the surface, creating molecular multilayers and matching the size of the molecules to the pore size of the nanostructured electrode. The third factor is the energy mismatch of the elements in the cell.

Scientists endorse the low efficiency of natural photosynthesis processes to the mismatch of photochemical processes with redox cofactors, a legacy biochemistry inherited from non-phototrophic organism[154]. Proper selection of elements and characterization of their electronic structure is necessary, as well as doping and addition of components to create energy cascade structures. The fourth factor is kinetic competition with charge recombination processes, for which the community has been paying more attention to the proton-coupled electron transfer processes that takes place in photosynthesis to extend the lifetime of charge-separated states[155, 156]. Even though the link between redox processes and transmembrane proton gradients is the unifying concept in bioenergetics, it has been mostly disregarded in the design of biophotovoltaics. The activation energy of redox reactions or proton-couple electron transfer processes has also been proposed as the possible cause for low potocurrents, which could be solved by modification of redox mediators or electrode surface[156]. **bR is a robust well-known system to investigate solutions to these limitations and establish a molecular basis for future progress in the field of biophotovoltaics.**

1.5. The Concept of a Biophotovoltaic Cell Built from Renewable Carbon

We propose the integration of photoactive biomolecules with carbonaceous materials derived from renewable sources as energy generation scheme with lower impacts on the environment and human health than current PV technologies. This novel PV device concept is based on a bio-sensitized solar cell (BSC) configuration, as illustrated in **Figure 1.4**. Carbon is an abundant element that exhibits a broad assortment of allotropic forms and electrical behavior, and it can make up an infinite variety of functional biomolecules when combined with other plentiful elements, like oxygen and hydrogen. Therefore, carbon can play many distinct functions in the BSC. The photoanode and counter electrode of such BSC would incorporate carbon nanomaterials and biomolecules derived from biological sources, such as graphene as TC, bR as sensitizer, and graphene-CNT hybrid as counter electrode.
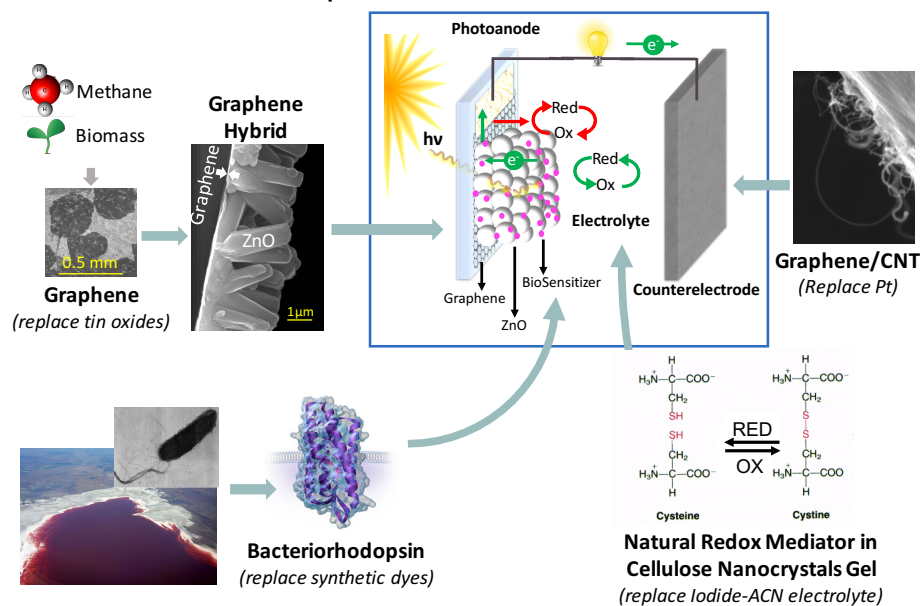
Figure 1.4. Conceptual diagram of a biophotovoltaic cell built from renewable carbon. Bacteriorhodopsin images adapted from online sources [157-159]

The electrolyte of a sustainable BSC should be aqueous, for which the performance has been demonstrated to improve with the presence of gelling agents[41]. Example of renewable carbon–based hydrogels are cellulose derivatives[160], including nanocellulose[161, 162]. The mediator of the electrolyte can be of biological origin too. The electron shuttles used by living organisms are sulfur, carbon rings and metals. The chemistry of the thiol group for SCs has been highlighted in literature, with redox pairs such as cysteine/cysteine[163] or disulfide/thiolate[164]. Quinones and metalloproteins, like the Fe-containing cytochrome *c*, have been reported as mediators for SCs, inspired on the proton-coupled electron transfer paths in photosynthesis [165-168].

Understanding the energy transduction and interfacial electrical transport in the device proposed here is relevant not only for this biophotovoltaics, but for advancement of sustainable bioelectronics and biophotonics in general. In the assessment of energy generation technology for the future, it is important to consider not only net PCE, but the relation of the device life cycle with human and environment, especially the interaction with the food supply, climate change and human rights[81].

1.6. Objectives of the work and experimental approach

The aim of this project is to gradually replace components in the photoanode of a sensitized solar cell with more sustainable alternatives derived from renewable carbon sources. We investigate the fabrication and performance of graphene-ZnO heterostructures and bacteriorhodopsin as functional components on the photoanode. This project is divided in four objectives, as illustrated in **Figure 1.5**.
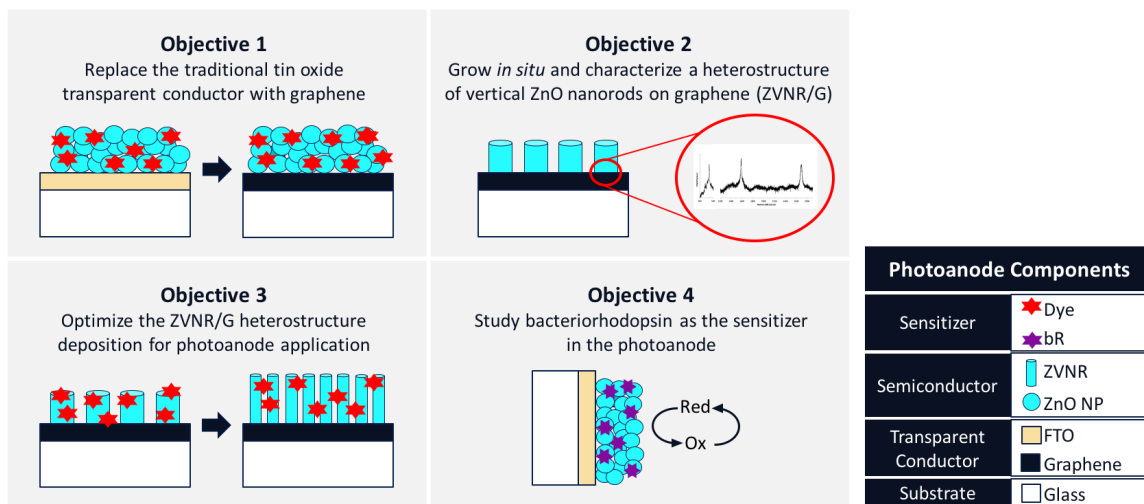
Figure 1.5.   Research objectives of the dissertation

In the first objective, the performance of graphene as TC is compared to that of FTO in a DSC made with slip-casted ZnO NPs sensitized with a synthetic dye. The practical challenges of incorporating graphene, a one atom-thick material, as a functional building block in large area devices are assessed. This work contributes to determining the feasibility of graphene to replace tin oxides as TC material. In the second objective, we study the *in situ* growth of vertically aligned ZnO nanorods (ZVNR) by cathodic electrodeposition on graphene and perform characterization of the hybrid materials. We emphasize on the heterostructure interface, especially on determining the prevalence of sp^2 hybridization in graphene to ensure that its attractive electrical properties are retained. In the third objective, the topography of the ZVNR/G hybrid is optimized for application as SC photoanode by changing parameters of the electrodeposition process. The structure of the ZVNR/G is designed to have large surface area and a very

efficient charge collection by minimizing losses caused by recombination. Finally, in the fourth objective, we use the bR to replace the synthetic dye on a ZnONPs/FTO platform, and explore the formulation of the electrolyte to improve the electron charge transfer at the interface. Each stage poses different challenges in terms of stability and interfacing of optical, electrical and mechanical properties of the different elements.

With the advances made in DNA recombinant and nanotechnology, new concepts for energy transduction based on natural systems are possible. Such bio-nanosystems remain a mystery for science in many senses; therefore, a systematic study of the role and behavior of each individual element may provide insight into the photoelectric processes taking place. The analysis of energy levels of the chosen materials dictate that the proposed system is energetically feasible, considering that electron transfer in interfaces occurs only between energy states that are approximately at the same level, and more rapid when transferring thermodynamically downhill [169].

To determine the performance of the proposed systems we applied a detailed analysis of fabricated SCs combining linear sweep voltammetry (LSV), electrochemical impedance spectroscopy (EIS) and open-circuit voltage decay (OCVD). This approach provides insight of the internal charge transfer mechanisms, enabling to identify PCE loss mechanisms and solutions. **Figure 1.6(a)** shows the LSV curve of an illuminated reference cell we fabricated using a photoanode of ZnO NPs spread onto FTO and sensitized with a D149 dye. The short-circuit current density (J_{sc}), open circuit voltage (V_{oc}), PEC and fill factor (FF) are extracted from the J-V plot as shown in **Figure 1.6** and **Equations 1.1** and **1.2**.

$PEC = P_{max}/P_{in}$ **Equation 1.1**

$FF = P_{max}/J_{sc}xV_{oc}$ **Equation 1.2**
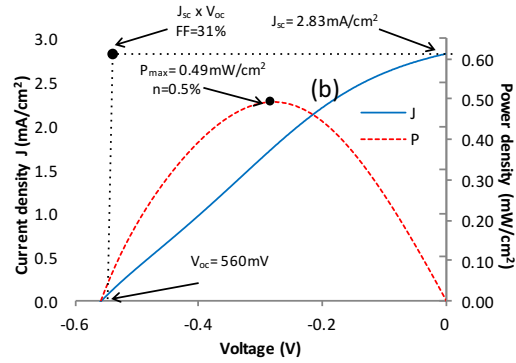
Figure 1.6. Current density-voltage (J-V) and power-voltage (P-V) characteristic for reference DSC under 100mW/cm2 Xe lamp.

Figure 1.7(a-b) shows the Nyquist and Bode plot of EIS spectra for the reference DSC described above. The experimental EIS data (Z_{exp}) is interpreted by the equivalent circuit model of **Figure 1.7(c)**. The impedance of a SC (Z_{Model}) is interpreted as a sum of the elements in series in the SC: resistance of the TC (R_{TC}), charge transfer impedance in the photoanode (Z_{PA}), Warburg diffusion impedance of the electrolyte (W) and charge transfer impedance at the counter-electrode (Z_{CE}), as described by **Equation 1.3**.

$$Z_{Model} = R_{TC} + Z_{PA} + W + Z_{CE} \qquad \textbf{Equation 1.3}$$

All the double layer capacitances in the interfaces of solids with electrolyte are considered constant phase element (CPE) to account for the deviation from an ideal capacitor. The impedance of a CPE with capacitance prefactor C and ideality factor n as a function of the frequency (ω) is given by **Equation 1.4.**

$$Z_{CPE}(\omega) = \frac{1}{j\omega^n C} \qquad \textbf{Equation 1.4}$$

17

Figure 1.7. (a) Nyquist and (b) Bode plots of experimental and fitted EIS of reference solar cell. (c) Equivalent circuit of SCs

R$_{TC}$ is found at the highest frequency in EIS, Z$_{CE}$ is a high-frequency peak, the middle-frequency peak corresponds to Z$_{PA}$, and W is found at the lowest frequency [170-173]. The R_{TC} corresponds to the sheet resistance of the transparent conductor. The Z$_{PA}$ is interpreted according to the most widely accepted model of electron diffusion through ZnO NPs (r_d) coupled to electron-transfer reactions with the electrolyte (r_k) in a transmission line model, in series with the charge transfer impedance at the TC/ZnO interface (Z$_{TC/ZnO}$) and parallel to the impedance for recombination of electrons from the TC to the electrolyte (Z$_{TC/El}$) [174]. R_d equals the sum of the inter-particle resistances r_d. R_k represents the numerous charge transfer resistances r_k between individual particles and electrolyte, and is generally much larger than R_d. The Z$_{TC/ZnO}$ is much smaller than the R$_k$ after annealing, while the Z$_{TC/El}$ is much larger than R$_k$, therefore, both Z$_{TC/ZnO}$ and Z$_{TC/El}$ can be neglected in the calculations. Therefore, the Z$_{PA}$ is simplified to the transmission line of R$_d$ and R$_k$ as described by **Equation 1.5**:

$$Z_{PA} = \sqrt{\frac{R_d R_k}{1+(j\omega)^{n_k} R_k CPE_k}} \times \coth\sqrt{\frac{R_d}{R_k}\{1 + (j\omega)^{n_k} R_k CPE_k\}} \qquad \textbf{Equation 1.5}$$

The W is given by σ, the Warburg diffusion coefficient of ions in the electrolyte on a surface according to the **Equation 1.6.**

$$W = \frac{\sqrt{2}\sigma}{\sqrt{j\omega}}$$ **Equation 1.6**

The Z_{CE} is expressed as capacitance (CPE_{CE})-resistor(R_{CE}) parallel circuit and is given by **Equation 1.7.**

$$Z_{CE} = \frac{R_{CE}}{1+(j\omega)^{n_{CE}}R_{CE}C_{CE}}$$ **Equation 1.7**

The Z_{Model} is constructed by using the Kirchoff rules to analyze the circuit, and applying complex number operations for the impedance elements with built-in functions in a Excel spreadsheet from literature [170]. The Z_{Model} provides estimate values of the internal impedance elements and kinetic parameters of the DSC. The fitting error (e) is kept within ±5% for all the analysis, as calculated from the **Equation 1.8.**

$$e = \frac{Z_{Exp}-Z_{Model}}{Z_{exp}} * 100$$ **Equation 1.8**

Extracting the transport kinetics for charge carriers in the cells is very useful as the mobility of the charges in the semiconductors is largely affected by scattering events [175], so we will use the photoconductive effect to measure the electron lifetime, i.e. mean free time between minority-carrier collisions τ. The generation of excess carriers in semiconductors under illumination cause a momentary increase of the conductivity, and when the light is turned off, the decay of this photocurrent can be monitored by the V_{oc} decay (OCVD) [173, 176]. The τ is extracted from the OCVD by **Equation 1.9**.

$$\tau = -\frac{k_B T}{n}\left(\frac{\mathrm{d}V_{OC}}{\mathrm{d}t}\right)^{-1}$$ **Equation 1.9**

Biophotovoltaic devices are in the first stage of their development, and the main challenge is their low PCE. We expect to contribute to the development of more efficient devices by fundamental studies of the internal mechanisms within a BSC. The extraction of kinetic parameters will provide significant insight in the charge transfer processes to identify the bottlenecks of the systems. **Our experimental work is aimed to understand how to better integrate functional membrane proteins and carbon nanomaterial hybrids derived from renewable sources into sustainable solar energy harvesting devices.**

1.7. References

1.   Crowley, T. J., Causes of climate change over the past 1000 years. *Science* **2000,** *289* (5477), 270-277.

2.   Tsao, J.; Lewis, N.; Crabtree, G. *Solar FAQs*; Sandia National Laboratories: 2006.

3.   Hoffert, M. I.; Caldeira, K.; Benford, G.; Criswell, D. R.; Green, C.; Herzog, H.; Jain, A. K.; Kheshgi, H. S.; Lackner, K. S.; Lewis, J. S.; Lightfoot, H. D.; Manheimer, W.; Mankins, J. C.; Mauel, M. E.; Perkins, L. J.; Schlesinger, M. E.; Volk, T.; Wigley, T. M. L., Advanced technology paths to global climate stability: Energy for a greenhouse planet. *Science* **2002,** *298* (5595), 981-987.

4.   Esteve-Núñez, A.; Caballero, A.; Ramos, J. L., Biological Degradation of 2,4,6-Trinitrotoluene. In *Microbiol Mol Biol Rev*, 2001; Vol. 65, pp 335-52.

5.   EPA, U. S., 2,4,6-Trinitrotoluene (TNT) Technical Fact   Sheet. (5106P), O. o. S. W. a. E. R., Ed. 2014.

6.   Systems, F. I. f. S. E. *Photovoltaics Report*; 2018.

7.   Hou, G. F.; Sun, H. H.; Jiang, Z. Y.; Pan, Z. Q.; Wang, Y. B.; Zhang, X. D.; Zhao, Y.; Yao, Q., Life cycle assessment of grid-connected photovoltaic power generation from crystalline silicon solar modules in China. *Applied Energy* **2016,** *164*, 882-890.

8.   Sherwani, A. F.; Usmani, J. A.; Varun, Life cycle assessment of solar PV based electricity generation systems: A review. *Renewable & Sustainable Energy Reviews* **2010,** *14* (1), 540-544.

9.   UNEP *Assessing the Environmental Impacts of Consumption and Production: Priority Products and Materials.*; International Panel for Sustainable Resource Management: 2010.

10.   Louwen, A.; van Sark, W.; Faaij, A. P. C.; Schropp, R. E. I., Re-assessment of net energy production and greenhouse gas emissions avoidance after 40 years of photovoltaics development. *Nature Communications* **2016,** *7*.

11.   Rowan, J. S.; Barnes, S. J. A.; Hetherington, S. L.; Lambers, B.; Parsons, F., Geomorphology and pollution: the Environmental Impacts of Lead Mining, Leadhills, Scotland. *Journal of Geochemical Exploration* **1995,** *52* (1-2), 57-65.

12.   Salomons, W., Environmental impact of metals derived from mining activities: Processes, predictions, prevention. *Journal of Geochemical Exploration* **1995,** *52* (1), 5-23.

13.   Dziubanek, G.; Baranowska, R.; Cwielag-Drabek, M.; Spychala, A.; Piekut, A.; Rusin, M.; Hajok, I., Cadmium in edible plants from Silesia, Poland, and its implications for health risk in populations. *Ecotoxicology and Environmental Safety* **2017,** *142*, 8-13.

14.   Camizuli, E.; Scheifler, R.; Garnier, S.; Monna, F.; Losno, R.; Gourault, C.; Hamm, G.; Lachiche, C.; Delivet, G.; Chateau, C.; Alibert, P., Trace metals from historical mining sites and past metallurgical activity remain bioavailable to wildlife today. *Scientific Reports* **2018,** *8*.

15.   Polgreen, L., Congo's Riches, Looted by Renegade Troops. *New York Times* 2008, p 14.

16.   Green, M. A.; Ho-Baillie, A.; Snaith, H. J., The emergence of perovskite solar cells. *Nature Photonics* **2014,** *8* (7), 506-514.

17.   Kazim, S.; Nazeeruddin, M. K.; Graetzel, M.; Ahmad, S., Perovskite as Light Harvester: A Game Changer in Photovoltaics. *Angewandte Chemie-International Edition* **2014,** *53* (11), 2812-2824.

18.	Levin, R.; Brown, M. J.; Kashtock, M. E.; Jacobs, D. E.; Whelan, E. A.; Rodman, J.; Schock, M. R.; Padilla, A.; Sinks, T., Lead Exposures in U.S. Children, 2008: Implications for Prevention. *Environ Health Perspect* **2008,** *116* (10), 1285-93.

19.	Fujishima, A.; Honda, K., ELECTROCHEMICAL PHOTOLYSIS OF WATER AT A SEMICONDUCTOR ELECTRODE. *Nature* **1972,** *238* (5358), 37-+.

20.	Matsumura, M.; Matsudaira, S.; Tsubomura, H.; Takata, M.; Yanagida, H., DYE SENSITIZATION AND SURFACE-STRUCTURES OF SEMICONDUCTOR ELECTRODES. *Industrial & Engineering Chemistry Product Research and Development* **1980,** *19* (3), 415-421.

21.	Gerischer, H.; Tributsch, H., ELECTROCHEMISTRY OF ZNO MONOCRYSTAL SPECTRAL SENSITIVITY. *Berichte Der Bunsen-Gesellschaft Fur Physikalische Chemie* **1968,** *72* (3), 437-+.

22.	Desilvestro, J.; Gratzel, M.; Kavan, L.; Moser, J.; Augustynski, J., HIGHLY EFFICIENT SENSITIZATION OF TITANIUM-DIOXIDE. *Journal of the American Chemical Society* **1985,** *107* (10), 2988-2990.

23.	Tsubomura, H.; Matsumura, M.; Nomura, Y.; Amamiya, T., DYE SENSITIZED ZINC-OXIDE - AQUEOUS-ELECTROLYTE - PLATINUM PHOTOCELL. *Nature* **1976,** *261* (5559), 402-403.

24.	Anderson, S.; Constable, E. C.; Dareedwards, M. P.; Goodenough, J. B.; Hamnett, A.; Seddon, K. R.; Wright, R. D., CHEMICAL MODIFICATION OF A TITANIUM(IV) OXIDE ELECTRODE TO GIVE STABLE DYE SENSITIZATION WITHOUT A SUPERSENSITIZER. *Nature* **1979,** *280* (5723), 571-573.

25.	Oregan, B.; Gratzel, M., A LOW-COST, HIGH-EFFICIENCY SOLAR-CELL BASED ON DYE-SENSITIZED COLLOIDAL TIO2 FILMS. *Nature* **1991,** *353* (6346), 737-740.

26.	Mathew, S.; Yella, A.; Gao, P.; Humphry-Baker, R.; Curchod, B. F. E.; Ashari-Astani, N.; Tavernelli, I.; Rothlisberger, U.; Nazeeruddin, M. K.; Gratzel, M., Dye-sensitized solar cells with 13% efficiency achieved through the molecular engineering of porphyrin sensitizers. *Nature Chemistry* **2014,** *6* (3), 242-247.

27.	Li, T. L.; Lee, Y. L.; Teng, H., High-performance quantum dot-sensitized solar cells based on sensitization with CuInS2 quantum dots/CdS heterostructure. *Energy & Environmental Science* **2012,** *5* (1), 5315-5324.

28.	Chandrasekhar, P. S.; Komarala, V. K., Effect of graphene and Au@SiO2 core-shell nano-composite on photoelectrochemical performance of dye-sensitized solar cells based on N-doped titania nanotubes. *Rsc Advances* **2015,** *5* (103), 84423-84431.

29.	Thakur, U. K.; Askar, A. M.; Kisslinger, R.; Wiltshire, B. D.; Kar, P.; Shankar, K., Halide perovskite solar cells using monocrystalline TiO2 nanorod arrays as electron transport layers: impact of nanorod morphology. *Nanotechnology* **2017,** *28* (27).

30.	Thavasi, V.; Lazarova, T.; Filipek, S.; Kolinski, M.; Querol, E.; Kumar, A.; Ramakrishna, S.; Padros, E.; Renugopalakrishnan, V., Study on the Feasibility of Bacteriorhodopsin as Bio-Photosensitizer in Excitonic Solar Cell: A First Report. *Journal of Nanoscience and Nanotechnology* **2009,** *9* (3), 1679-1687.

31.	Mershin, A.; Matsumoto, K.; Kaiser, L.; Yu, D.; Vaughn, M.; Nazeeruddin, M. K.; Bruce, B. D.; Graetzel, M.; Zhang, S., Self-assembled photosystem-I biophotovoltaics on nanostructured TiO2 and ZnO. *Scientific Reports* **2012,** *2*.

32.	Lee, C. P.; Lin, C. A.; Wei, T. C.; Tsai, M. L.; Meng, Y.; Li, C. T.; Ho, K. C.; Wu, C. I.; Lau, S. P.; He, J. H., Economical low-light photovoltaics by using the Pt-free dye-sensitized solar cell with graphene dot/PEDOT:PSS counter electrodes. *Nano Energy* **2015,** *18*, 109-117.

33.   Weerasinghe, H. C.; Huang, F. Z.; Cheng, Y. B., Fabrication of flexible dye sensitized solar cells on plastic substrates. *Nano Energy* **2013,** *2* (2), 174-189.

34.   Yoon, S.; Tak, S.; Kim, J.; Jun, Y.; Kang, K.; Park, J., Application of transparent dye-sensitized solar cells to building integrated photovoltaic systems. *Building and Environment* **2011,** *46* (10), 1899-1904.

35.   Hagfeldt, A., Brief Overview of Dye-Sensitized Solar Cells. *Ambio* **2012,** *41*, 151-155.

36.   Smestad, G.; Bignozzi, C.; Argazzi, R., TESTING OF DYE-SENSITIZED TIO2 SOLAR-CELLS .1. EXPERIMENTAL PHOTOCURRENT OUTPUT AND CONVERSION EFFICIENCIES. *Solar Energy Materials and Solar Cells* **1994,** *32* (3), 259-272.

37.   Kommalapati, R.; Kadiyala, A.; Shahriar, M. T.; Huque, Z., Review of the Life Cycle Greenhouse Gas Emissions from Different Photovoltaic and Concentrating Solar Power Electricity Generation Systems. *Energies* **2017,** *10* (3).

38.   Chang, C. Y.; Yu, H. Y.; Chen, J. J.; Li, F. B.; Zhang, H. H.; Liu, C. P., Accumulation of heavy metals in leaf vegetables from agricultural soils and associated potential health risks in the Pearl River Delta, South China. *Environmental Monitoring and Assessment* **2014,** *186* (3), 1547-1560.

39.   Shahid, M.; Dumat, C.; Khalid, S.; Niazi, N. K.; Antunes, P. M. C., Cadmium Bioavailability, Uptake, Toxicity and Detoxification in Soil-Plant System. *Reviews of Environmental Contamination and Toxicology* **2017,** *241*, 73-137.

40.   Yoo, K.; Kim, J. Y.; Lee, J. A.; Kim, J. S.; Lee, D. K.; Kim, K.; Kim, B.; Kim, H.; Kim, W. M.; Kim, J. H.; Ko, M. J., Completely Transparent Conducting Oxide-Free and Flexible Dye-Sensitized Solar Cells Fabricated on Plastic Substrates. *Acs Nano* **2015,** *9* (4), 3760-3771.

41.   Bella, F.; Gerbaldi, C.; Barolo, C.; Gratzel, M., Aqueous dye-sensitized solar cells. *Chemical Society Reviews* **2015,** *44* (11), 3431-3473.

42.   Xue, B. F.; Wang, H. X.; Hu, Y. S.; Li, H.; Wang, Z. X.; Meng, Q. B.; Huang, X. J.; Sato, O.; Chen, L. Q.; Fujishima, A., An alternative ionic liquid based electrolyte for dye-sensitized solar cells. *Photochemical & Photobiological Sciences* **2004,** *3* (10), 918-919.

43.   Yanagida, S.; Yu, Y. H.; Manseki, K., Iodine/Iodide-Free Dye-Sensitized Solar Cells. *Accounts of Chemical Research* **2009,** *42* (11), 1827-1838.

44.   Yun, S. N.; Lund, P. D.; Hinsch, A., Stability assessment of alternative platinum free counter electrodes for dye-sensitized solar cells. *Energy & Environmental Science* **2015,** *8* (12), 3495-3514.

45.   Yu, C. L.; Yu, J. C.; He, H. B.; Zhou, W. Q., Progress in sonochemical fabrication of nanostructured photocatalysts. *Rare Metals* **2016,** *35* (3), 211-222.

46.   Mirzaei, H.; Darroudi, M., Zinc oxide nanoparticles: Biological synthesis and biomedical applications. *Ceramics International* **2017,** *43* (1), 907-914.

47.   Sastrawan, R.; Beier, J.; Belledin, U.; Hemming, S.; Hinsch, A.; Kern, R.; Vetter, C.; Petrat, F. M.; Prodi-Schwab, A.; Lechner, P.; Hoffmann, W., A glass frit-sealed dye solar cell module with integrated series connections. *Solar Energy Materials and Solar Cells* **2006,** *90* (11), 1680-1691.

48.   More, V.; Bhargava, P., Electrodeposited copper current collecting fingers for DSSCs. *Materials Science in Semiconductor Processing* **2017,** *68*, 178-185.

49.   Azam, M. A.; Mudtalib, N. E. S. A. A.; Seman, R. N. A. R., Synthesis of graphene nanoplatelets from palm-based waste chicken frying oil carbon feedstock by using catalytic chemical vapour deposition. *Materials Today Communications* **2018,** *15*, 81-87.

50.   Seo, H. K.; Kim, T. S.; Park, C.; Xu, W.; Baek, K.; Bae, S. H.; Ahn, J. H.; Kim, K.; Choi, H. C.; Lee, T. W., Value-added Synthesis of Graphene: Recycling Industrial Carbon Waste into Electrodes for High-Performance Electronic Devices. *Scientific Reports* **2015,** *5*.

51.   McWilliams, A., Graphene Technologies, Applications and Markets. *Graphene Technologies, Applications and Markets* **2012**, 147 pp-147 pp.

52.   Selopal, G. S.; Milan, R.; Ortolani, L.; Morandi, V.; Rizzoli, R.; Sbveglieri, G.; Veronese, G. P.; Vomiero, A.; Concina, I., Graphene as transparent front contact for dye sensitized solar cells. *Solar Energy Materials and Solar Cells* **2015,** *135*, 99-105.

53.   Wang, X.; Zhi, L.; Muellen, K., Transparent, conductive graphene electrodes for dye-sensitized solar cells. *Nano Letters* **2008,** *8* (1), 323-327.

54.   Dong, P.; Zhu, Y.; Zhang, J.; Peng, C.; Yan, Z.; Li, L.; Peng, Z.; Ruan, G.; Xiao, W.; Lin, H.; Tour, J. M.; Lou, J., Graphene on Metal Grids as the Transparent Conductive Material for Dye Sensitized Solar Cell. *Journal of Physical Chemistry C* **2014,** *118* (45), 25863-25868.

55.   He, Z.; Hung, P.; Liu, J.; Thuc-Quyen, N.; Tan, T. T. Y., Understanding TiO2 Size-Dependent Electron Transport Properties of a Graphene-TiO2 Photoanode in Dye-Sensitized Solar Cells Using Conducting Atomic Force Microscopy. *Advanced Materials* **2013,** *25* (47), 6900-6904.

56.   Yang, N.; Zhai, J.; Wang, D.; Chen, Y.; Jiang, L., Two-Dimensional Graphene Bridges Enhanced Photoinduced Charge Transport in Dye-Sensitized Solar Cells. *Acs Nano* **2010,** *4* (2), 887-894.

57.   Madhavan, A. A.; Kalluri, S.; Chacko, D. K.; Arun, T. A.; Nagarajan, S.; Subramanian, K. R. V.; Nair, A. S.; Nair, S. V.; Balakrishnan, A., Electrical and optical properties of electrospun TiO2-graphene composite nanofibers and its application as DSSC photo-anodes. *Rsc Advances* **2012,** *2* (33), 13032-13037.

58.   Yan, X.; Cui, X.; Li, B.; Li, L.-s., Large, Solution-Processable Graphene Quantum Dots as Light Absorbers for Photovoltaics. *Nano Letters* **2010,** *10* (5), 1869-1873.

59.   Son, D. I.; Kwon, B. W.; Yang, J. D.; Park, D. H.; Seo, W. S.; Lee, H.; Yi, Y.; Lee, C. L.; Choi, W. K., Charge separation and ultraviolet photovoltaic conversion of ZnO quantum dots conjugated with graphene nanoshells. *Nano Research* **2012,** *5* (11), 747-761.

60.   Wang, K.; Wan, S.; Liu, Q.; Yang, N.; Zhai, J., CdS quantum dot-decorated titania/graphene nanosheets stacking structures for enhanced photoelectrochemical solar cells. *Rsc Advances* **2013,** *3* (45), 23755-23761.

61.   Ming-Yu, Y.; Min-Chien, H.; Shu-Hang, L.; Po, I. L.; Han-Min, T.; Ma, C. C. M.; Nen-Wen, P.; Ming-Der, G., Preparation of graphene/multi-walled carbon nanotube hybrid and its use as photoanodes of dye-sensitized solar cells. *Carbon* **2011,** *49* (11), 3597-606.

62.   Ahmad, I.; Khan, U.; Gun'ko, Y. K., Graphene, carbon nanotube and ionic liquid mixtures: towards new quasi-solid state electrolytes for dye sensitised solar cells. *Journal of Materials Chemistry* **2011,** *21* (42), 16990-16996.

63.   Liu, M.; Li, G.; Chen, X., One-Pot Controlled Synthesis of Spongelike CuInS2 Microspheres for Efficient Counter Electrode with Graphene Assistance in Dye-Sensitized Solar Cells. *Acs Applied Materials & Interfaces* **2014,** *6* (4), 2604-2610.

64.	Radich, J. G.; Dwyer, R.; Kamat, P. V., Cu2S Reduced Graphene Oxide Composite for High-Efficiency Quantum Dot Solar Cells. Overcoming the Redox Limitations of S-2(-)/S-n(2-) at the Counter Electrode. *Journal of Physical Chemistry Letters* **2011,** *2* (19), 2453-2460.

65.	Zheng, H.; Neo, C. Y.; Ouyang, J., Highly Efficient Iodide/Triiodide Dye-Sensitized Solar Cells with Gel-Coated Reduce Graphene Oxide/Single-Walled Carbon Nanotube Composites as the Counter Electrode Exhibiting an Open-Circuit Voltage of 0.90 V. *Acs Applied Materials & Interfaces* **2013,** *5* (14), 6657-6664.

66.	Velten, J.; Mozer, A. J.; Li, D.; Officer, D.; Wallace, G.; Baughman, R.; Zakhidov, A., Carbon nanotube/graphene nanocomposite as efficient counter electrodes in dye-sensitized solar cells. *Nanotechnology* **2012,** *23* (8).

67.	Youn, D. H.; Seol, M.; Kim, J. Y.; Jang, J.-W.; Choi, Y.; Yong, K.; Lee, J. S., TiN Nanoparticles on CNT-Graphene Hybrid Support as Noble-Metal-Free Counter Electrode for Quantum-Dot-Sensitized Solar Cells. *Chemsuschem* **2013,** *6* (2), 261-267.

68.	Li-Hsueh, C.; Chien-Kuo, H.; Min-Chien, H.; Jen-Chi, C.; Po, I. L.; Kuan-Ku, H.; Ma, C. C. M.; Ming-Yu, Y.; Ming-Chi, T.; Chuen-Horng, T., A graphene-multi-walled carbon nanotube hybrid supported on fluorinated tin oxide as a counter electrode of dye-sensitized solar cells. *Journal of Power Sources* **2013,** *222*, 518-25.

69.	Ma, J.; Zhou, L.; Li, C.; Yang, J.; Meng, T.; Zhou, H.; Yang, M.; Yu, F.; Chen, J., Surfactant-free synthesis of graphene-functionalized carbon nanotube film as a catalytic counter electrode in dye-sensitized solar cells. *Journal of Power Sources* **2014,** *247*, 999-1004.

70.	Guang, Z.; Likun, P.; Ting, L.; Tao, X.; Zhuo, S., Electrophoretic deposition of reduced graphene-carbon nanotubes composite films as counter electrodes of dye-sensitized solar cells. *Journal of Materials Chemistry* **2011,** *21* (38), 14869-75.

71.	Zhibin, Y.; Mingkai, L.; Chao, Z.; Weng Weei, T.; Tianxi, L.; Huisheng, P., Carbon Nanotubes Bridged with Graphene Nanoribbons and their Use in High-Efficiency Dye-Sensitized Solar Cells. *Angewandte Chemie International Edition* **2013,** *52* (14), 3996-9.

72.	Li, S.; Luo, Y.; Lv, W.; Yu, W.; Wu, S.; Hou, P.; Yang, Q.; Meng, Q.; Liu, C.; Cheng, H.-M., Vertically Aligned Carbon Nanotubes Grown on Graphene Paper as Electrodes in Lithium-Ion Batteries and Dye-Sensitized Solar Cells. *Advanced Energy Materials* **2011,** *1* (4), 486-490.

73.	Tsai, C.-H.; Chen, C.-H.; Hsiao, Y.-C.; Chuang, P.-Y., Investigation of graphene nanosheets as counter electrodes for efficient dye-sensitized solar cells. *Organic Electronics* **2015,** *17*, 57-65.

74.	Hoshi, H.; Tanaka, S.; Miyoshi, T., Pt-graphene electrodes for dye-sensitized solar cells. *Materials Science and Engineering B-Advanced Functional Solid-State Materials* **2014,** *190*, 47-51.

75.	Faccio, R.; Fernandez-Werner, L.; Pardo, H.; Mombru, A. W., Current Trends in Materials for Dye Sensitized Solar Cells. *Recent Patents on Nanotechnology* **2011,** *5* (1), 46-61.

76.	Yang, N. L.; Zhang, Y.; Halpert, J. E.; Zhai, J.; Wang, D.; Jiang, L., Granum-Like Stacking Structures with TiO2-Graphene Nanosheets for Improving Photo-electric Conversion. *Small* **2012,** *8* (11), 1762-1770.

77.	Santra, P. K.; Kamat, P. V., Mn-Doped Quantum Dot Sensitized Solar Cells: A Strategy to Boost Efficiency over 5%. *Journal of the American Chemical Society* **2012,** *134* (5), 2508-2511.

78.	Tripathi, B.; Yadav, P.; Pandey, K.; Kanade, P.; Kumar, M.; Kumar, M., Investigating the role of graphene in the photovoltaic performance improvement of dye-sensitized solar cell. *Materials Science and Engineering B-Advanced Functional Solid-State Materials* **2014,** *190*, 111-118.

79.   Bajpai, R.; Roy, S.; Kulshrestha, N.; Rafiee, J.; Koratkar, N.; Misra, D. S., Graphene supported nickel nanoparticle as a viable replacement for platinum in dye sensitized solar cells. *Nanoscale* **2012,** *4* (3), 926-930.

80.   Liu, Z. K.; You, P.; Liu, S. H.; Yan, F., Neutral-Color Semitransparent Organic Solar Cells with All-Graphene Electrodes. *Acs Nano* **2015,** *9* (12), 12026-12034.

81.   Blankenship, R. E.; Tiede, D. M.; Barber, J.; Brudvig, G. W.; Fleming, G.; Ghirardi, M.; Gunner, M. R.; Junge, W.; Kramer, D. M.; Melis, A.; Moore, T. A.; Moser, C. C.; Nocera, D. G.; Nozik, A. J.; Ort, D. R.; Parson, W. W.; Prince, R. C.; Sayre, R. T., Comparing Photosynthetic and Photovoltaic Efficiencies and Recognizing the Potential for Improvement. *Science* **2011,** *332* (6031), 805-809.

82.   Calvin, M., SOLAR-ENERGY BY PHOTOSYNTHESIS. *Science* **1974,** *184* (4134), 375-381.

83.   LaVan, D. A.; Cha, J. N., Approaches for biological and biomimetic energy conversion. *Proceedings of the National Academy of Sciences of the United States of America* **2006,** *103* (14), 5251-5255.

84.   Meunier, C. F.; Yang, X. Y.; Rooke, J. C.; Su, B. L., Biofuel cells Based on the Immobilization of Photosynthetically Active Bioentities. *Chemcatchem* **2011,** *3* (3), 476-488.

85.   Xie, X. J.; Bakker, E., Creating electrochemical gradients by light: from bio-inspired concepts to photoelectric conversion. *Physical Chemistry Chemical Physics* **2014,** *16* (37), 19781-19789.

86.   Hug, H.; Bader, M.; Mair, P.; Glatzel, T., Biophotovoltaics: Natural pigments in dye-sensitized solar cells. *Applied Energy* **2014,** *115*, 216-225.

87.   Sekar, N.; Ramasamy, R. P., Photosynthetic Energy Conversion: Recent Advances and Future Perspective. *Electrochemical Society Interface* **2015,** *24* (3), 67-73.

88.   Yehezkeli, O.; Tel-Vered, R.; Wasserman, J.; Trifonov, A.; Michaeli, D.; Nechushtai, R.; Willner, I., Integrated photosystem II-based photo-bioelectrochemical cells. *Nature Communications* **2012,** *3*.

89.   Robinson, M. T.; Gizzie, E. A.; Mwambutsa, F.; Cliffel, D. E.; Jennings, G. K., Mediated approaches to Photosystem I-based biophotovoltaics. *Current Opinion in Electrochemistry* **2017,** *5* (1), 211-217.

90.   McCormick, A. J.; Bombelli, P.; Bradley, R. W.; Thorne, R.; Wenzel, T.; Howe, C. J., Biophotovoltaics: oxygenic photosynthetic organisms in the world of bioelectrochemical systems. *Energy & Environmental Science* **2015,** *8* (4), 1092-1109.

91.   Kato, M.; Sato, H.; Yagi, I.; Sugiura, M., Bio-inorganic hybrid photoanodes of photosystem II and ferricyanide-intercalated layered double hydroxide for visible-light-driven water oxidation. *Electrochimica Acta* **2018,** *264*, 386-392.

92.   Badura, A.; Kothe, T.; Schuhmann, W.; Rogner, M., Wiring photosynthetic enzymes to electrodes. *Energy & Environmental Science* **2011,** *4* (9), 3263-3274.

93.   Iwuchukwu, I. J.; Vaughn, M.; Myers, N.; O'Neill, H.; Frymier, P.; Bruce, B. D., Self-organized photosynthetic nanoparticle for cell-free hydrogen production. *Nature Nanotechnology* **2010,** *5* (1), 73-79.

94.   Millsaps, J. F.; Bruce, B. D.; Lee, J. W.; Greenbaum, E., Nanoscale photosynthesis: Photocatalytic production of hydrogen by platinized photosystem I reaction centers. *Photochemistry and Photobiology* **2001,** *73* (6), 630-635.

95.   Utschig, L. M.; Dimitrijevic, N. M.; Poluektov, O. G.; Chemerisov, S. D.; Mulfort, K. L.; Tiede, D. M., Photocatalytic Hydrogen Production from Noncovalent Biohybrid Photosystem I/Pt Nanoparticle Complexes. *Journal of Physical Chemistry Letters* **2011,** *2* (3), 236-241.

96.	Friebe, V. M.; Frese, R. N., Photosynthetic reaction center-based biophotovoltaics. *Current Opinion in Electrochemistry* **2017,** *5* (1), 126-134.

97.	Kay, A.; Gratzel, M., ARTIFICIAL PHOTOSYNTHESIS .1. PHOTOSENSITIZATION OF TIO2 SOLAR-CELLS WITH CHLOROPHYLL DERIVATIVES AND RELATED NATURAL PORPHYRINS. *Journal of Physical Chemistry* **1993,** *97* (23), 6272-6277.

98.	Kay, A.; Humphrybaker, R.; Gratzel, M., ARTIFICIAL PHOTOSYNTHESIS .2. INVESTIGATIONS ON THE MECHANISM OF PHOTOSENSITIZATION OF NANOCRYSTALLINE TIO2 SOLAR-CELLS BY CHLOROPHYLL DERIVATIVES. *Journal of Physical Chemistry* **1994,** *98* (3), 952-959.

99.	Amao, Y.; Komori, T., Bio-photovoltaic conversion device using chlorine-e(6) derived from chlorophyll from Spirulina adsorbed on a nanocrystalline TiO2 film electrode. *Biosensors & Bioelectronics* **2004,** *19* (8), 843-847.

100.	Greenbaum, E., Vectorial photocurrents and photoconductivity in metalized chloroplasts. *The Journal of Physical Chemistry* **1990,** *94* (16), 6151-6153.

101.	Lam, K. B.; Johnson, E. A.; Chiao, M.; Lin, L. W., A MEMS photosynthetic electrochemical cell powered by subcellular plant photosystems. *Journal of Microelectromechanical Systems* **2006,** *15* (5), 1243-1250.

102.	Calkins, J. O.; Umasankar, Y.; O'Neill, H.; Ramasamy, R. P., High photo-electrochemical activity of thylakoid-carbon nanotube composites for photosynthetic energy conversion. *Energy & Environmental Science* **2013,** *6* (6), 1891-1900.

103.	Wang, X. F.; Koyama, Y.; Kitao, O.; Wada, Y.; Sasaki, S.; Tamiaki, H.; Zhou, H. S., Significant enhancement in the power-conversion efficiency of chlorophyll co-sensitized solar cells by mimicking the principles of natural photosynthetic light-harvesting complexes. *Biosensors & Bioelectronics* **2010,** *25* (8), 1970-1976.

104.	Diarra, A.; Hotchandani, S.; Max, J. J.; Leblanc, R. M., PHOTOVOLTAIC PROPERTIES OF MIXED MONOLAYERS OF CHLOROPHYLL A AND CAROTENOID CANTHAXANTHIN. *Journal of the Chemical Society-Faraday Transactions Ii* **1986,** *82*, 2217-2231.

105.	Hao, S. C.; Wu, J. H.; Huang, Y. F.; Lin, J. M., Natural dyes as photosensitizers for dye-sensitized solar cell. *Solar Energy* **2006,** *80* (2), 209-214.

106.	Furukawa, S.; Iino, H.; Iwamoto, T.; Kukita, K.; Yamauchi, S., Characteristics of dye-sensitized solar cells using natural dye. *Thin Solid Films* **2009,** *518* (2), 526-529.

107.	Wahyuono , R. A.; Risanti, D. D., Selection of Natural Dye Photosensitizer for Quasi-solid State Dye-sensitized Mesoporous TiO2 Solar Cell (DSC) Fabrication. In *International Conference on Chemical and Material Engineering*, Semarang Indonesia, 2012.

108.	Polo, A. S.; Iha, N. Y. M., Blue sensitizers for solar cells: Natural dyes from Calafate and Jaboticaba. *Solar Energy Materials and Solar Cells* **2006,** *90* (13), 1936-1944.

109.	Liu, B. Q.; Zhao, X. P.; Luo, W., The synergistic effect of two photosynthetic pigments in dye-sensitized mesoporous TiO2 solar cells. *Dyes and Pigments* **2008,** *76* (2), 327-331.

110.	Tan, S. C.; Crouch, L. I.; Mahajan, S.; Jones, M. R.; Welland, M. E., Increasing the Open-Circuit Voltage of Photoprotein-Based Photoelectrochemical Cells by Manipulation of the Vacuum Potential of the Electrolytes. *Acs Nano* **2012,** *6* (10), 9103-9109.

111.	Ham, M. H.; Choi, J. H.; Boghossian, A. A.; Jeng, E. S.; Graff, R. A.; Heller, D. A.; Chang, A. C.; Mattis, A.; Bayburt, T. H.; Grinkova, Y. V.; Zeiger, A. S.; Van Vliet, K. J.; Hobbie, E. K.; Sligar, S. G.; Wraight, C. A.; Strano, M. S.,

Photoelectrochemical complexes for solar energy conversion that chemically and autonomously regenerate. *Nature Chemistry* **2010,** *2* (11), 929-936.

112.   Lu, Y. D.; Yuan, M. J.; Liu, Y.; Tu, B.; Xu, C. H.; Liu, B. H.; Zhao, D. Y.; Kong, J. L., Photoelectric performance of bacteria photosynthetic proteins entrapped on tailored mesoporous WO3-TiO2 films. *Langmuir* **2005,** *21* (9), 4071-4076.

113.   Lebedev, N.; Trammell, S. A.; Spano, A.; Lukashev, E.; Griva, I.; Schnur, J., Conductive wiring of immobilized photosynthetic reaction center to electrode by cytochrome c. *Journal of the American Chemical Society* **2006,** *128* (37), 12044-12045.

114.   Yaghoubi, H.; Lafalce, E.; Jun, D.; Jiang, X. M.; Beatty, J. T.; Takshi, A., Large Photocurrent Response and External Quantum Efficiency in Biophotoelectrochemical Cells Incorporating Reaction Center Plus Light Harvesting Complexes. *Biomacromolecules* **2015,** *16* (4), 1112-1118.

115.   Rosenbaum, M.; He, Z.; Angenent, L. T., Light energy to bioelectricity: photosynthetic microbial fuel cells. *Current Opinion in Biotechnology* **2010,** *21* (3), 259-264.

116.   Tsujimura, S.; Wadano, A.; Kano, K.; Ikeda, T., Photosynthetic bioelectrochemical cell utilizing cyanobacteria and water-generating oxidase. *Enzyme and Microbial Technology* **2001,** *29* (4-5), 225-231.

117.   Sekar, N.; Jain, R.; Yan, Y.; Ramasamy, R. P., Enhanced photo-bioelectrochemical energy conversion by genetically engineered cyanobacteria. *Biotechnology and Bioengineering* **2016,** *113* (3), 675-679.

118.   Rogner, M., Metabolic engineering of cyanobacteria for the production of hydrogen from water. *Biochemical Society Transactions* **2013,** *41*, 1254-1259.

119.   Cho, Y. K.; Donohue, T. J.; Tejedor, I.; Anderson, M. A.; McMahon, K. D.; Noguera, D. R., Development of a solar-powered microbial fuel cell. *Journal of Applied Microbiology* **2008,** *104* (3), 640-650.

120.   Rosenbaum, M.; Schroder, U.; Scholz, F., Utilizing the green alga Chlamydomonas reinhardtii for microbial electricity generation: a living solar cell. *Applied Microbiology and Biotechnology* **2005,** *68* (6), 753-756.

121.   Powell, E. E.; Mapiour, M. L.; Evitts, R. W.; Hill, G. A., Growth kinetics of Chlorella vulgaris and its use as a cathodic half cell. *Bioresource Technology* **2009,** *100* (1), 269-274.

122.   Berk, R. S.; Canfield, J. H., BIOELECTROCHEMICAL ENERGY CONVERSION. *Applied Microbiology* **1964,** *12* (1), 10-&.

123.   Strik, D.; Hamelers, H. V. M.; Snel, J. F. H.; Buisman, C. J. N., Green electricity production with living plants and bacteria in a fuel cell. *International Journal of Energy Research* **2008,** *32* (9), 870-876.

124.   Kouzuma, A.; Kaku, N.; Watanabe, K., Microbial electricity generation in rice paddy fields: recent advances and perspectives in rhizosphere microbial fuel cells. *Applied Microbiology and Biotechnology* **2014,** *98* (23), 9521-9526.

125.   Sekar, N.; Umasankar, Y.; Ramasamy, R. P., Photocurrent generation by immobilized cyanobacteria via direct electron transport in photo-bioelectrochemical cells. *Physical Chemistry Chemical Physics* **2014,** *16* (17), 7862-7871.

126.   Krassen, H.; Ott, S.; Heberle, J., In vitro hydrogen production-using energy from the sun. *Physical Chemistry Chemical Physics* **2011,** *13* (1), 47-57.
127.   He, Z.; Kan, J.; Mansfeld, F.; Angenent, L. T.; Nealson, K. H., Self-Sustained Phototrophic Microbial Fuel Cells Based on the Synergistic Cooperation between Photosynthetic Microorganisms and Heterotrophic Bacteria. *Environmental Science & Technology* **2009,** *43* (5), 1648-1654.

128.   Cao, X. X.; Huang, X.; Liang, P.; Boon, N.; Fan, M. Z.; Zhang, L.; Zhang, X. Y., A completely anoxic microbial fuel cell using a photo-biocathode for cathodic carbon dioxide reduction. *Energy & Environmental Science* **2009,** *2* (5), 498-501.

129.   *Origin and Evolution of Biological Energy Conversion*. Wiley: 1996.

130.   Miercke, L. J. W.; Ross, P. E.; Stroud, R. M.; Dratz, E. A., PURIFICATION OF BACTERIORHODOPSIN AND CHARACTERIZATION OF MATURE AND PARTIALLY PROCESSED FORMS. *Journal of Biological Chemistry* **1989,** *264* (13), 7531-7535.

131.   Lee, S. Y.; Chang, H. N.; Um, Y. S.; Hong, S. H., Bacteriorhodopsin production by cell recycle culture of Halobacterium halobium. *Biotechnology Letters* **1998,** *20* (8), 763-765.

132.   Li, L. S.; Xu, T.; Zhang, Y. J.; Jin, J.; Li, T. J.; Zou, B. S.; Wang, J. P., Photovoltaic characteristics of BR/p-silicon heterostructures using surface photovoltage spectroscopy. *Journal of Vacuum Science & Technology a-Vacuum Surfaces and Films* **2001,** *19* (4), 1037-1041.

133.   Chen, Z. P.; Lewis, A.; Takei, H. Y.; Nebenzahl, I., BACTERIORHODOPSIN ORIENTED IN POLYVINYL-ALCOHOL FILMS AS AN ERASABLE OPTICAL STORAGE MEDIUM. *Applied Optics* **1991,** *30* (35), 5188-5196.

134.   Alfinito, E.; Pousset, J.; Reggiani, L.; Lee, K., Photoreceptors for a light biotransducer: a comparative study of the electrical responses of two (type-1) opsins. *Nanotechnology* **2013,** *24* (39).

135.   Jin, Y.; Honig, T.; Ron, I.; Friedman, N.; Sheves, M.; Cahen, D., Bacteriorhodopsin as an electronic conduction medium for biomolecular electronics. *Chemical Society Reviews* **2008,** *37* (11), 2422-2432.

136.   Collins, A. M.; Kaus, N. H. M.; Speranza, F.; Briscoe, W. H.; Rhinow, D.; Hampp, N.; Mann, S., Assembly of poly(methacrylate)/purple membrane lamellar nanocomposite films by intercalation and in situ polymerisation. *Journal of Materials Chemistry* **2010,** *20* (41), 9037-9041.

137.   Al-Aribe, K. M.; Knopf, G. K.; Bassi, A. S. In *Organic photovoltaic cells based on photoactive bacteriorhodopsin proteins*, Conference on Microfluidics, BioMEMS, and Medical Microsystems XI, San Francisco, CA, 2013 Feb 03-05; San Francisco, CA, 2013.

138.   Nicolini, C.; Erokhin, V.; Paddeu, S.; Sartore, M., Towards a light-addressable transducer bacteriorhodopsin-based. *Nanotechnology* **1998,** *9* (3), 223-227.

139.   Yen, C.-W.; Hayden, S. C.; Dreaden, E. C.; Szymanski, P.; El-Sayed, M. A., Tailoring Plasmonic and Electrostatic Field Effects To Maximize Solar Energy Conversion by Bacteriorhodopsin, the Other Natural Photosynthetic System. *Nano Letters* **2011,** *11* (9), 3821-3826.

140.   Li-Kang, C.; Chun-Wan, Y.; El-Sayed, M. A., Bacteriorhodopsin-based photo-electrochemical cell. *Biosensors & Bioelectronics* **2010,** *26* (2), 620-6.

141.   Roy-Mayhew, J. D.; Aksay, I. A., Graphene Materials and Their Use in Dye-Sensitized Solar Cells. *Chemical Reviews* **2014,** *114* (12), 6323-6348.

142.   Allam, N. K.; Yen, C.-W.; Near, R. D.; El-Sayed, M. A., Bacteriorhodopsin/TiO2 nanotube arrays hybrid system for enhanced photoelectrochemical water splitting. *Energy & Environmental Science* **2011,** *4* (8), 2909-2914.

143.   Balasubramanian, S.; Wang, P.; Schaller, R. D.; Rajh, T.; Rozhkova, E. A., High-Performance Bioassisted Nanophotocatalyst for Hydrogen Production. *Nano Letters* **2013,** *13* (7), 3365-3371.

144.   Janfaza, S.; Molaeirad, A.; Mohamadpour, R.; Khayati, M.; Mehrvand, J., Efficient bio-nano hybrid solar cells via purple membrane as sensitizer. *BioNanoScience* **2014,** *4* (1), 6.

145.   Mohammadpour, R.; Janfaza, S., Efficient Nanostructured Biophotovoltaic Cell Based on Bacteriorhodopsin as Biophotosensitizer. *Acs Sustainable Chemistry & Engineering* **2015,** *3* (5), 809-813.

146.   Molaeirad, A.; Janfaza, S.; Karimi-Fard, A.; Mahyad, B., Photocurrent generation by adsorption of two main pigments of Halobacterium salinarum on TiO2 nanostructured electrode. *Biotechnology and Applied Biochemistry* **2015,** *62* (1), 121-125.

147.   Molaeirad, A.; Rezaeian, N., Oriented assembly of bacteriorhodopsin on ZnO nanostructured electrode for enhanced photocurrent generation. *Biotechnology and Applied Biochemistry* **2014**, 5.

148.   Naseri, N.; Janfaza, S.; Irani, R., Visible light switchable bR/TiO2 nanostructured photoanodes for bio-inspired solar energy conversion. *Rsc Advances* **2015,** *5* (24), 18642-18646.

149.   Chellamuthu, J.; Nagaraj, P.; Chidambaram, S. G.; Sambandam, A.; Muthupandian, A., Enhanced photocurrent generation in bacteriorhodopsin based bio-sensitized solar cells using gel electrolyte. *Journal of Photochemistry and Photobiology B-Biology* **2016,** *162*, 208-212.

150.   Juretic, D.; Zupanovic, P., Photosynthetic models with maximum entropy production in irreversible charge transfer steps. *Computational Biology and Chemistry* **2003,** *27* (6), 541-553.

151.   Renugopalakrishnan, V.; Barbiellini, B.; King, C.; Molinari, M.; Mochalov, K.; Sukhanova, A.; Nabiev, I.; Fojan, P.; Tuller, H. L.; Chin, M.; Somasundaran, P.; Padros, E.; Ramakrishna, S., Engineering a Robust Photovoltaic Device with Quantum Dots and Bacteriorhodopsin. *Journal of Physical Chemistry C* **2014,** *118* (30), 16710-16717.

152.   Rajesh; Paul, R. K.; Mulchandani, A., Platinum nanoflowers decorated three-dimensional graphene-carbon nanotubes hybrid with enhanced electrocatalytic activity. *Journal of Power Sources* **2013,** *223*, 23-29.

153.   Das, R.; Kiley, P. J.; Segal, M.; Norville, J.; Yu, A. A.; Wang, L. Y.; Trammell, S. A.; Reddick, L. E.; Kumar, R.; Stellacci, F.; Lebedev, N.; Schnur, J.; Bruce, B. D.; Zhang, S. G.; Baldo, M., Integration of photosynthetic protein molecular complexes in solid-state electronic devices. *Nano Letters* **2004,** *4* (6), 1079-1083.

154.   Gust, D.; Kramer, D.; Moore, A.; Moore, T. A.; Verrnaas, W., Engineered and artificial photosynthesis: Human ingenuity enters the game. *Mrs Bulletin* **2008,** *33* (4), 383-387.

155.   Mora, S. J.; Odella, E.; Moore, G. F.; Gust, D.; Moore, T. A.; Moore, A. L., Proton-Coupled Electron Transfer in Artificial Photosynthetic Systems. *Accounts of Chemical Research* **2018,** *51* (2), 445-453.

156.   Xie, X. J.; Bakker, E., Photoelectric Conversion Based on Proton-Coupled Electron Transfer Reactions. *Journal of the American Chemical Society* **2014,** *136* (22), 7857-7860.

157.   Studios, F. Bacteriorhodopsin. http://www.fairmanstudios.com/bacteriorhodopsin/.

158.   Oestrehelt, D. Halobacterium salinarum - overview. http://www.biochem.mpg.de/522218/Org_Hasal.

159.   Owens Lake. **2018**.

160.   Bella, F.; Galliano, S.; Falco, M.; Viscardi, G.; Barolo, C.; Grätzel, M.; Gerbaldi, C., Approaching truly sustainable solar cells by the use of water and cellulose derivatives. **2016**.

161.   Miettunen, K.; Vapaavuori, J.; Tiihonen, A.; Poskela, A.; Lahtinen, P.; Hatme, J.; Lund, P., Nanocellulose aerogel membranes for optimal electrolyte filling in dye solar cells. *Nano Energy* **2014,** *8*, 95-102.

162.   Du, X.; Zhang, Z.; Liu, W.; Deng, Y. L., Nanocellulose-based conductive materials and their emerging applications in energy devices - A review. *Nano Energy* **2017,** *35*, 299-320.

163.   Cheng, M.; Yang, X.; Li, S.; Wang, X.; Sun, L., Efficient dye-sensitized solar cells based on an iodine-free electrolyte using L-cysteine/L-cystine as a redox couple. *Energy & Environmental Science* **2012,** *5* (4), 6290-6293.

164.   Wang, M.; Chamberland, N.; Breau, L.; Moser, J.-E.; Humphry-Baker, R.; Marsan, B.; Zakeeruddin, S. M.; Grätzel, M., An organic redox electrolyte to rival triiodide/iodide in dye-sensitized solar cells. *Nature Chemistry* **2010,** *2* (5), 385.

165.   Cheng, M.; Yang, X. C.; Zhang, F. G.; Zhao, J. H.; Sun, L. C., Efficient Dye-Sensitized Solar Cells Based on Hydroquinone/Benzoquinone as a Bioinspired Redox Couple. *Angewandte Chemie-International Edition* **2012,** *51* (39), 9896-9899.

166.   Flores-Díaz, N.; Soto-Navarro, A.; Freitag, M.; Lamoureux, G.; Pineda, L. W., Neutral organic redox pairs based on sterically hindered hydroquinone/benzoquinone derivatives for dye-sensitized solar cells. *Solar Energy* **2018,** *167*, 76-83.

167.   Woronowicz, K.; Ahmed, S.; Biradar, A. A.; Biradar, A. V.; Birnie, D. P., III; Asefa, T.; Niederman, R. A., Near-IR Absorbing Solar Cell Sensitized With Bacterial Photosynthetic Membranes. *Photochemistry and Photobiology* **2012,** *88* (6), 1467-1472.

168.   Hvasanov, D.; Peterson, J. R.; Thordarson, P., Self-assembled light-driven photosynthetic-respiratory electron transport chain hybrid proton pump. *Chemical Science* **2013,** *4* (10), 3833-3838.

169.   Morrison, S. R., The Chemical physics of surfaces. Plenum: New York, 1990; p 438.

170.   Sarker, S.; Ahammad, A. J. S.; Seo, H. W.; Kim, D. M., Electrochemical Impedance Spectra of Dye-Sensitized Solar Cells: Fundamentals and Spreadsheet Calculation. *International Journal of Photoenergy* **2014**.

171.   Qing, W.; Moser, J. E.; Gratzel, M., Electrochemical impedance spectroscopic analysis of dye-sensitized solar cells. *Journal of Physical Chemistry B* **2005,** *109* (31), 14945-53.

172.   Kern, R.; Sastrawan, R.; Ferber, J.; Stangl, R.; Luther, J., Modeling and interpretation of electrical impedance spectra of dye solar cells operated under open-circuit conditions. *Electrochimica Acta* **2002,** *47* (26), 4213-4225.

173.   Bisquert, J.; Fabregat-Santiago, F.; Mora-Sero, I.; Garcia-Belmonte, G.; Gimenez, S., Electron Lifetime in Dye-Sensitized Solar Cells: Theory and Interpretation of Measurements. *Journal of Physical Chemistry C* **2009,** *113* (40), 17278-17290.

174.   Bisquert, J., Theory of the impedance of electron diffusion and recombination in a thin layer. *Journal of Physical Chemistry B* **2002,** *106* (2), 325-333.

175.   Adam, S.; Hwang, E. H.; Galitski, V. M.; Das Sarma, S., A self-consistent theory for graphene transport. *Proceedings of the National Academy of Sciences of the United States of America* **2007,** *104* (47), 18392-18397.

176.   Sze, S.; Ng, K., *Physics of Semiconductor Devices*. 3rd ed.; John Wiley and Sons, Inc.: 2006; p 815.

Chapter I:

Graphene Compared to Doped Tin Oxide as Transparent Conductor in ZnO Dye-Sensitized Solar Cells

Abstract

Due to its high transparency and electrical conductivity, graphene could replace widely used transparent conductors (TC) like fluorine-doped and indium tin oxides (FTO and ITO, respectively). This work focuses on the technical feasibility of pristine graphene produced by chemical vapor deposition (CVD) to replace FTO in the photoanode of dye-sensitized solar cells (DSCs). This is the first study in which graphene is used as photoanode TC in a tin oxide-free DSC using ZnO as mesoporous semiconductor. The stability of graphene towards hybridization with ZnO was investigated using electrical measurements and Raman spectroscopy. A thorough comparison of performance between FTO- and graphene-DSCs under identical conditions was done using current density–voltage (J-V) plots, electrochemical impedance spectroscopy (EIS) and open circuit voltage decay (OCVD) for 10 samples fabricated with each material. Graphene DSCs consistently produced larger open circuit voltage (V_{oc}) and short circuit current density (J_{sc}) than FTO DSCs, attributed to graphene's higher optical transmittance. However, the fill factor (FF) was lower for the graphene DSCs, attributed to the larger sheet resistance of graphene. Graphene and FTO DSCs yielded similar power conversion efficiencies (PCE) of 0.4%, despite graphene having a thickness that is two orders of magnitude smaller than FTO. The findings have important cost and environmental implications for largescale production, not only for DSCs, but also for the many photovoltaic technologies derived from them, such as perovskites and quantum dot-SCs.

2.1. Introduction

Graphene's flexibility, transparency and high electrical conductivity make it an ideal transparent conductor (TC) for optoelectronic devices, such as touchscreens, displays, lighting and smart windows [1-3], as well as different kinds of photovoltaic devices, including dye-sensitized solar cells (DSCs) [4-9]. The principal materials used for these applications are doped tin oxides (i.e. FTO, ITO), which are brittle, rare, costly - possibly toxic - and their production requires the use of conflict minerals, i.e. cassiterite [10, 11]. It has been shown that mining and industrial wastes related to these materials can adversely affect water quality and human health [12-14]. Furthermore, cassiterite has been linked to armed conflicts in African countries, making regulation compliance an escalating cost for tin oxide industry world-wide [15, 16]. In comparison, graphene is made from the abundant element carbon, can be synthesized from a variety of organic materials and wastes, and its mass production cost is expected to drop in the near future [17].

The use of graphene as TC poses the challenge of minimizing its sheet resistance (R_s), while maintaining a high optical transmittance (T), properties contained in the figure of merit $\sigma_{dc/op}$, the ratio of direct current conductivity to optical conductivity, given by Equation 1, where $Z_0 = 377\ \Omega$ is the free space impedance [18].

$$\sigma_{dc/op} = \sigma_{dc}/\sigma_{op} = \frac{Z_0}{2R_s}\left(\frac{1}{\sqrt{T}} - 1\right)^{-1} \tag{1}$$

In photovoltaics, a $\sigma_{dc/op}$ value at least larger than 32 is desirable ($R_s < 50\ \Omega/\square$ and $T > 80\%$); for example, ITO has $\sigma_{dc/op} = 110\text{-}150$ [19]. The theoretical maximum $\sigma_{dc/op}$ value for pristine single layer graphene (1LG) is 2.55, which has already been reached experimentally but may not be good enough for a TC [18, 20, 21]. Reducing R_s has the largest effect on increasing $\sigma_{dc/op}$, and for graphene this could be achieved by increasing the effective mobility (μ), the film thickness (t), and the majority carrier density (n), according to the relation $R_s = (q\mu n t)^{-1}$, where q is the electron charge [22]. The high value of $\mu = 200,000$ cm^2/V·s, reported for mechanically exfoliated graphene, is one of the material's most exalted properties. However, it is uncommon to achieve such values in large area films [23]. Conventional CVD which is a suitable technique to scale-up graphene synthesis, commonly yields a film with $\sigma_{dc/op} \approx 3\text{-}10$ and μ of few thousand cm^2/V·s,

higher than other common methods like reduced graphene-oxide (rGO), and it could be further improved by increasing the crystal size and optimizing the transfer methods [18, 24]. The second parameter t increases with the number of carbon layers, and stacking of CVD-graphene films has been reported to decrease R , at the expense of T [25]. The third parameter, n, depends on the Fermi level for graphene and can be increased by doping, with estimations of figure of merit $\sigma_{dc/op}$=330 for highly doped 4 layer graphene (4LG) [18].

This work focuses on application of graphene in dye sensitized solar cells (DSCs), which are interesting photovoltaic devices because of their low cost and the possibility to fabricate flexible transparent modules [26, 27]. A DSC is composed of a photoanode and a counter-electrode, connected by an electrolyte. From the many elements that make up a DSC, the TC in the photoanode currently represents a large share of the cost and environmental impact, motivating the search for alternatives. Furthermore, the structure of a TC coated with a wide-bandgap semiconductor holds great relevance, as it has been inherited from DSCs into the photoanode platform for bulk heterojunction, quantum dot- and perovskite-sensitized solar cells, technologies that are rapidly changing the game of photovoltaics [28-30].

In this study, we compared the performance, internal resistance elements and charge kinetics for DSCs made with 4LG versus FTO as TC in the photoanode, using identical electrolyte and counter-electrodes. In contrast to all previous studies on graphene/TiO$_2$-DSCs, ZnO nanoparticles (NPs) were chosen as the mesoporous semiconductor layer, because ZnO can be more easily synthesized in a variety of morphologies using mild methods compatible with graphene technology. From the many approaches for hybridization of graphene with ZnO [31], we used a simple assembly by doctor blade as a first approach. The electrochemical measurements show similar power conversion efficiency for DSCs with both TC materials, but also reveal differences in charge generation and loss mechanisms between the two materials. Solutions for improving graphene´s performance as TC in photovoltaics are provided based on our results.

2.2. Experimental Procedures

2.2.1. Graphene growth and transfer

For the fabrication of graphene-based TCs, a continuous 1LG film was grown on Cu foil using a ambient-pressure (AP) CVD, with diluted methane as carbon source (~90ppm). This method was adapted from a previous publication of our group[32] by extending the growth time for single crystal domains to expand until achieving continuous graphene film. Cu foil 99.8% from Alfa Aesar, catalog# 46986, is cut and flattened. Then it is cleaned in a 5% v/v acetic acid solution for 10 min. Next, the Cu foil is rinsed with deionized water (DI water), acetone and isopropyl alcohol for 10 min each, followed by drying with N_2, carefully, to prevent wrinkle formation. The Cu foil is placed inside the furnace tube (1" diameter) on a quartz holder and annealed for two hours at 1030 °C in the furnace at atmospheric pressure with Ar (300 sccm) and H_2 (15 sccm). Then graphene is grown with 375 sccm of diluted methane in Ar (90ppm) and 15 sccm of H_2. After 60 minutes, the diluted methane is turned off and the tube is cooled with Ar (300 sccm) and H_2 (15 sccm) to room temperature. The continuity of the graphene is assessed by the destructive technique of oxidizing the Cu foil covered with graphene at 120 °C on a hot plate for 15 min and observing it under the optical microscope.

The graphene-coated Cu is spin-coated with PMMA (4% v/v in anisol) at 3000 rpm for 30 seconds, followed by baking at 95 °C for 3 minutes. Then, the copper layer is etched away by floating on a solution of $FeCl_3$ 0.3 M or ammonium persulfate 0.5 M. After the copper has been completely etched, the remaining solution is washed with DI water, and with HCl 10% for 1 hour, after which the solution is cleaned again with DI water. The floating 1LG is scooped by a second graphene/copper film. The PMMA/graphene/copper substrate is left to dry under air, and then is baked for 1 hour in the oven at 80 °C. The process is repeated until obtaining 4LG/copper film. Next, glass slides are washed with soap, sonicated in acetone, and finally soaked in piranha solution (3:1 H_2SO_2:H_2O_2) or concentrated NH_4OH for 30 minutes. The completely clean and hydrophilic glass is used to scoop the floating 4LG. The PMMA/4LG/glass assembly is soaked in acetone

overnight at 65 °C to remove the PMMA. The graphene-coated glass is annealed in furnace with Ar (100 sccm) and H_2 (15 sccm) at 400 °C and atmospheric pressure for 1 hour.

2.2.2.   Fabrication and Characterization of Photoanode

A 10nm/120nm Cr/Au collector was deposited around graphene-on-glass using e-beam evaporation. A mask of aluminum foil held with two small pieces of tape was used to avoid contamination of the 4LG with photoresists or thermal tape. The FTO-coated glass was cleaned with distilled water water, sonicated in acetone, rinsed with isopropyl alcohol and dried under nitrogen. Then it was annealed at 400°C and cooled down slowly. Finally, it was immersed in HNO_3 40% for 2min, rinsed with water and dried with N_2.

Subsequently, the 4LG and FTO TCs where coated with a mixture of commercially available ZnO-NPs of two different size ranges 1:1 (Alfa Aesar Nanotek #44899 40-100 nm and US Research Nanomaterials #US3590 10-30nm). The NPs were deposited on the substrate by spreading a paste by doctor blade. Two different pastes were explored, one that used polyethylene glycol (PEG) as medium and another that used sec-butanol (ButOH). The PEG paste was prepared by mortaring the ZnO NPs with PEG (M_n = 400) in 1:2 weight ratio, one layer of 15 $\mu l/cm^2$ from this paste was spread on the TC and annealed for 30 min at 400 °C in air for sintering. The ButOH paste was prepared by sonicating the NPs with 2-butanol in 1:6 weight ratio and 3% acetic acid as dispersant. This paste was applied by applying a layer of 15 $\mu l/cm^2$ on the TC and evaporating the solvent at 50°C, process that was repeated four times. The samples were dried in vacuum overnight and then annealed under air or argon at 400 °C for 30min. We will use as nomenclature ZF for the ZnO on FTO electrode, and ZG for the ZnO on 4LG.

The R of graphene was calculated from the bulk resistance (R_B) of a two terminal device on glass with the formula R = $R_B \cdot W/L$, where W is the width of the graphene area and L as the length between contacts, method that was validated against four-point measurements. The transfer characteristic of the graphene was measured in a Field Effect Transistor (FET) device. The three-terminal transistor device was made using graphene as the semiconducting channel, e-beam evaporated Cr (10 nm)/Au (120 nm) as

source-drain contacts, a highly doped p-type Si as global back gate, and 300 nm thermally grown SiO_2 as the gate dielectric. The graphene channel was prepared by photolithography and Reactive Ion Etching, with equal width and length dimensions of $1\mu m$. UV-Vis transmittance of graphene and FTO on glass was acquired using a spectrophotometer (DU 800, Beckman Coulter), with air as the blank.

The structure and morphology of ZG and ZF were characterized using Raman spectroscopy and scanning electron microscopy (SEM). The Raman spectra were obtained using a Horiba Scientific LabRam Monochromator equipped with a 532-nm laser. SEM was performed using the FEI NovaNanoSEM 450. The crystalline phase of ZnO in ZF and ZG hybrids was determined using X-ray diffraction (XRD). XRD measurements were taken at room temperature with the Empyrean diffractometer from Panalytical, using a copper anode at 40 mA and 45 kV and step size of 0.0260°. AFM of the ZG and ZFTO surfaces was obtained in tapping mode with Veeco's NanoScope V using Bruker CONTV-A tips.

2.2.3.   DSC Assembly

The photoanode was immersed 30 min in a 0.3 mM solution of D149 dye (Sigma-Aldrich) using acetonitrile and sec-butanol as solvents in ratios of 1:1 and 1mM sodium cholate, followed by rinsing with sec-butanol and drying in air. The counter-electrode was prepared e-beam evaporation of a 40 nm/40 nm Ti/Pt film on a clean glass substrate with 2 holes pre-drilled. The photoanode and counter-electrode were assembled together using polydimethysiloxane as spacer. The electrolyte was injected through the holes in the counter electrode. The electrolyte was composed by acetonitrile and ethylene carbonate as solvent in 1:3 volume ratio, and 0.5 M tetrapropylammonium iodide and 0.05 M I_2 as redox mediator. The cyclic voltammogram of Pt disk electrode in this electrolyte is shown in **Figure 2.1**.
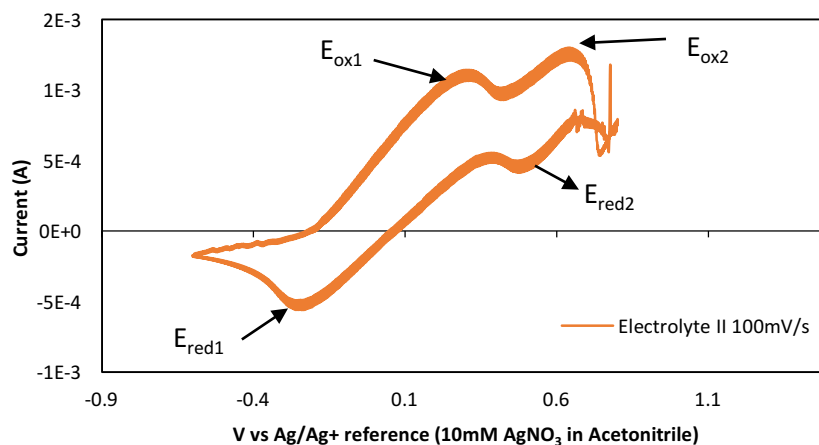
Figure 2.1. Cyclic voltammetry measurements for a Pt disk in the I^-/I_3^- electrolyte used for the DSSCs. The electrolyte is composed by acetonitrile and ethylene carbonate as solvent in 1:3 volume ratio, and 0.5 M tetrapropylammonium iodide and 0.05 M I_2 as redox mediator. CV measurements were carried from -0.6 V to 0.8 V at 100mV/s scanning rate.

2.2.4. DSCs Photolectrochemical Performance Measurement

The DSCs were tested under a xenon lamp (USHIO UXL-75XE) with 100 mW/cm^2 power input, calibrated with a Newport Power Meter 1918-R. J-V curves, EIS and OCVD of the solar cells were obtained with CHI 660C. The J-V curve was measured from 0.2 V to -0.8 V with a scan rate of 0.5 V/s. The EIS spectra was recorded under illumination, in the frequency range between 10^{-1} and 10^5 Hz, setting the bias voltage at the V_{oc} of the device and the amplitude at 10 mV. Fitting of the EIS data was done as described in **Section 1.6** [33-36]. The OCVD was measured by monitoring the open circuit voltage (V_{oc}) of the DSC after switching from illuminated to dark operation and the electron lifetime $\boldsymbol{\tau_n}$ was calculated according to **Equation 1.9**[37].

37

2.3. Results

A continuous film of 1LG was grown using AP-CVD with diluted methane (90 ppm in Ar) as a carbon source. The Raman spectra taken at different random positions for a continuous film of our SLG on SiO_2 in **Figure 2.2(a)** shows only two peaks, corresponding to the G band (1580cm^{-1}) and 2D band (2700cm-1) of graphene. The ratio of I_{2D}/I_G is ≥1 indicates a continuous film of single-layer graphene with sparse nuclei of few layer graphene on top as observed in **figure 2.2(b)**, which is common in CVD-graphene grown on Cu [39, 40]. The absence of D band at 1350cm^{-1} indicates a highly crystalline sp^2 carbon network, with large domains, since the crystallite size is inversely proportional to the ratio of I_D/I_G [41]. AFM in **figure 2.2(c)** was taken of a graphene edge on SiO_2 and the measurement of the graphene thickness was 0.3-0.5nm further confirming the single-layer nature of the CVD-graphene.
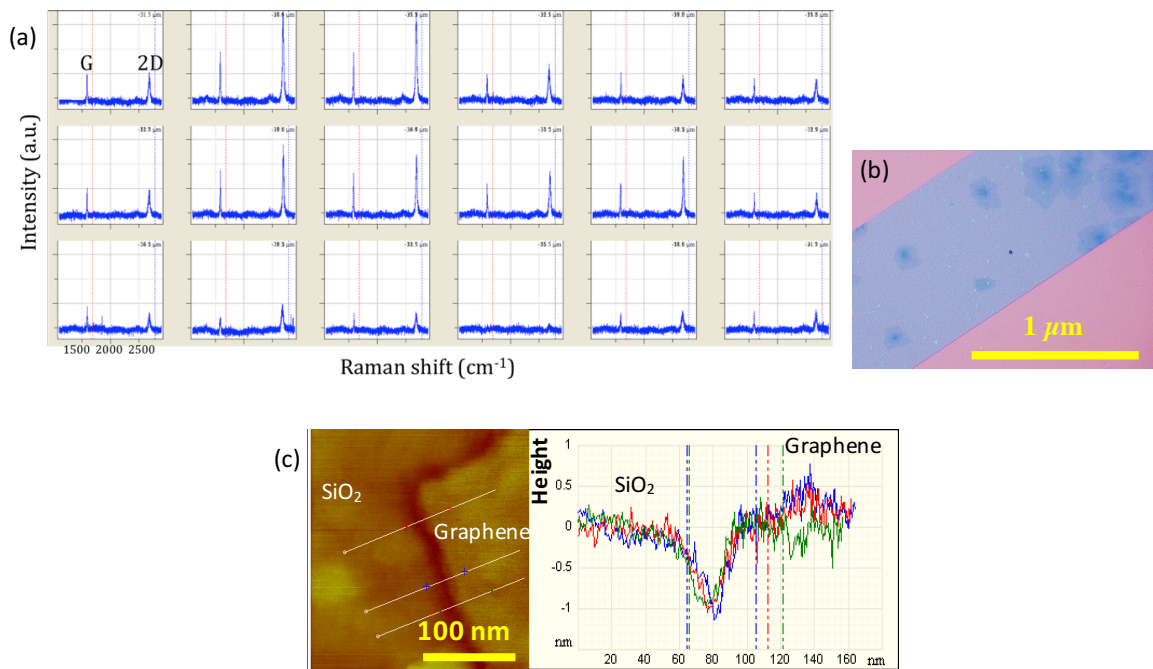
Figure 2.2. (a) Raman shift spectra for the graphene grown by CVD using diluted methane (90ppm in Ar) and transferred to SiO_2/Si substrate. (b) Optical micrograph of patterned graphene on SiO_2 showing a continuous single-layer graphene film with sparse nuclei of few-layer graphene on top. (c) AFM micrograph and height measurement of graphene edge on a SiO2 substrate.

Figure 2.3(a) shows the transfer properties by FET measurements of 8 different samples of SLG grown using methane 90ppm. This transport behavior, where the Dirac voltage is between 40 and 70V indicates strong p-doping for our processing. The hole mobility displayed in **figure 2.3(b)** was calculated from the transfer characteristic curves and its value between 4000 and 6000 cm^2/V.s which has been reported for CVD-graphene with similar domain size [38].
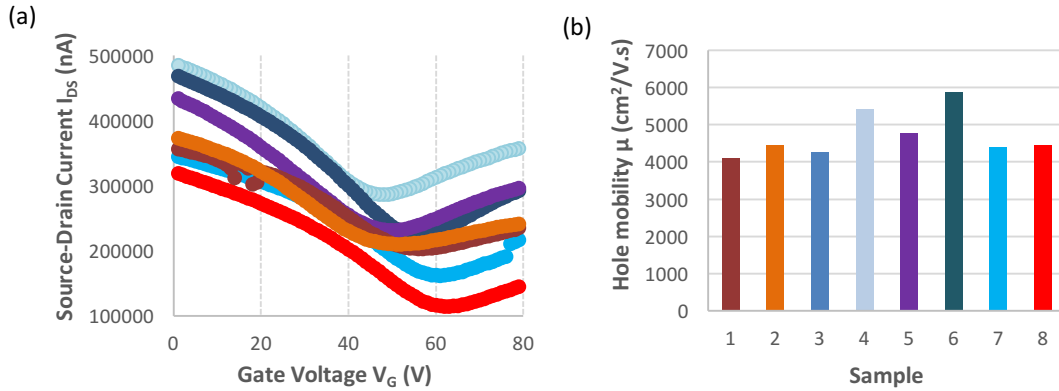
Figure 2.3. Transfer characteristic for different FET devices using graphene grown with diluted methane (90ppm) as carbon source. FETs were fabricated on 300nm SiO$_2$/Si, V$_{DS}$=0.1 (b) Hole mobility for different graphene samples obtained from the FET transfer characteristic curves.

The low methane concentration allowed the reduction of the nucleation density of graphene and growing a high quality 1LG with hexagonal crystals of diameter larger than 500μm, as shown in the inset of **Figure 2.4(a).** The main challenge with using graphene as a TC is minimizing its R while maintaining high T. As shown in **Figure 2.4(a)**, the R for 1LG was found to be ~1200 Ω/ , in comparison to 7 Ω/ for FTO, but stacking of individual 1LG layers reduced R to 372 Ω/ for 4LG.
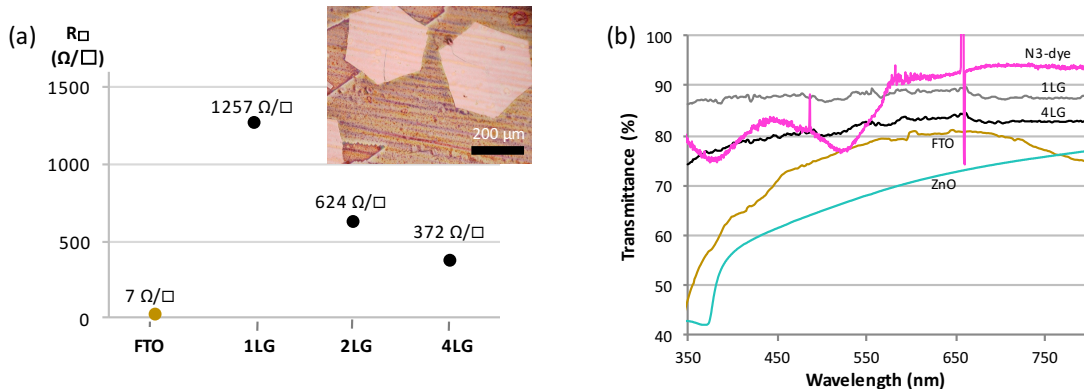
Figure 2.4. **(a) Sheet resistance of FTO and graphene; inset: Optical micrograph of graphene single crystals on copper at an intermediate growth stage showing large domains. (b) UV-vis transmittance of graphene, FTO, ZnO and N3 dye**

The comparison of UV-vis transmittance of graphene and FTO, along with the photoactive materials in the DSC, ZnO and N3 dye, is shown in **Figure 2.4(b).** The transmittance for 4LG in the UV-Visible light range (λ = 350 - 800 nm) was measured to be 75-85%, while FTO shows a more variable T, with only 50% transmittance at 350 nm, 81% at 660 nm and 75% at 800 nm. However, the 4LG had $\sigma_{dc/op}{\sim}5$, still significantly lower than $\sigma_{dc/op}{\sim}220$ for FTO, using the T at 550 nm. To further reduce the $R_\square$ of graphene, we tried to increase the number of charge carriers n with molecular doping by immersing the samples in concentrated nitric acid, which reduced the resistance by about 50%, but the original resistance was restored after a couple of days. Later we have tried spinning a $AuHCl_4$ solution on top of the graphene, and the doping effects have been stable over longer periods of time, but also tend to restore some of the original resistance. The value of $\sigma_{dc/op}$ for our Au-doped 4LG is 29.4 ($R_\square$=42 Ω/□ and T=75%), which is very close to our target of 31.

The hybridization of ZnO with the 4LG was characterized by measuring its electrical resistance. For the fabrication of ZG hybrid, the ButOH-ZnO paste showed good colloidal dispersion and formed a homogeneous continuous ZnO film on graphene. The R after application and drying of the ButOH-ZnO paste increased by 50-70% compared to bare graphene. Annealing in air at 400˚C of bare 4LG and ZG hybrids

prepared with ButOH and PEG pastes caused open circuit failure of the devices, while annealing in Ar only caused a slight resistance increase of 6% for ZG.

The stability and integrity of graphene during the fabrication and annealing steps was monitored using Raman spectroscopy. As shown in **Figure 2.5**, the Raman spectra of bare graphene (black curve) shows the characteristic G and 2D peaks at ~1590 cm^{-1} and ~2700 cm^{-1}, respectively. The Raman spectra of the ZG hybrid fabricated using ButOH-ZnO paste non-annealed and annealed in Ar at 400˚C (green curves) shows mostly no change with respect to bare graphene. The ZG hybrid also showed the characteristic Raman peaks for ZnO hexagonal wurtzite nanostructures below 500cm^{-1} (inset of **Figure 2.5**). When the same ZG hybrid was annealed in air (orange), a relatively large D peak with I_D/I_G = 1.3 appeared. The ZG hybrid fabricated with PEG paste required annealing in air to burn the polymer which lead to increase of D peak to yield I_D/I_G = 0.4 (yellow). Additionally, annealing in air of bare graphene (red) and ZG prepared both with PEG and ButOH pastes displayed the D' peak around 1620 – 1625 cm^{-1}. The higher degree of disorder introduced for bare graphene (I_D/I_G =2.2) in comparison to both ZG hybrids during thermal annealing in air indicates that the ZnO paste might have partly protected graphene from oxidation. In terms of the ratio between 2D and G peaks, some spectra resemble the Raman signature of 1LG ($I_{2D}>I_G$) and other correspond to that of few-layer graphene ($I_{2D}\leq I_G$), even though in all cases we used 4LG.
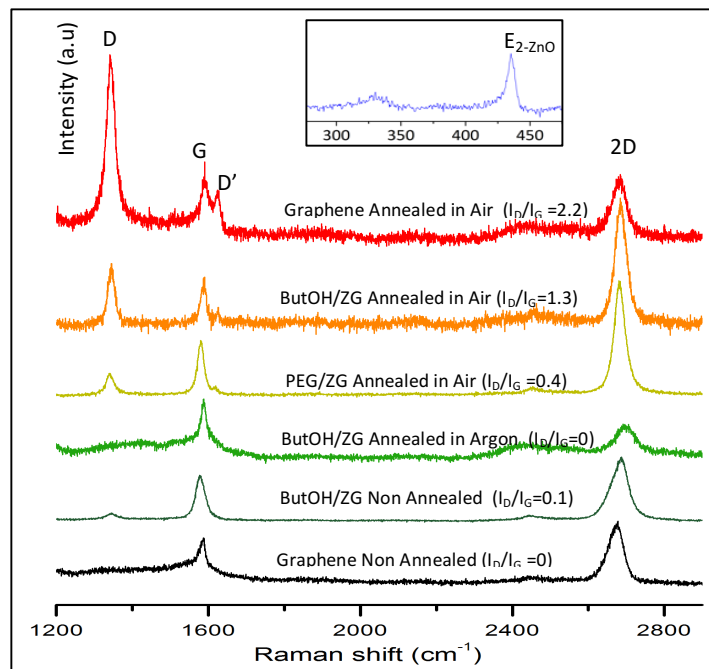
Figure 2.5. Raman spectra of graphene and ZG hybrids prepared under different conditions. Inset: Raman spectra region showing the ZnO peaks for ZG hybrids.

The contrast in thickness between the two TCs is illustrated in the cross-section SEM images of ZG and ZF and in **Figures 2.6 (a,b).** The 1.5 nm thickness of 4LG is two orders of magnitude smaller than the 500 nm thickness of FTO, implicating large savings of material for graphene TCs.
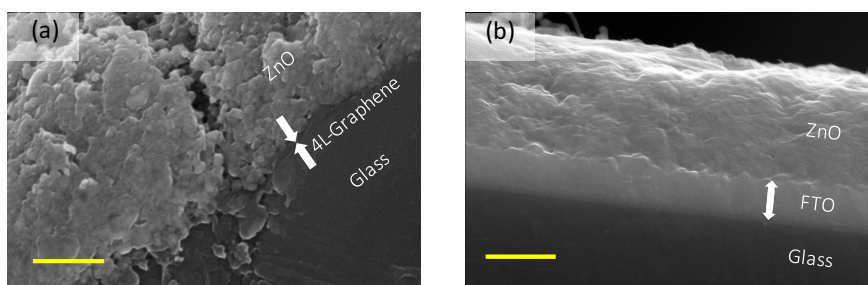
Figure 2.6. SEM images of the (a) ZG and (b) ZF photoanodes cross section. Scale bars correspond to 1μm.

The ZnO films for both ZG and ZF were porous, exhibiting an average roughness (R_a=336 ± 54 nm) as illustrated in the SEM and AFM microgrpahs illustrated in **Figures 2.7(a,b)**. As shown in **Figure 2.7(c),** the both ZnO films were crystalline and the XRD spectra was indexed to the ZnO wurtzite crystal structure (JCDP 36-1451), with the hexagonal space group P63mc (a=b=3.2494 Å, c=5.2058 Å, $\alpha=\beta=90°$, $\gamma=120°$). Additional peaks corresponding to the FTO substrate were found for ZF. The peak position and relative intensities for ZF and ZG prevail as compared to the commercial ZnO NPs. A shift of the peaks towards larger Bragg angle was observed after annealing.
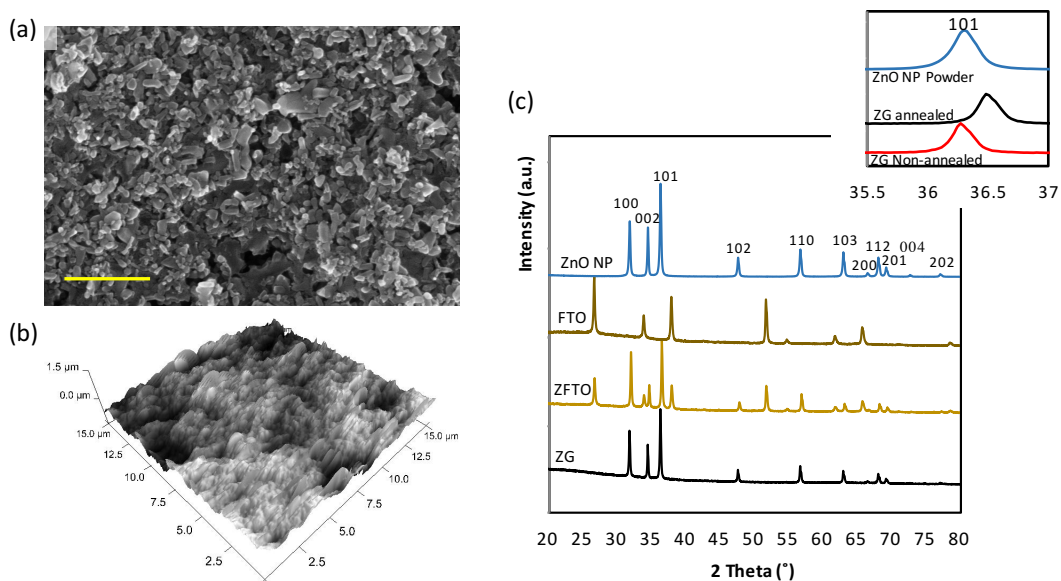
Figure 2.7.   Scale bars correspond to 1 µm. (c) X-Ray diffractogram of ZG and ZF samples, inset: X-ray diffraction of the {101} plane reflection for ZG hybrid before and after annealing.

The performance of the ZG and ZF electrodes was studied by fabricating DSCs with traditional D149 dye and I^-/I_3^- electrolyte. The DSC J-V plots are compared in **Figure 2.8(a)**, and the values of V_{oc}, J_{sc}, FF and PCE averaged for 10 samples of each material are summarized in **Figure 2.8(b)**. The V_{oc} of the ZG cells was found to be systematically larger than ZF, with ZG having an average value of 440mV and ZF 420mV. The J_{sc} was also found larger for ZG, with average value of 2.7 mA/cm^2, in comparison to 2.3 mA/cm^2 for ZF. However, the FF was found to be larger for FZ, with values of 41% compared to 33% of ZG, which resulted in both materials having equal average PCE of 0.4%.
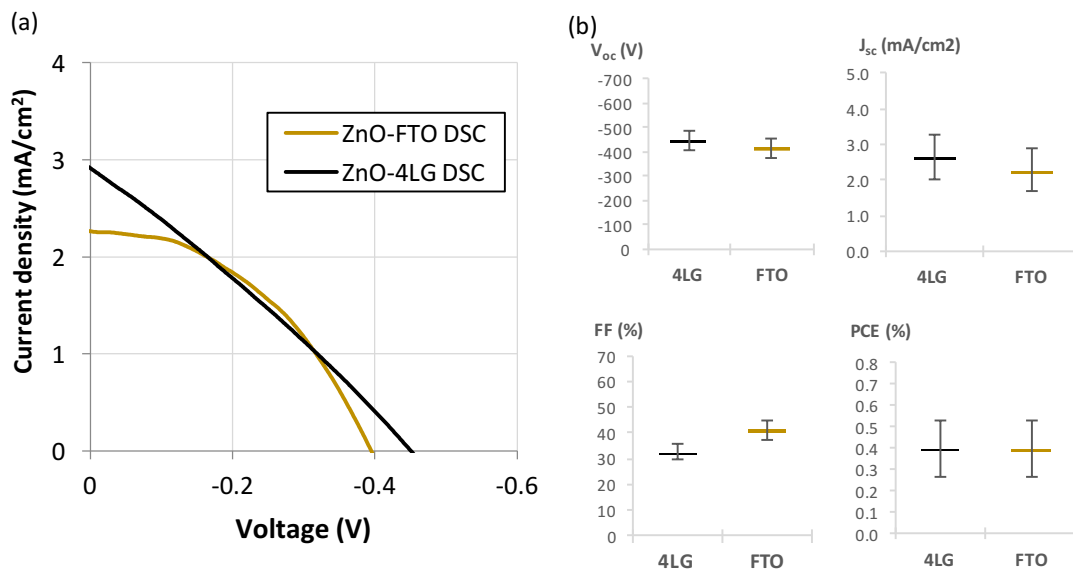
Figure 2.8. **(a) Representative J-V curve of DSCs fabricated with ZG and ZF. (b) Statistical summary of performance parameters V$_{oc}$, J$_{sc}$, FF and PCE for DSC using ZG and ZF, 10 samples were tested for each material**

EIS was used to get insight of the internal charge transport in the DSCs. The Nyquist and Bode plots of representative samples for ach materials are shown in **Figures 2.9(a-b)**. The average values of TC resistance (R_{TC}), and resistance and frequency of charge transfer between the photoanode and the electrolyte (R_{PA} and f_{PA} respectively) are shown in **Figures 2.9(d)**. R_{PA} had similar values for ZG and ZF of 32 and 28 $\Omega.\text{cm}^2$, respectively. f_{PA} also had similar values for ZG and ZF of 7.7 and 9 Hz, respectively. In contrast, the value of R_{TC} was significantly larger for ZG, with a value of 44 $\Omega.\text{cm}^2$ compared to 30 $\Omega.\text{cm}^2$ for ZF. Measurement of OCVD was used to further compare the device kinetics. The electron lifetime τ was calculated using **Equation 1.9** and plotted vs voltage in **Figure 2.9(c)** for representative devices of each material, showing approximately the same value at any voltage. Averaged τ at 200mV is plotted for each material in **Figure 2.9(d)**, with a value of 0.4s for both materials.
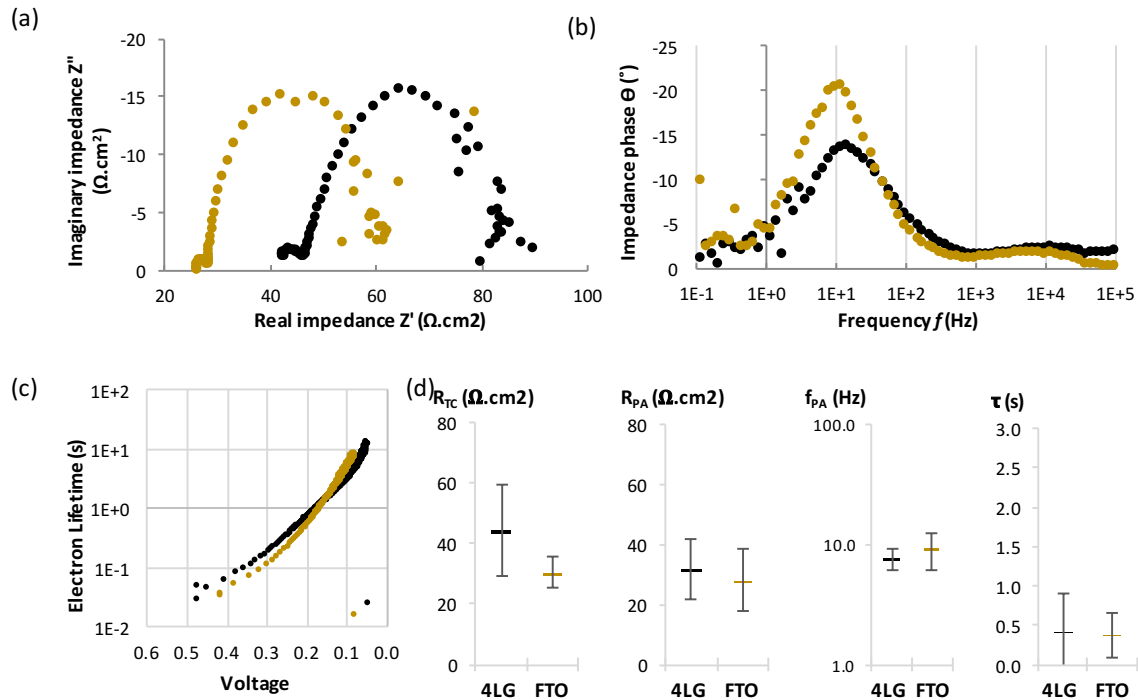
Figure 2.9. **(a) Complex and (b) Bode plot of EIS and (c) electron lifetime (τ) vs voltage for representative DSC fabricated with ZF and ZG as photoanode platform. (d) Statistical summary of internal resistance elements R$_{TC}$ and R$_{PA}$ and kinetic parameters f$_{PA}$ and τ (at 200mV) for fabricated DSC using ZF and ZG, 10 samples were tested for each material**

2.4. Discussion

The stability of graphene after hybridization with ZnO was monitored to ensure compatibility of the fabrication process with the final application. The Raman spectra for bare graphene shows the distinctive G and 2D peaks corresponding to the material, and absence of the D peak (~1350 cm^{-1}), indicating the defect-free nature of the graphene obtained[39]. The variation in I$_{2D}$/I$_G$ between 4LG samples is attributed to random misorientation angles between the stacked graphene crystals, that results in a distribution of interlayer coupling levels and electronic band structures [42, 43]. After ZnO deposition and annealing in Ar, the D peak remains absent, indicating that the graphitic nature is still intact. Annealing in air of bare graphene and graphene coated with ZnO whether in PEG or ButOH paste, did increase the intensity of D peak, which indicates introduction of defects in graphene due to presence of oxygen-containing functional groups. Furthermore, a D` peak appear for all air-annealed samples, which further confirms the introduction of

disorder and defects in the graphene lattice [32, 44]. The Raman spectra indicates oxidation of graphene when annealed in air and explain the open circuit failure of devices annealed in air. In contrats, graphene is not damaged during preparation of the photoanode, if thermal processes are performed in Ar atmosphere. The increase of R for graphene after ZnO coating and annealing in Ar is thus attributed to the increased surface scattering of charges carriers in graphene [45], and not to disruption of the sp^2 lattice.

In regards to the ZnO film, the ZnO Raman peak centered at ~437 cm^{-1} correspond to the E_2 vibrational mode, and a broad peak around 330 cm^{-1}, attributed to a second-order Raman processes [46]. The prevalence of the XRD peak position and relative intensities for ZF and ZG as compared to the commercial ZnO NPs indicate no phase transition during the annealing process. A shift of the peaks towards larger Bragg angle was observed after annealing, which is correlated to increase in NP size due to sintering [47].

ZG DSCs yielded efficiencies comparable to ZF. The contribution of 4LG to the R_s of the cells was found to be only twice the contribution of FTO, both from J-V and EIS analysis, demonstrating that the electron transport is in the same order of magnitude in both TCs under operation. These results are remarkable, considering that the thickness of 4LG was only 0.3% the thickness of FTO, and that the R of 4LG was 50 times larger than for FTO. Illumination and configuration of charge collectors seemed to reduce the effects of TC resistance under DSC operation, due to an increase in charge carrier concentration caused by a photoconductivity effect and the reduction of charge carrier path length[22, 48].

The 4LG is more transparent than FTO in the entire solar spectrum, allowing more photons to reach the photoactive materials. Additionally, graphene has almost 25% higher T compared to FTO in the UV region, where the absorbance of ZnO is maximum. Because of the larger amount of photons reaching the photoactive materials in the ZG DSC, the V_{oc} and J_{sc} were systematically larger than for ZF devices. The higher transparency of 4LG in the UV and visible range increases the photogenerated electrons and upshifts the ZnO Fermi level, causing larger with respect to the redox potential of the electrolyte. Despite ZG-DSCs having larger V_{oc} and J_{sc}, they displayed lower FF than ZF devices. The lower FF in ZG DSCs is attributed to

losses due to larger R of 4LG compared to FTO, which is demonstrated by the larger R_{TC} measured in the EIS. CVD-graphene with very low R is expected to be realizable in a close future, by increasing its μ and n, as the recent milestone achieved of CVD-graphene with μ = 350,000 cm^2/V·s and the many efforts towards large area monocrystalline graphene [49-52], molecular doping [3, 8, 53-58] and simultaneous improvement of R and T [59, 60]. The similar R_{PA}, f_{PA} and τ between ZG and ZF devices indicates that the charge transfer resistance and kinetics in the interfaces are not affected by the choice of TC in this case. The basal plane of graphene has the lowest heterogeneous electron transfer rates amongst carbon allotropes[61], therefore its catalytic activity towards reduction of I_3^- is not larger than that of FTO, demonstrated by similar recombination kinetics observed both in EIS and OCVD of the fabricated DSC.

To our knowledge, this is the first report of FTO-free DSCs using pristine CVD-graphene as the TC and ZnO NPs as the mesoporous semiconductor in the photoanode. The efficiency of these 4LG cells was the same as ZF-DSCs prepared with the same ZnO, Pt and electrolyte elements. Even though many studies have applied graphene as an additive in the photoanode of DSCs, most of them still used tin oxides as the TC material[62]. There are few reports of the application of graphene as TC in the photoanode of tin oxide-free DSCs. In 2014, a TiO$_2$-DSC using CVD-graphene on Pt grids ($\sigma_{dc/op} \approx 107$) was reported with a 0.4% efficiency [5]. The same year another study on CVD-graphene ($\sigma_{dc/op}$=2.2-4.5) reported a 2% efficiency TiO$_2$-DSC [6]. The only work that directly compared the performance of the rGO ($\sigma_{dc/op}$=1.22) with FTO was published in 2008, reporting a TiO$_2$-DSCs with 0.26% efficiency, lower than their FTO reference cell [4]. To our knowledge, there has been no report of equal or better performance for a graphene-photoanode compared to a tin oxide-photoanode fabricated and tested under identical conditions. These previous reports whether did not provide comparison to FTO reference DSCs, or reported a lower efficiency when compared. The stacking of high quality pristine CVD-graphene here used proofs to be a promising approach to produce TCs for large scale applications, with higher $\sigma_{dc/op}$ than rGO or CNT, and lower cost than other strategies, like the use of metal grids.

2.5. Conclusions
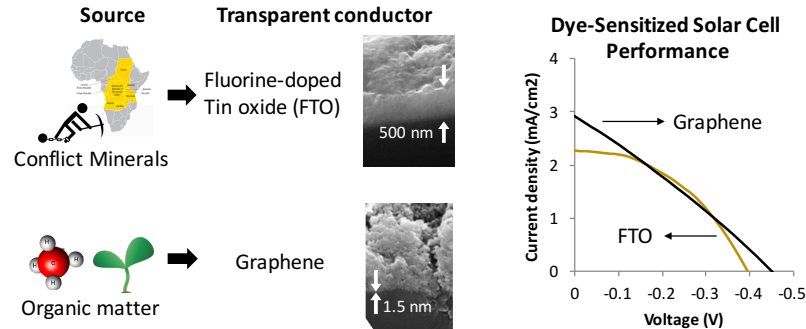
Figure 2.10. Graphene is a competitive alternative to replace tin oxides as transparent conductor in solar cells, its manufacturing can be made more sustainable, and the same performance is observed in DSC application, despite the graphene film having a thickness two orders of magnitude smaller than its counterpart

The results demonstrate that high quality 4LG can compete in performance with FTO for application as TC in the photoanode of DSCs. Annealing of the assembled ZG hybrid in inert atmosphere was found fundamental for the efficient functioning of the cells, as it prevented oxidation of graphene at high temperatures. The devices fabricated with ZG delivered the same PCE as ZF, even though the thickness of 4LG was only 0.3% of the FTO thickness. 4LG is more transparent to all the solar spectrum and up to 25% more in the UV range, resulting in cells with larger V_{oc} and J_{sc}. Larger internal losses in ZG cells, demonstrated by a lower FF in comparison to FTO cells, were found to be caused by graphene's higher R . Replacing traditional tin oxides with graphene in TCs would allow to reduce the costs of raw materials, shrink the weight and thickness of the devices and mitigate the environmental and social impact of their production, while meeting industry's technical requirements to advance towards flexible portable devices. The approach of stacking high quality pristine CVD-graphene is promising to produce TCs for large scale applications, with higher $\sigma_{dc/op}$ than rGO or CNT, and lower cost than metal grids. Our ongoing efforts are focused on optimizing the design of the ZG hybrid for improving the power conversion efficiency of the devices, and on replacing the synthetic dyes with photoactive biomolecules, to advance towards sustainable biophotovoltaics.

2.6. References

1.   Bonaccorso, F.; Sun, Z.; Hasan, T.; Ferrari, A. C., Graphene photonics and optoelectronics. *Nature Photonics* **2010,** *4* (9), 611-622.

2.   Tanemura, M.; Sharma, S.; Kalita, G. Manufacture of single-crystal graphene used for e.g. touchscreen involves thermal decomposition of carbon source which is carbon compound that is arranged in area, arranging board to other area, heating and vaporizing carbon compound. JP2015147706-A.

3.   Han, T.-H.; Lee, Y.; Choi, M.-R.; Woo, S.-H.; Bae, S.-H.; Hong, B. H.; Ahn, J.-H.; Lee, T.-W., Extremely efficient flexible organic light-emitting diodes with modified graphene anode. *Nature Photonics* **2012,** *6* (2), 105-110.

4.   Wang, X.; Zhi, L.; Muellen, K., Transparent, conductive graphene electrodes for dye-sensitized solar cells. *Nano Letters* **2008,** *8* (1), 323-327.

5.   Dong, P.; Zhu, Y.; Zhang, J.; Peng, C.; Yan, Z.; Li, L.; Peng, Z.; Ruan, G.; Xiao, W.; Lin, H.; Tour, J. M.; Lou, J., Graphene on Metal Grids as the Transparent Conductive Material for Dye Sensitized Solar Cell. *Journal of Physical Chemistry C* **2014,** *118* (45), 25863-25868.

6.   Selopal, G. S.; Milan, R.; Ortolani, L.; Morandi, V.; Rizzoli, R.; Sberveglieri, G.; Veronese, G. P.; Vomiero, A.; Concina, I., Graphene as transparent front contact for dye sensitized solar cells. *Solar Energy Materials and Solar Cells* **2015,** *135*, 99-105.

7.   Vaianella, F.; Rosolen, G.; Maes, B., Graphene as a transparent electrode for amorphous silicon-based solar cells. *Journal of Applied Physics* **2015,** *117* (24).

8.   Cui, T.; Lv, R.; Huang, Z.-H.; Chen, S.; Zhang, Z.; Gan, X.; Jia, Y.; Li, X.; Wang, K.; Wu, D.; Kang, F., Enhanced efficiency of graphene/silicon heterojunction solar cells by molecular doping. *Journal of Materials Chemistry A* **2013,** *1* (18), 5736-5740.

9.   De Arco, L. G.; Zhang, Y.; Schlenker, C. W.; Ryu, K.; Thompson, M. E.; Zhou, C., Continuous, Highly Flexible, and Transparent Graphene Films by Chemical Vapor Deposition for Organic Photovoltaics. *Acs Nano* **2010,** *4* (5), 2865-2873.

10.   Kasap, S., Peter, *Springer Handbook of Electronic and Photonic Materials*. Springer US: 2007.

11.   Kumar, A.; Zhou, C., The Race To Replace Tin-Doped Indium Oxide: Which Material Will Win? *Acs Nano* **2010,** *4* (1), 11-14.

12.   Salomons, W., ENVIRONMENTAL-IMPACT OF METALS DERIVED FROM MINING ACTIVITIES - PROCESSES, PREDICTIONS, PREVENTION. *Journal of Geochemical Exploration* **1995,** *52* (1-2), 5-23.

13.   Hertwich, E. G.; van der Voet, E.; Suh, S.; Tukker, A.; M., H.; Kazmierczyk, P.; Lenzen, M.; McNeely, J.; Moriguchi, Y. *Assessing the Environmental Impacts of Consumption and Production: Priority Products and Materials, A Report of the Working Group on the Environmental Impacts of Products and Materials to the International Panel for Sustainable Resource Management*; UNEP: 2010.

14.   Badding, M. A.; Fix, N. R.; Orandle, M. S.; Barger, M. W.; Dunnick, K. M.; Cummings, K. J.; Leonard, S. S., Pulmonary toxicity of indium-tin oxide production facility particles in rats. *Journal of Applied Toxicology* **2016,** *36* (4), 618-626.

15.   Polgreen, L., Congo's Riches, Looted by Renegade Troops. *New York Times* 2008, p 14.

16.   comission, S. a. e., Final Rule-CO**NFLICT MINERALS** 2012.

17.   McWilliams, A., Graphene Technologies, Applications and Markets. *Graphene Technologies, Applications and Markets* **2012**, 147 pp-147 pp.

18.   De, S.; Coleman, J. N., Are There Fundamental Limitations on the Sheet Resistance and Transmittance of Thin Graphene Films? *Acs Nano* **2010,** *4* (5), 2713-2720.

19.   Lee, J.-Y.;   Connor, S. T.;   Cui, Y.; Peumans, P., Solution-processed metal nanowire mesh transparent electrodes. *Nano Letters* **2008,** *8* (2), 689-692.

20.   Mak, K. F.;   Ju, L.;   Wang, F.; Heinz, T. F., Optical spectroscopy of graphene: From the far infrared to the ultraviolet. *Solid State Communications* **2012,** *152* (15), 1341-1349.

21.   Chen, J.-H.;   Jang, C.;   Xiao, S.;   Ishigami, M.; Fuhrer, M. S., Intrinsic and extrinsic performance limits of graphene devices on SiO2. *Nature Nanotechnology* **2008,** *3* (4), 206-209.

22.   Sze, S.; Ng, K., *Physics of Semiconductor Devices*. 3rd ed.; John Wiley and Sons, Inc.: 2006; p 815.

23.   Bolotin, K. I.;   Sikes, K. J.;   Jiang, Z.;   Klima, M.;   Fudenberg, G.;   Hone, J.;   Kim, P.; Stormer, H. L., Ultrahigh electron mobility in suspended graphene. *Solid State Communications* **2008,** *146* (9-10), 351-355.

24.   Chan, J.;   Venugopal, A.;   Pirkle, A.;   McDonnell, S.;   Hinojos, D.;   Magnuson, C. W.;   Ruoff, R. S.;   Colombo, L.;   Wallace, R. M.; Vogel, E. M., Reducing Extrinsic Performance-Limiting Factors in Graphene Grown by Chemical Vapor Deposition. *Acs Nano* **2012,** *6* (4), 3224-3229.

25.   Bae, S.;   Kim, H.;   Lee, Y.;   Xu, X.;   Park, J.-S.;   Zheng, Y.;   Balakrishnan, J.;   Lei, T.;   Kim, H. R.;   Song, Y. I.;   Kim, Y.-J.;   Kim, K. S.;   Ozyilmaz, B.;   Ahn, J.-H.;   Hong, B. H.; Iijima, S., Roll-to-roll production of 30-inch graphene films for transparent electrodes. *Nature Nanotechnology* **2010,** *5* (8), 574-578.

26.   Oregan, B.; Gratzel, M., A LOW-COST, HIGH-EFFICIENCY SOLAR-CELL BASED ON DYE-SENSITIZED COLLOIDAL TIO2 FILMS. *Nature* **1991,** *353* (6346), 737-740.

27.   Mathew, S.;   Yella, A.;   Gao, P.;   Humphry-Baker, R.;   Curchod, B. F. E.;   Ashari-Astani, N.;   Tavernelli, I.;   Rothlisberger, U.;   Nazeeruddin, M. K.; Graetzel, M., Dye-sensitized solar cells with 13% efficiency achieved through the molecular engineering of porphyrin sensitizers. *Nature Chemistry* **2014,** *6* (3), 242-247.

28.   Kazim, S.;   Nazeeruddin, M. K.;   Graetzel, M.; Ahmad, S., Perovskite as Light Harvester: A Game Changer in Photovoltaics. *Angewandte Chemie-International Edition* **2014,** *53* (11), 2812-2824.

29.   Boucle, J.; Ackermann, J., Solid-state dye-sensitized and bulk heterojunction solar cells using TiO2 and ZnO nanostructures: recent progress and new concepts at the borderline. *Polymer International* **2012,** *61* (3), 355-373.

30.   Kamat, P. V., Quantum Dot Solar Cells. Semiconductor Nanocrystals as Light Harvesters. *Journal of Physical Chemistry C* **2008,** *112* (48), 18737-18753.

31.   Badhulika, S.;   Terse-Thakoor, T.;   Villarreal, C.; Mulchandani, A., Graphene hybrids: synthesis strategies and applications in sensors and sensitized solar cells. *Frontiers in Chemistry* **2015,** *3* (38), 19.

32.   Malekpour, H.;   Ramnani, P.;   Srinivasan, S.;   Balasubramanian, G.;   Nika, D. L.;   Mulchandani, A.;   Lake, R.;   Balandin, A. A., Thermal conductivity of graphene with defects induced by electron beam irradtiation. *Nanoscale* **2016,** *8* (30), 14608-14616.

33.   Sarker, S.; Ahammad, A. J. S.; Seo, H. W.; Kim, D. M., Electrochemical Impedance Spectra of Dye-Sensitized Solar Cells: Fundamentals and Spreadsheet Calculation. *International Journal of Photoenergy* **2014**.

34.   Qing, W.; Moser, J. E.; Gratzel, M., Electrochemical impedance spectroscopic analysis of dye-sensitized solar cells. *Journal of Physical Chemistry B* **2005,** *109* (31), 14945-53.

35.   Kern, R.; Sastrawan, R.; Ferber, J.; Stangl, R.; Luther, J., Modeling and interpretation of electrical impedance spectra of dye solar cells operated under open-circuit conditions. *Electrochimica Acta* **2002,** *47* (26), 4213-4225.

36.   Bisquert, J., Theory of the impedance of electron diffusion and recombination in a thin layer. *Journal of Physical Chemistry B* **2002,** *106* (2), 325-333.

37.   Zaban, A.; Greenshtein, M.; Bisquert, J., Determination of the electron lifetime in nanocrystalline dye solar cells by open-circuit voltage decay measurements. *Chemphyschem* **2003,** *4* (8), 859-864.

38.   Li, X.; Magnuson, C. W.; Venugopal, A.; Tromp, R. M.; Hannon, J. B.; Vogel, E. M.; Colombo, L.; Ruoff, R. S., Large-Area Graphene Single Crystals Grown by Low-Pressure Chemical Vapor Deposition of Methane on Copper. *Journal of the American Chemical Society* **2011,** *133* (9), 2816-2819.

39.   Ferrari, A. C., Raman spectroscopy of graphene and graphite: Disorder, electron-phonon coupling, doping and nonadiabatic effects. *Solid State Communications* **2007,** *143* (1-2), 47-57.

40.   Robertson, A. W.; Warner, J. H., Hexagonal Single Crystal Domains of Few-Layer Graphene on Copper Foils. *Nano Letters* **2011,** *11* (3), 1182-1189.

41.   Cancado, L. G.; Takai, K.; Enoki, T.; Endo, M.; Kim, Y. A.; Mizusaki, H.; Jorio, A.; Coelho, L. N.; Magalhaes-Paniago, R.; Pimenta, M. A., General equation for the determination of the crystallite size L-a of nanographite by Raman spectroscopy. *Applied Physics Letters* **2006,** *88* (16).

42.   Niilisk, A.; Kozlova, J.; Alles, H.; Aarik, J.; Sammelselg, V., Raman characterization of stacking in multi-layer graphene grown on Ni. *Carbon* **2016,** *98*, 658-665.

43.   Kim, K.; Coh, S.; Tan, L. Z.; Regan, W.; Yuk, J. M.; Chatterjee, E.; Crommie, M. F.; Cohen, M. L.; Louie, S. G.; Zettl, A., Raman Spectroscopy Study of Rotated Double-Layer Graphene: Misorientation-Angle Dependence of Electronic Structure. *Physical Review Letters* **2012,** *108* (24).

44.   Teweldebrhan, D.; Balandin, A. A., Modification of graphene properties due to electron-beam irradiation. *Applied Physics Letters* **2009,** *94* (1).

45.   Adam, S.; Hwang, E. H.; Galitski, V. M.; Das Sarma, S., A self-consistent theory for graphene transport. *Proceedings of the National Academy of Sciences of the United States of America* **2007,** *104* (47), 18392-18397.

46.   Alim, K. A.; Fonoberov, V. A.; Shamsa, M.; Balandin, A. A., Micro-Raman investigation of optical phonons in ZnO nanocrystals. *Journal of Applied Physics* **2005,** *97* (12).

47.   Spanhel, L.; Anderson, M. A., SEMICONDUCTOR CLUSTERS IN THE SOL-GEL PROCESS - QUANTIZED AGGREGATION, GELATION, AND CRYSTAL-GROWTH IN CONCENTRATED ZNO COLLOIDS. *Journal of the American Chemical Society* **1991,** *113* (8), 2826-2833.

48.   Freitag, M.; Low, T.; Xia, F.; Avouris, P., Photoconductivity of biased graphene. *Nature Photonics* **2013,** *7* (1), 53-59.

49.   Ogawa, Y.; Komatsu, K.; Kawahara, K.; Tsuji, M.; Tsukagoshi, K.; Ago, H., Structure and transport properties of the interface between CVD-grown graphene domains. *Nanoscale* **2014,** *6* (13), 7288-7294.

50.   Van Luan, N.; Shin, B. G.; Dinh Loc, D.; Kim, S. T.; Perello, D.; Lim, Y. J.; Yuan, Q. H.; Ding, F.; Jeong, H. Y.; Shin, H. S.; Lee, S. M.; Chae, S. H.; Quoc An, V.; Lee, S. H.; Lee, Y. H., Seamless Stitching of Graphene Domains on Polished Copper (111) Foil. *Advanced Materials* **2015,** *27* (8), 1376-+.

51.   **Lin, L.**; **Li,** J.; R**en, H.**; Koh, A. **L.**; Kang, N.; Peng, H.; **Xu, H.** Q.; Liu, Z., Surface Engineering of Copper Foils for Growing Centimeter-Sized Single-Crystalline Graphene. *ACS Nano* **2016,** *10* (2), 2922-2929.

52.   **Banszerus, L.**; **Schmitz, M.**; **Engels, S.**; **Dauber, J.**; **Oellers, M.**; **Haupt, F.**; **Watanabe, K.**; **Taniguchi, T.**; **Beschoten, B.**; **Stampfer, C.**, Ultrahigh-mobility graphene devices from chemical vapor deposition on reusable copper. *Science Advances* **2015,** *1* (6), 1-6.

53.   Dao, V.-D.; Jung, S.-H.; Kim, J.-S.; Tran, Q. C.; Chong, S.-A.; Larina, L. L.; Choi, H.-S., AuNP/graphene nanohybrid prepared by dry plasma reduction as a low-cost counter electrode material for dye-sensitized solar cells. *Electrochimica Acta* **2015,** *156*, 138-146.

54.   Goncher, S. J.; Zhao, L.; Pasupathy, A. N.; Flynn, G. W., Substrate Level Control of the Local Doping in Graphene. *Nano Letters* **2013,** *13* (4), 1386-1392.

55.   Xu, C., Paul A.Lu, JingShuford, Kevin L., Electronic properties of halogen-adsorbed graphene. *The Journal of Physical Chemistry C* **2015**.

56.   Gunes, F.; Shin, H.-J.; Biswas, C.; Han, G. H.; Kim, E. S.; Chae, S. J.; Choi, J.-Y.; Lee, Y. H., Layer-by-Layer Doping of Few-Layer Graphene Film. *Acs Nano* **2010,** *4* (8), 4595-4600.

57.   Khrapach, I.; Withers, F.; Bointon, T. H.; Polyushkin, D. K.; Barnes, W. L.; Russo, S.; Craciun, M. F., Novel Highly Conductive and Transparent Graphene-Based Conductors. *Advanced Materials* **2012,** *24* (21), 2844-2849.

58.   Chan, K. T.; Neaton, J. B.; Cohen, M. L., First-principles study of metal adatom adsorption on graphene. *Physical Review B* **2008,** *77* (23).

59.   Bao, W.; Wan, J.; Han, X.; Cai, X.; Zhu, H.; Kim, D.; Ma, D.; Xu, Y.; Munday, J. N.; Drew, H. D.; Fuhrer, M. S.; Hu, L., Approaching the limits of transparency and conductivity in graphitic materials through lithium intercalation. *Nature Communications* **2014,** *5*.

60.   Choi, D.; Kuru, C.; Choi, C.; Noh, K.; Hwang, S.; Choi, W.; Jin, S., Unusually High Optical Transparency in Hexagonal Nanopatterned Graphene with Enhanced Conductivity by Chemical Doping. *Small* **2015,** *11* (26), 3143-3152.

61.   Villarreal, C. C.; Pham, T.; Ramnani, P.; Mulchandani, A., Carbon allotropes as sensors for environmental monitoring. *Current Opinion in Electrochemistry* **2017,** *3* (1), 106-113.

62.   Kilic, B.; Turkdogan, S., Fabrication of dye-sensitized solar cells using graphene sandwiched 3D-ZnO nanostructures based photoanode and Pt-free pyrite counter electrode. *Materials Letters* **2017,** *193*, 195-198.

Chapter II:

Characterization of the Heterojunction Microstructure for Electrodeposited Vertical ZnO Nanorods on CVD-Graphene

Abstract

A low-cost heterostructure of a wide-bandgap nanostructured semiconductor on top of a transparent conductor (TC) fabricated from abundant sustainable materials is of great interest for optoelectronic devices, such as heterojunction photovoltaic cells. Due to its high optical transparency and electron mobility, graphene is an attractive carbon-based material to replace the traditional TCs (i.e. ITO). However, for the industrial application of graphene as TC, it is necessary to interface it with other materials, like oxides, while maintaining the sp^2 carbon network that provides its excellent electronic properties. We report the electrodeposition of ZnO on graphene optimized to obtain a textured layer of vertically aligned crystalline semiconducting nanorods (ZVNRs) evenly coating the graphene surface. Lattice distortions and mosaicity in the crystals indicate that the ZVNRs grow under out-of-plane compressive strain. The stability of the sp^2 network of graphene during *in situ* growth of ZnO is demonstrated using Raman spectroscopy from the front and backside of the heterostructure, in a novel approach to investigate junctions of 2D-3D nanomaterials. Despite the structural stability of graphene, its sheet resistance (R) is found to increase with ZVNRs electrodeposition, which can be attributed to reduction of mobility due to charge carrier scattering, reduction of carrier concentration due to doping or interfacial strain. The cathodic electrodeposition is an effective and versatile method to grow crystalline nanostructures in the surface of single layer-graphene while protecting its sp^2 hybridization, while it provides relative fast deposition rates, affordability, and low processing temperatures that would allow the use of polymeric flexible substrates. These findings on interfacial properties are important to advance the functionality of graphene as TC material and develop nano-heterostructures for myriad technological applications.

3.1. Introduction

An array of vertically-aligned ZnO nanorods on graphene (ZVNR/G) is a heterostructure of great interest for applications in next-generation flexible optoelectronics including photovoltaics, displays and smart windows, as well as piezoelectric nanogenerators and sensors [1-3]. 1D semiconductor nanostructures provide space-confinement for electrical charges [4] and large surface area for light scattering and absorption, while allowing minority charge carriers to move radially towards the junction before recombination occurs. This is especially useful for inexpensive materials with high crystal defects density and short diffusion length [4, 5]. Nanostructured ZnO and TiO_2 are leading low-cost semiconductors used in the photoanode of heterojunction solar cells, in which they are sensitized with photoactive materials like dyes, perovskites, quantum dots, polymers, plasmonic nanoparticles and biomolecules to expand their solar spectrum absorbance range[6-12]. Such photoanodes are built on the surface of a transparent conductor (TC) whose function is to collect the generated electrons and transport them to the external circuit of the solar cell. The current market of TCs is primarily comprised of doped tin oxides, which are brittle, costly, pose health hazards and are partly produced from conflict minerals like cassiterite [13, 14]. For these reasons, there are growing efforts to find convenient, affordable and sustainable TC alternatives. ZnO itself has been proposed as TC, but the performance is limited by its low charge carrier mobility. Approaches to increase ZnO mobility, such as aluminum doping (i.e. AZO coatings) have even reached successful commercial scales, demonstrating the need in the market for cost-effective alternatives [15, 16]. The use of a graphene layer under the ZnO film has been shown to be effective in increasing the intrinsic mobility of ZnO [17]. The application of graphene as TC in solar cells has experienced a tremendous growth in recent years, due to its high transparency and charge carrier mobility [18, 19]. Recently, for example, a semitransparent and flexible solar cell fabricated with all-graphene electrodes was reported [20]. The experimental studies with the model ZVNR/G system are of great importance for the field of graphene hybrids in general.

Many challenges need to be addressed before heterostructures of graphene and oxides achieve industrial scale production. The preservation of electronic properties may be relevant when making a graphene-based heterostructure. The sheet resistance allows to easily monitor the electronic transport in graphene during hybridization, and is correlated to the effective mobility (μ), the film thickness (t), and the majority carrier density (n), according to Equation 3.1.

$$R = (q\mu n t)^{-1}$$ **Equation 3.1**

Where q is the electron charge [21]. Since the majority of the atoms in graphene are on the surface, the sp^2 network that provide its outstanding mobility is jeopardized by the interface formation with an oxide [22]. Therefore, graphene instability in oxidizing conditions limits the methods that can be used to fabricate hybrids, such as chemical vapor deposition at high temperature (>400°C) in air [23]. The *in situ* synthesis of ZnO nanostructures can be done by methods more compatible with graphene than its counterpart, TiO_2. ZnO also surpasses TiO_2 in terms of electron mobility [4, 24]. The electronic band structure of graphene and ZnO is favorable for electron transport at the interface, because the work function of ZnO (~5.3eV) is larger or equal to that of graphene (~4.4-5.3eV), resulting in ohmic contact [25].

Cathodic electrodeposition is an *in-situ* approach to grow ZVNRs on graphene that is simple, affordable and fast. **Figure 3.1** illustrates the experimental setup and reaction mechanisms taking place during ZnO electrodeposition.
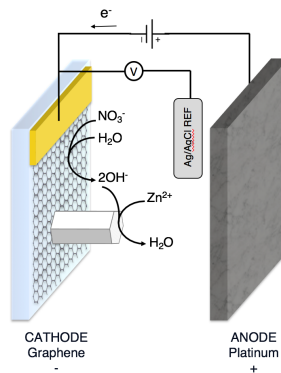
Figure 3.1. Schematics of electrodeposition setup and reaction mechanisms for *in situ* growth of ZVNRs on graphene

The generation of OH⁻ ions in the negatively charged graphene surface increases the pH near the cathode, causing the zinc ions to react with hydroxyl ions and resulting in the precipitation of ZnO, leading to deposition on the substrate according to **Equations 2 and 3** [26, 27].

$$NO_3^- + H_2O + 2e^- \rightarrow NO_2^- + 2OH^- \qquad \textbf{Equation 2}$$

$$Zn^{2+} + 2OH^- \xrightarrow{temp} ZnO + H_2O \qquad \textbf{Equation 3}$$
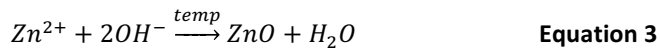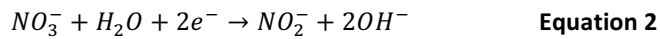
Cathodic electrodeposition avoids the exposure of graphene to oxidizing conditions, surpassing other methods like metal-organic vapor phase epitaxy, hydrothermal and chemical vapor deposition [25, 28, 29]. Furthermore, the structural characteristics of the ZVNR/G, such as crystallinity, texture and density, can be easily controlled by changing the electrodeposition variables.

The electrodeposition of ZnO on reduced graphene oxide (rGO) and partially oxidized bi-layer chemical vapor deposition (CVD)-graphene were initial approaches to produce the ZVNR/G heterostructure [30, 31]. However, these graphene varieties presented poor performance as optoelectronic materials due to their limitations of low mobility, lower optical transmittance, high interlayer resistance between rGO flakes, oxygen defects and rupture of the sp^2 bond. Pristine CVD-graphene has better optoelectronic properties for the application as TC [32] and its use as substrate for ZVNR electrodeposition has been reported recently [33]. The use of pristine CVD-graphene has additional advantages because the basal plane of graphitic materials displays slower rates of charge transfer with redox mediators than rGO or oxidized varieties of graphene [34], resulting in reduced recombination losses as photoanode platform for heterojunction photovoltaic devices.

In this work, **the electrodeposition of ZnO on high-quality CVD-graphene has been optimized to obtain a continuous array of ZVNRs and the resulting heterostructure is characterized**. The structure of the ZVNRs is determined by XRD, SEM and selected area electron diffraction (SAED) in Transmission Electron Microscope (TEM). **The structure of graphene is studied by Raman spectroscopy from both sides of the junction, in a novel approach to characterize 2D-3D heterostructures of nanomaterials**. The sheet

resistance of the graphene is monitored to understand the effect of the ZnO growth on the electron transport across the TC. This work contributes to the development of the ZVNR/G hybrid from an application perspective. This heterostructure can be synthesized from abundant resources by low-cost methods with myriad applications in flexible optoelectronic and other transducing devices.

3.2. Experimental Procedures

The continuous graphene film was grown on Cu foil using ambient-pressure CVD, with diluted methane as carbon source (≈90ppm) [35]. The CVD-graphene was spin-coated on one side with PMMA. 1LG was prepared following the details on graphene synthesis described in section 2.2.1. The samples for characterization from top- and back-side of the heterostructure were prepared as illustrated in **Figure 3.2**. For the top side analysis, the copper was etched in $FeCl_3$ and the graphene/PMMA film was transferred onto a clean glass substrate, with the graphene in contact with the glass. The PMMA was dissolved in acetone and a Cr/Au contacts were e-beam evaporated. The ZVNRs carpet was electrodeposited from a 10mM $Zn(NO_3)_2$ aqueous solution on the negatively biased graphene using a CHI 660C electrochemical station and a three-electrode configuration with Pt counterlectrode and Ag/AgCl$_{sat'd}$ KCl reference electrode, as illustrated in **Figure 3.1**. PMMA was used as dielectric coating to prevent electrodeposition on the metallic contact, which would hinder ZnO growth on the graphene. The galvanostatic deposition was applied for 30 minutes while stirring. The current density was optimized for the best quality crystals, considering that ZVNRs morphology is obtained on graphene between 0.1 and 1 mA/cm^2 at 75˚C [26]. For the back-side characterization, the floating graphene/PMMA film was scooped to a polystyrene (PS) sheet with the PMMA in contact with the PS [36]. The copper was etched in $FeCl_3$ and the metallic contacts were e-beam evaporated. Then the ZVNR carpet was electrodeposited on top following same conditions as described above. The top-side of the graphene/ZVNR was then coated with PDMS, and the sacrificial PMMA/PS dissolved in acetone, leaving the backside of the graphene exposed for characterization.
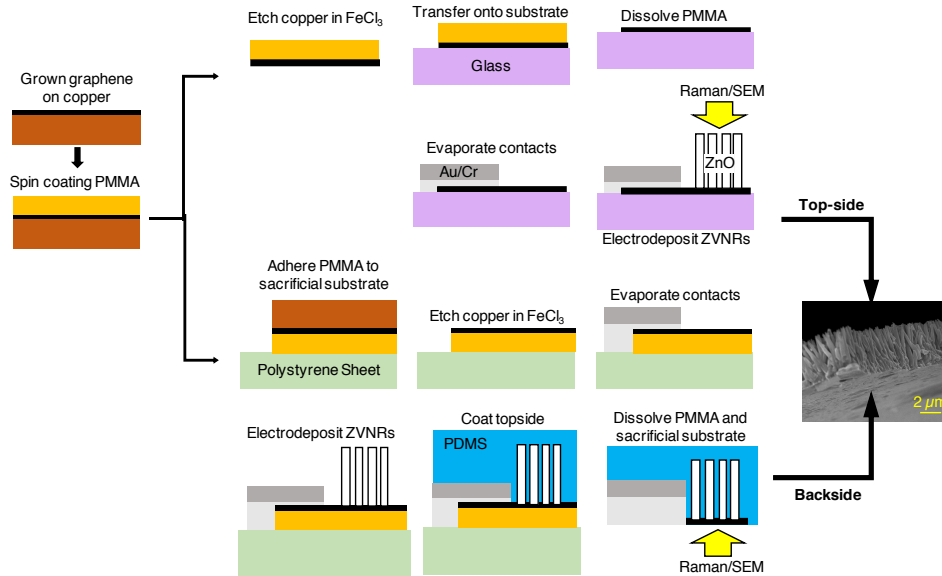
Figure 3.2. **Schematics of ZVNR/Graphene heterostructure preparation for interface characterization**

The structure of the ZVNR/G was characterized using X-Ray diffraction, Raman spectroscopy, scanning electron microscopy (SEM) and selected area electron diffraction (SAED). XRD measurements were taken at room temperature with the Empyrean diffractometer from Panalytical, using a copper anode at 40 mA and 45 kV and step size of 0.0260°. The Raman spectra were obtained using a Horiba Scientific LabRam Monochromator equipped with a 532 nm laser. SEM was performed using the FEI NovaNanoSEM 450. The ZVNRs were scraped off and sonicated in water for SAED, which was obtained with an FEI Tecnai12 TEM at 120kV. The R of graphene was calculated from the bulk resistance (R_B) of a two-terminal device on glass with the formula $R = R_B \cdot W/L$, where W is the width of the graphene area and L as the length between contacts, method that was validated against four-point measurements.

3.3. Results

The *in situ* growth of 1D ZnO nanostructures on graphene was performed with galvanostatic electrodeposition. The effect of the current density on the ZnO morphology is observed in the SEM micrographs of **Figure 3.3(a-c)** and on its crystal structure by XRD in **Figure 3.3(e)**. The XRD spectra were indexed to the ZnO wurtzite crystal structure (JCDP 36-1451), with the hexagonal space group P63mc (a=b=3.25 Å, c=5.21 Å, $\alpha=\beta=90°$, $\gamma=120°$). At 0.3 mA/cm^2 the ZVNRs grow with low crystallinity and poor alignment. As the current density is increased to 0.4 mA/cm^2 the crystallinity and texture of the material increases, with the (0001) plane predominant in the diffractogram, parallel to the graphene's surface. Very weak diffraction peaks corresponding to the ZnO ($10\bar{1}1$) and ($10\bar{1}0$) planes are also observed, which arise from slightly tilted nanorods. At the highest current density of 0.5 mA/cm^2 the ZnO film still shows high crystallinity and texture but a new hollow morphology of vertically-aligned nanotubes appears (ZVNTs). Lower current densities have been correlated to crystal nucleation in the electrolyte, and later anchoring of the grown nanoparticles on the electrode surface, which could result in the random orientation of the NRs observed at 0.3mA/cm^2. As the current density is increased to 0.4mA/cm^2, ZnO supersaturates faster in the precursor solution, and nucleation occurs directly on the electrode, resulting in heteroepitaxy and a more organized ZVNRs array. Alternating layers of Zn$^+$ and O$^-$ are deposited as shown in **Figure 3.3(d)**, attracted towards the c-plane due to its strong polarity, resulting in anisotropic growth of solid ZVNRs in the c-direction [27, 37]. When higher current density of 0.5mA/cm^2 is applied, the axial screw dislocation crystal becomes the growth driving force, as shown in F**igure 3.3(d)**. The self-perpetuating growth spirals enable anisotropic growth, and the dislocation strain energy overcomes the surface energy required for filling the inner surface, forming hollow ZVNTs spontaneously, a mechanism observed at low precursor concentration in hydrothermal growth [38]. The current density of 0.5mA/cm^2 drives faster reaction rates that rapidly reduce the precursor ions concentration close to the surface, resulting in the observed tubular morphology. The current density of 0.4 mA/cm^2 was chosen for further studying the highly crystalline and textured layer of

solid ZVNRs on graphene. However, the hybrid of ZVNTs/G results interesting for future study, as tubular solar cells have been reported in literature to yield 2.7-fold increase in efficiency compared to the original solid nanorods [39].
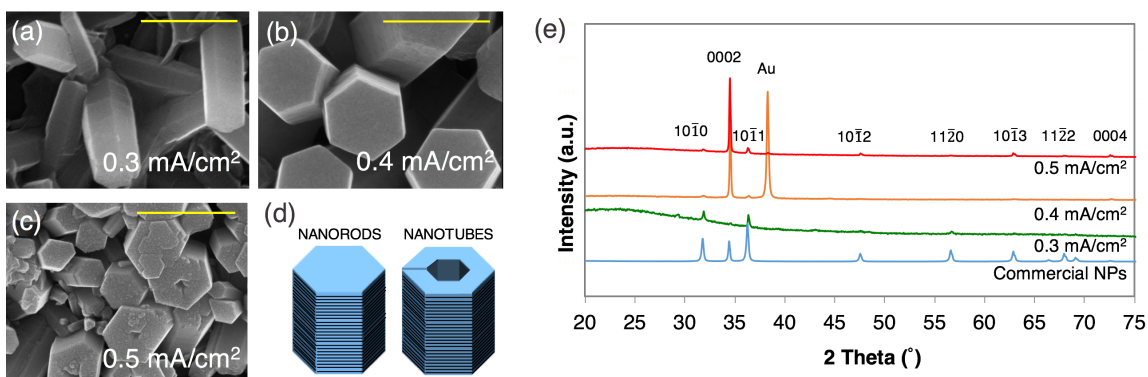
Figure 3.3. SEM micrographs of ZnO nanostructures electrodeposited on graphene with different current densities (a) 0.3mA/cm², (b) 0.4mA/cm², (c) 0.5mA/cm². Scale bar 500nm. (d) Schematics of the nanostructures obtained and their (e) X-ray diffractograms, background gold peak corresponds to electric contacts.

The potential as a function of time during galvanostatic deposition of vertically-aligned ZnO nanorods (ZVNRs) with current density of 0.4mA/cm², precursor concentration of 10 mM $Zn(NO_3)_2$, mixing and temperature of 75°C is illustrated in **Figure 3.4**. The reaction starts at relatively low potential, corresponding to the nucleation phase, followed by a steady potential of ~ -0.9 V vs Ag/AgCl$_{sat'd KCl}$ after ~ 120 s at which the growth stage takes over. At this current density, solubility of ZnO fastly saturates in the precursor solution, and nucleation occurs directly on the electrode[37].
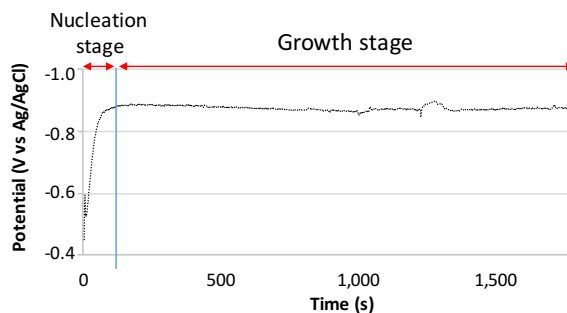
Figure 3.4. Electrode potential as a function of time during galvanostatic deposition of vertically-aligned ZnO nanorods (ZVNRs) with current density of 0.4mA/cm², precursor concentration of 10 mM $Zn(NO_3)_2$, mixing and temperature of 75°C.

60

The SEM micrographs of the ZVNR/G electrodeposited at 0.4 mA/cm^2 observed from the top-side and cross-section of the heterojunction are shown in **Figures 3.5(a-d)**. The anisotropic growth of the ZnO results in a texturized film of vertically aligned hexagonal crystals. The obtained alignment is ascribed to the heteroepitaxial growth of the ZnO nanostructures on graphene [40, 41]. In the VNRs, the {0001} faces of the crystals are rough, due to rapid growth along the *c* axis. In contrast, prismatic faces, corresponding to {01$\bar{1}$0} or {2$\bar{1}\bar{1}$0}, are smooth and well-developed, due to slow growth, and reveal the lamellar structure of the Zn+ and O- ionic layers that stack up along the 0001 direction [27]. The backside of the junction is also observed in SEM micrograph in **Figure 4(e)**, showing the flat morphology of graphene and a crack through which the ZVNRs can be seen on the other side. The homogeneous contrast of the surface indicates an evenly covered graphene, a desirable feature for preventing shunt contact of the graphene with the hole acceptor in p-n junction device applications.
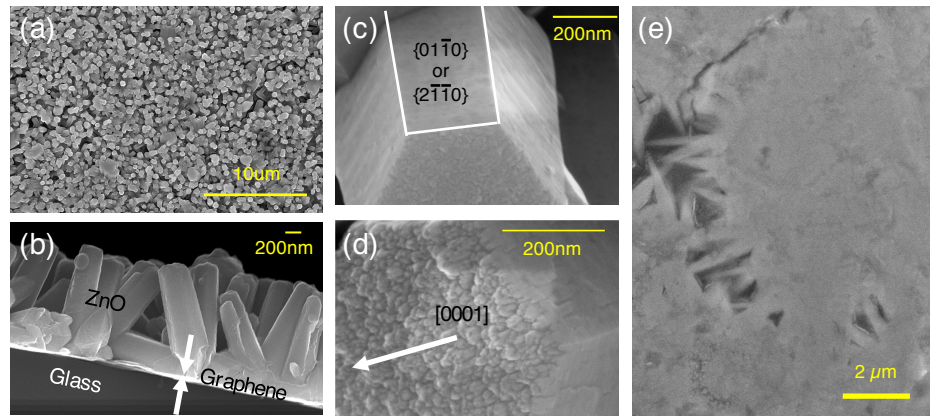
Figure 3.5.   ZVNR/Graphene hybrid grown by electrodeposition (a) top-view and (b) cross-section of the heterostructure, (c) close-up of the walls of the nanorods, (d) close-up of the tip of the nanorods, (e) backside of the heterotructure.

The density of ZVNRs grown on the graphene from 10mM Zn(NO$_3$)$_2$ was 3.4 x 10^8 /cm^2, with diameter of 364 $\pm$ 48 nm, length of 0.9 $\pm$ 0.1 μm and surface to volume ratio estimated to be 13.8 /μm. The diameters here obtained were larger than the 200nm ZVNRs electrodeposited on rGO [30], probably because they used a lower concentration of 1mM ZnCl$_2$ salt and deposited a seed layer before growth. Our ZVNRs also had

larger diameter than the 250nm ZVNRs grown on oxidized CVD-graphene from 5mM $Zn(NO_3)_2$ [31], for which

no seed layer was used. These results support the mechanism proposed for the ZnO deposition on graphene

in which the hydroxyl groups (OH−) contained in the solution attach to the defect sites, leading to nucleation

and growth [42]. The rGO surface offers higher density of defects than pristine CVD-graphene, that act as

electroactive sites, for example, rGO has heterogeneous electron transfer rates in $Fe(CN)_6^{3-/4-}$ that are 10^4

times faster than CVD-graphene [34]. Because the defect density of the pristine CVD-graphene is lower than

rGO or oxidized graphene, the nanorod density obtained is lower too. The use of seed layer or other

functional groups on the surface of graphene would reduce the diameter and increase the density of the

VNRs, which is desirable for applications of large surface area-nanostructured semiconductors. Using a

pristine graphene with low defect density allows to maximize the mobility along the graphene sp^2 network,

therefore oxidation steps are undesirable for electronic application of the hybrid.

A characteristic crystal distortion in the ZVNRs/G is displayed in Figures 3.6(a-f) with red arrows, where

the ZVNRs become tapered close to the base. This distortion indicate that the ZnO grow in compressive

pseudomorphic epitaxy on graphene, supporting the ZnO/G interface structure previously predicted [40]. The

lattice mismatch generates a compressive strain on the ZVNR film for the in-plane direction and a tensile

strain for the out-of-plane direction. Such atomic arrangement is not in equilibrium, and after a critical

thickness value, the lattice of the ZnO film relaxes to its bulk dimensions, accompanied by distortion of the

crystal shape [43], as shown in the TEM micrograph in **Figure 3.6(g)**. NRs of smaller dimensions are expected

to result in coherent mismatch strain relief, but due to relatively large diameter of our ZVNRs, the lattice

mismatch strain is accommodated with misfit dislocations that form steps in the crystal shape [44].
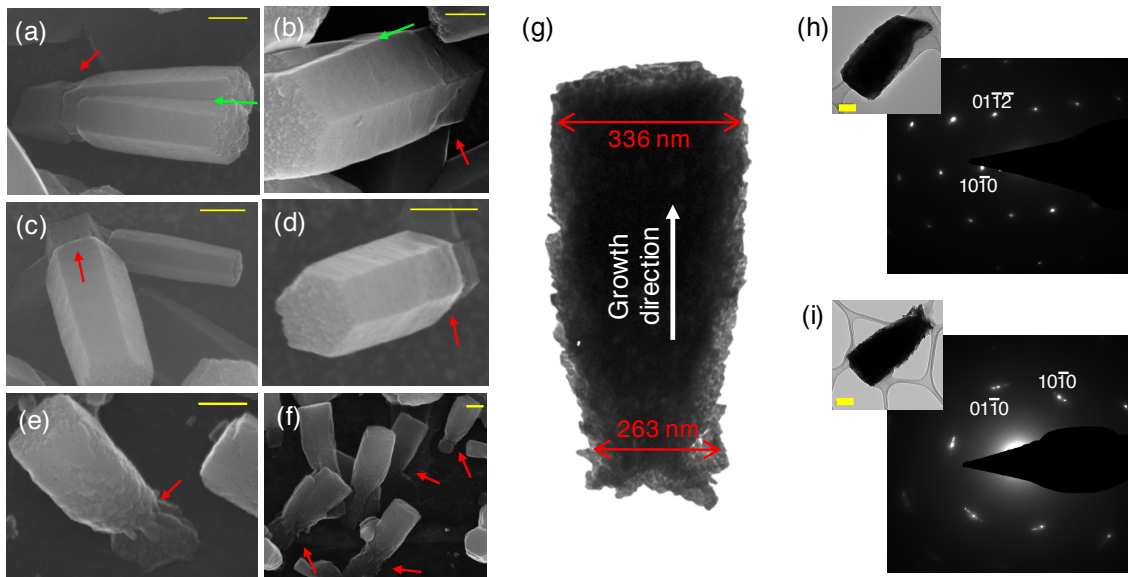
Figure 3.6. **(a-f) SEM micrographs of crystal distortion in electrodeposited VNRs on graphene indicated by red arrows, and quasi-parallel crystal growth in green (g) bright-field TEM micrograph and dimensions of a monocrystalline ZVNR grown on graphene (h-i) Electron diffraction patterns and bright-field TEM images for ZVNRs. Scale bars 200nm**

Selected area electron diffraction (SAED) was used to determine the crystal structure of individual ZVNRs. A fraction of the ZVNRs yielded a diffraction pattern with resolved individual diffraction spots, like the one shown in **Figure 3.6(h)**, corresponding to single crystalline wurtzite structure taken with electron beam parallel to the $[1\bar{2}16]$ zone axis. Other VNRs produced a diffraction pattern like the one in **Figure 3.6(i)** near the $[0001]$ zone of wurtzite, that displays a broadening of the diffraction spots streaking into arcs, which is known as mosaicity. A mosaic crystal consists of numerous smaller perfect crystals with slight misalignment and is characteristic of strained lattices. The spread of spot intensity profile in the azimuthal direction corresponds to the grain twist component, caused by a rotation about the c-axis, reported for other wurtzite systems in literature and thought to arise from edge dislocation and oxygen-related strain-relieving defects [45, 46], which are expected from the lattice mismatched interface of ZVNR/G. The 2-3˚ mosaicity here obtained indicates narrow spread of grain orientation. SEM micrographs in **Figures 3.6(a,b)** show crystal defects with green arrows that support the proposed quasi-parallel crystal growth in the $[0001]$ direction. Our results are consistent with recent reports of ZnO atomic layer deposition (ALD) on

different substrates, where mosaicity appears under compressive pseudomorphic growth, as on SiC [47]. The obtained crystalline structure provides a fast and easy path for photoelectron extraction along the *c*-direction, because of the absence of grain boundaries, which is an advantage over NP arrays for optoelectronic applications [4].

In **Figure 3.7** it can be observed that the strain challenges the adhesion at the interfaces and the mechanical stability of the film resulting in delamination. This is especially observed when the heterostructure is brought in contact with water for rinsing, probably due to the hydrophilicity of glass and poor bond energy between glass and graphene. This challenge could be overcome by using a soft hydrophobic polymer substrate instead of glass, that would partially absorb the strain of the film with its flexibility, or by functionalizing the glass with graphene-binding molecules.
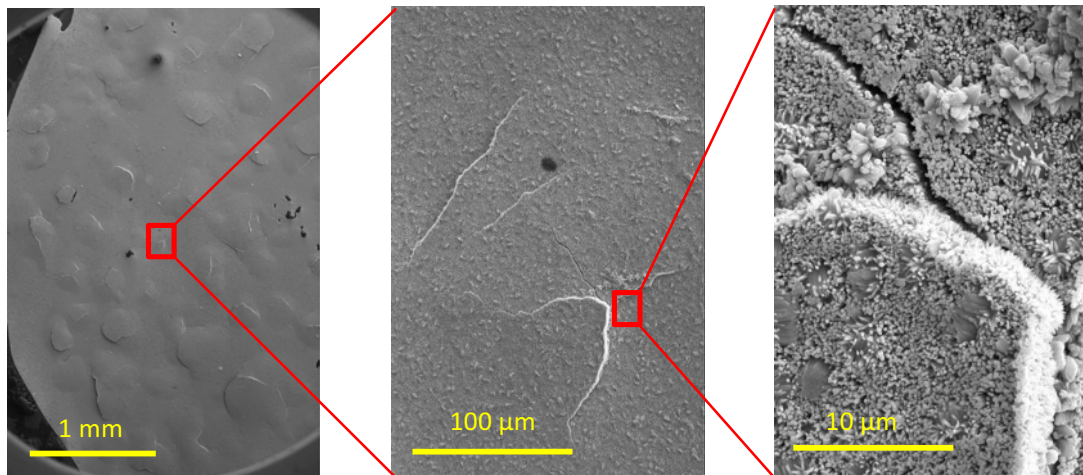
Figure 3.7.   The mechanical failure observed for the ZVNR/G hybrid (peeling-off), consistent with an in-plane compressive and out-of-plane tensile strain due to the lattice mismatch of graphene and ZnO in a heteroepitaxial thin film growth

The extreme thinness of 2D materials makes it difficult to identify defects, even with electron beam, and our SEM characterization failed to provide information about the structure of 0.3 nm-thick graphene after ZnO electrodeposition. Optical spectroscopic techniques are more revealing to determine damage of 2D materials crystal structure [48]. The prevalence of the sp^2 structure of the CVD-graphene is therefore studied with Raman shift spectra, as shown in **Figure 3.8(a)**, from the top- and back-sides of the junction. A

PDMS substrate is used to obtain the spectrum from the backside of the heterostructure, which introduces additional peaks that are shown in the reference red spectrum. The spectra of ZVNR/G exhibit the characteristic fingerprint of both materials. The peaks for ZnO hexagonal wurtzite nanostructures below $500cm^{-1}$ correspond to a sharp and intense E2 peak centered around 437 cm^{-1} denoting the wurtzite lattice of ZnO nanorods, and a broad peak around 330 cm^{-1}, attributed to a second-order Raman scattering processes [49]. The characteristic peaks for graphene are displayed from both sides of the junction. The G peak is observed at ~1590 cm^{-1} that corresponds to the bond stretching of all pairs of sp^2 atoms in both rings and chains, and the second order 2D peak at ~2690 cm^{-1} corresponding to E_{2g}-vibration mode of sp^2 carbon[50]. The ratio of I_{2D}/I_G was variable along the surface from 0.8 to 4, indicating a continuous single layer graphene, with patches of 2- and 3-layer graphene nuclei, typical of CVD-graphene [51]. The position of G and 2D peaks didn´t change after the ZVNR growth. The D peak at 1350, correlated to structure defects of sp^3 domain, is mostly absent from the top-side, and from the backside the average ratio of D to G peak (I_D/I_G) was 0.08 ± 0.05. In comparison, the I_D/I_G for pristine CVD-graphene has been reported to increase above 1 after hydrothermal growth of VNRs, attributed to generation of defects [52]. Exposure to oxygen plasma for 1s resulted in I_D/I_G ratio of ~1.7 [53] and exposure to UV-ozone treatment for 5 min increased the I_D/I_G to ~1.2 [54]. The low relative intensity of the D peak after ZnO electrodeposition is indicative of the retention of the pristine structure of graphene. The low I_D/I_G ratio also indicates that the two materials are held together by physical forces rather than by chemical bond, even though the graphene-ZnO bond prepared by hydrothermal has been observed to be very strong, with higher experimental and theoretical mechanical stability than the $ZnO-SiO_2$ bond [41].
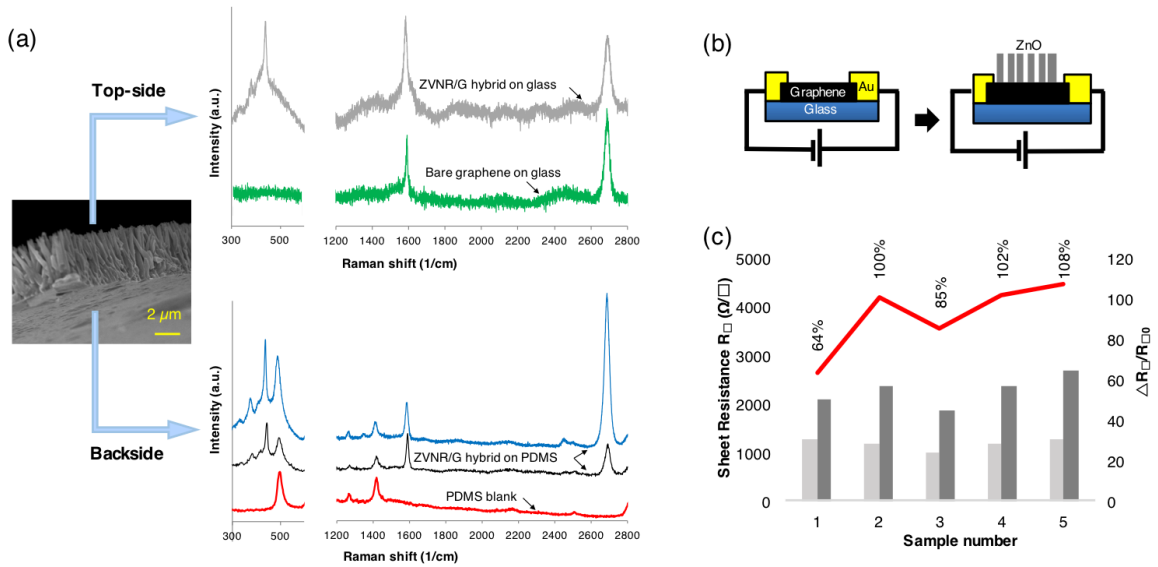
Figure 3.8. a) Raman shift spectra for ZVNR/G hybrid taken from the top and bottom sides of the heterostructure b) schematic of experimental measurement and c) $R_\square$ change for graphene after deposition of ZnO

The sheet resistance of the graphene was monitored experimentally with the $R_\square$ of 2-terminal devices before and after ZnO electrodeposition, as shown in **Figure 3.8(b,c)**. Even though no significant damage to the sp^2 network was detected with Raman spectroscopy, an increase of $R_\square$ between 65-108% was measured. In comparison, exposure to UV-ozone treatment for 5 min has been reported to increase the $R_\square$ by more than one order of magnitude [54]. The increase of $R_\square$ for graphene could be explain on base of **Equation 3.1**, caused by a reduction of mobility μ due to the ZVNRs acting as scattering centers for the carriers that travel along the surface of graphene, which is a general phenomenon predicted for graphene [55] and experimentally demonstrated for the ZnO/G system [17]. The $R_\square$ increase could also be attributed to a change in carrier concentration due to doping [56]. Density functional theory has predicted considerable charge transfer at the interface of graphene and (0001)-terminated ZnO, which would significantly modify the electronic properties of pristine graphene. Zn-terminated surfaces are predicted to have stronger binding energies than O-terminated surfaces, and to enrich the charge density of the π-orbital of the graphene sheet, while O-terminated surfaces would induce hole-doping [57]. The graphene prepared and

66

transferred with our methods is intrinsically p-doped, exhibiting Dirac voltages (V_{Dirac}) of 45 to 65V as shown in the transfer characteristic in **Figure 2.1(a)**, and hole mobility of 4723 ± 621 cm^2/V.s as shown in **Figure 2.1(b)**. Therefore, the increase of $R_\square$ in this case would be explained by reduction of hole density due to recombination with additional electrons transferred from the Zn-terminated surface. The reduction of conductance could also be a result of interface strain effects, which can dominate the materials properties, especially for 2D nanomaterials [58].

The *in situ* growth of ZVNR on graphene has been reported by a variety of methods, but the stability of the carbon monoatomic layer is often not characterized directly, and remains unclear if its outstanding electric performance holds after hybridization. For example, researchers concluded that graphene is not damaged after ZVNR growth by thermal CVD and MOVPE in presence oxygen above 400°C based on the indirect technique of photoluminescence that shows absence of carbon atoms incorporated in the ZVNRs [59, 60]. However, this is not a valid statement, as the graphene can oxidize completely towards CO_2 in such conditions, and still leave no residues on the ZnO. We have found that heating above 400°C two-terminal pristine CVD-1LG and 4LG, as well as ZVNR/1LG and ZVNR/4LG devices, in the presence of 1% oxygen results in open circuit failure in 100% of the cases. The rupture of the metal contact-graphene contact has been dismissed as the cause of device failure by re-depositing the Cr/Au contact. If graphene oxidizes when growing other materials on its surface, its sp^2 network would be disrupted and it would only serve as a buffer or sacrificial substrate [61]. The application of the ZVNR/G electrodes would still require a conductive film, like gold used in piezoelectric nanogenerator or sensor [3], or ITO in solar cell [62]. Direct approaches for graphene characterization during interfacing with other materials is therefore crucial to advance its application as alternative TC and reduce the device cost and the use of non-abundant metals. We report the use of Raman spectroscopy from both sides of the interface as a simple and useful tool to study junctions of 2D and 3D nanomaterials. We demonstrate that cathodic electrodeposition on graphene offers a feasible *in situ* route to fabricate the ZVNR/G hybrid, and graphene-based hybrids in general, while

preserving its sp^2 structure. The negative bias applied during electrochemical processing seems to protect graphene from defect introduction, as it has been observed in electrochemical delamination from metallic foils [63]. Electrodeposition is also compatible with flexible polymer substrates, due to low temperatures required, and the resulting high crystallinity of ZVNRs eliminates the need of further thermal processing. Moreover, electrodeposition provides fast ZVNR growth rates of ~2μm/hr from a 5-10mM Zn(NO$_3$)$_2$ solution, according to our results and other report [31], which is another determining factor for its application, for example in DSSCs, where the optimum semiconducting layer thickness is ~25μm [64]. ZnO growth rates on graphene substrates by electrodeposition are much faster than by hydrothermal methods of 0.7μm/hr from 25mM Zn(NO$_3$)$_2$, which also requires additional reactants like hexamethylenetetramine [65]. ALD of ZnO has also shown to preserve the sp^2 lattice of graphene, however its rate of growth is as low as 0.03μm/hr [66]. Electrodeposition rates are also much higher than those reported with catalyst-free CVD/thermal evaporation of 0.1-0.6 μm/hr [29]. The only technique reported until now with similar growth rates is MOVPE, with 1-4 μm/hr [28, 61], however, it is performed in oxidative conditions like CVD, which are not compatible with graphene technology. **Therefore, electrodeposition stands out as one of the most promising methods for the *in situ* fabrication of ZVNR/G heterostructure in terms of the structure-property-processing material paradigm.**

3.4. Conclusions

A continuous carpet of single-crystalline ZVNRs is grown *in situ* on graphene by electrodeposition. The optimized current density for good alignment and crystallinity was found to be 0.4mA/cm^2. Lower current densities result in poor crystallinity, while higher values yielded a tubular morphology attributed to fast growth kinetics. The ZnO film grown at the optimized conditions is a continuous carpet of crystalline vertically aligned nanorods highly texturized in the [0001] direction with average diameters of 364 nm and growth rates of ~2μm/hr from a 10mM Zn(NO$_3$)$_2$ concentration. The lattice mismatch between graphene

and ZnO generates an out-of-plane strain that results in mosaicity and crystal distortions that could be attributed to misfit dislocations in the ZVNRs. The heterostructure is characterized from the two sides of the interface formed between the 2D graphene and the 3D ZVNRs array to monitor the stability of the sp^2 carbon lattice in graphene towards cathodic electrodeposition. The Raman shift spectra recorded from both sides of the junction demonstrate that the electrodeposition conditions prevent graphene oxidation and the sp^2 network remains intact. Yet, an increase of graphene's sheet resistance of 68-100% is observed, which is hypothesized to occur because of interfacial strain effects, mobility loss caused by ZVNRs acting as scattering centers for charge carriers, or doping due to electron transfer from the ZnO. The results demonstrate the advantages of cathodic electrodeposition for *in situ* growth of crystalline materials like ZnO on graphene, including relative fast deposition rates, low processing temperatures that would allow the use of polymeric flexible substrates, affordability, simplicity and more importantly, preservation of the sp^2 lattice of graphene. The ZnO/graphene heterostructures have potential as flexible platforms for sustainable photovoltaic applications, including the exploration of the nanotubular morphology to increase surface area of the photoanode.

3.5. References

1.   Baek, H.; Kwak, H.; Song, M. S.; Ha, G. E.; Park, J.; Tchoe, Y.; Hyun, J. K.; Park, H. Y.; Cheong, E.; Yi, G. C., ZnO nanotube waveguide arrays on graphene films for local optical excitation on biological cells. *Apl Materials* **2017,** *5* (4).

2.   Willander, M.; Khun, K.; Ibupoto, Z. H., ZnO Based Potentiometric and Amperometric Nanosensors. *Journal of Nanoscience and Nanotechnology* **2014,** *14* (9), 6497-6508.

3.   Li, X. D.; Chen, Y.; Kumar, A.; Mahmoud, A.; Nychka, J. A.; Chung, H. J., Sponge-Templated Macroporous Graphene Network for Piezoelectric ZnO Nanogenerator. *Acs Applied Materials & Interfaces* **2015,** *7* (37), 20753-20760.

4.   Law, M.; Greene, L. E.; Johnson, J. C.; Saykally, R.; Yang, P. D., Nanowire dye-sensitized solar cells. *Nature Materials* **2005,** *4* (6), 455-459.

5.   Lewis, N. S., Toward cost-effective solar energy use. *Science* **2007,** *315* (5813), 798-801.

6.   Mathew, S.; Yella, A.; Gao, P.; Humphry-Baker, R.; Curchod, B. F. E.; Ashari-Astani, N.; Tavernelli, I.; Rothlisberger, U.; Nazeeruddin, M. K.; Gratzel, M., Dye-sensitized solar cells with 13% efficiency achieved through the molecular engineering of porphyrin sensitizers. *Nature Chemistry* **2014,** *6* (3), 242-247.

7.   Li, T. L.; Lee, Y. L.; Teng, H., High-performance quantum dot-sensitized solar cells based on sensitization with CuInS2 quantum dots/CdS heterostructure. *Energy & Environmental Science* **2012,** *5* (1), 5315-5324.

8.   Chandrasekhar, P. S.; Komarala, V. K., Effect of graphene and Au@SiO2 core-shell nano-composite on photoelectrochemical performance of dye-sensitized solar cells based on N-doped titania nanotubes. *Rsc Advances* **2015,** *5* (103), 84423-84431.

9.   Kazim, S.; Nazeeruddin, M. K.; Graetzel, M.; Ahmad, S., Perovskite as Light Harvester: A Game Changer in Photovoltaics. *Angewandte Chemie-International Edition* **2014,** *53* (11), 2812-2824.

10.   Thakur, U. K.; Askar, A. M.; Kisslinger, R.; Wiltshire, B. D.; Kar, P.; Shankar, K., Halide perovskite solar cells using monocrystalline TiO2 nanorod arrays as electron transport layers: impact of nanorod morphology. *Nanotechnology* **2017,** *28* (27).

11.   Thavasi, V.; Lazarova, T.; Filipek, S.; Kolinski, M.; Querol, E.; Kumar, A.; Ramakrishna, S.; Padros, E.; Renugopalakrishnan, V., Study on the Feasibility of Bacteriorhodopsin as Bio-Photosensitizer in Excitonic Solar Cell: A First Report. *Journal of Nanoscience and Nanotechnology* **2009,** *9* (3), 1679-1687.

12.   Mershin, A.; Matsumoto, K.; Kaiser, L.; Yu, D.; Vaughn, M.; Nazeeruddin, M. K.; Bruce, B. D.; Graetzel, M.; Zhang, S., Self-assembled photosystem-I biophotovoltaics on nanostructured TiO2 and ZnO. *Scientific Reports* **2012,** *2*.

13.   Polgreen, L., Congo's Riches, Looted by Renegade Troops. *New York Times* 2008, p 14.

14.   Badding, M. A.; Fix, N. R.; Orandle, M. S.; Barger, M. W.; Dunnick, K. M.; Cummings, K. J.; Leonard, S. S., Pulmonary toxicity of indium-tin oxide production facility particles in rats. *Journal of Applied Toxicology* **2016,** *36* (4), 618-626.

15.   Cho, B.; Kim, H.; Yang, D.; Shrestha, N. K.; Sung, M. M., Highly conductive air-stable ZnO thin film formation under in situ UV illumination for an indium-free transparent electrode. *Rsc Advances* **2016,** *6* (73), 69027-69032.

16.   Ravichandran, K.; Begum, N. J.; Snega, S.; Sakthivel, B., Properties of Sprayed Aluminum-Doped Zinc Oxide FilmsA Review. *Materials and Manufacturing Processes* **2016,** *31* (11), 1411-1423.

17.   Song, W.; Kwon, S. Y.; Myung, S.; Jung, M. W.; Kim, S. J.; Min, B. K.; Kang, M.-A.; Kim, S. H.; Lim, J.; An, K.-S., High-mobility ambipolar ZnO-graphene hybrid thin film transistors. *Scientific Reports* **2014,** *4*.

18.   Roy-Mayhew, J. D.; Aksay, I. A., Graphene Materials and Their Use in Dye-Sensitized Solar Cells. *Chemical Reviews* **2014,** *114* (12), 6323-6348.

19.   Badhulika, S.; Terse-Thakoor, T.; Villarreal, C.; Mulchandani, A., Graphene hybrids: synthesis strategies and applications in sensors and sensitized solar cells. *Frontiers in Chemistry* **2015,** *3* (38), 19.

20.   Liu, Z. K.; You, P.; Liu, S. H.; Yan, F., Neutral-Color Semitransparent Organic Solar Cells with All-Graphene Electrodes. *Acs Nano* **2015,** *9* (12), 12026-12034.

21.   Sze, S.; Ng, K., *Physics of Semiconductor Devices*. 3rd ed.; John Wiley and Sons, Inc.: 2006; p 815.

22.   Georgakilas, V.; Otyepka, M.; Bourlinos, A. B.; Chandra, V.; Kim, N.; Kemp, K. C.; Hobza, P.; Zboril, R.; Kim, K. S., Functionalization of Graphene: Covalent and Non-Covalent Approaches, Derivatives and Applications. *Chemical Reviews* **2012,** *112* (11), 6156-6214.

23.   Ni, Z. H.; Wang, Y. Y.; Yu, T.; Shen, Z. X., Raman Spectroscopy and Imaging of Graphene. *Nano Research* **2008,** *1* (4), 273-291.

24.   Sun, Z. C.; Yang, C.; Liu, M.; Chen, C. S.; Xu, S. C.; Zhang, C.; Man, B. Y., Limited graphene oxidation on the synthesis of ZnO-graphene hybrid nanostructures by the Zn predeposition. *Applied Surface Science* **2014,** *315*, 368-371.

25.   Zhao, Y.; Li, W. B.; Pan, L. J.; Zhai, D. Y.; Wang, Y.; Li, L. L.; Cheng, W.; Yin, W.; Wang, X. R.; Xu, J. B.; Shi, Y., ZnO-nanorods/graphene heterostructure: a direct electron transfer glucose biosensor. *Scientific Reports* **2016,** *6*.

26.   Hambali, N. A.; Yahaya, H.; Mahmood, M. R.; Terasako, T.; Hashim, A. M., Synthesis of zinc oxide nanostructures on graphene/glass substrate by electrochemical deposition: effects of current density and temperature. *Nanoscale Research Letters* **2014,** *9*.

27.   Skompska, M.; Zarebska, K., Electrodeposition of ZnO Nanorod Arrays on Transparent Conducting Substrates-a Review. *Electrochimica Acta* **2014,** *127*, 467-488.

28.   Kim, Y.-J.; Lee, J.-H.; Yi, G.-C., Vertically aligned ZnO nanostructures grown on graphene layers. *Applied Physics Letters* **2009,** *95* (21).

29.   Ahmad, N. F.; Yasui, K.; Hashim, A. M., Seed/catalyst-free growth of zinc oxide on graphene by thermal evaporation: effects of substrate inclination angles and graphene thicknesses. *Nanoscale Research Letters* **2015,** *10*.

30.   Yin, Z.; Wu, S.; Zhou, X.; Huang, X.; Zhang, Q.; Boey, F.; Zhang, H., Electrochemical Deposition of ZnO Nanorods on Transparent Reduced Graphene Oxide Electrodes for Hybrid Solar Cells. *Small* **2010,** *6* (2), 307-312.

31.   Xu, C.; Lee, J. H.; Lee, J. C.; Kim, B. S.; Hwang, S. W.; Whang, D., Electrochemical growth of vertically aligned ZnO nanorod arrays on oxidized bi-layer graphene electrode. *Crystengcomm* **2011,** *13* (20), 6036-6039.

32.   **Banszerus, L.**; **Schmitz, M.**; **Engels, S.**; **Dauber, J.**; **Oellers, M.**; **Haupt, F.**; **Watanabe, K.**; **Taniguchi, T.**; **Beschoten, B.**; **Stampfer, C.**, Ultrahigh-mobility graphene devices from chemical vapor deposition on reusable copper. *Science Advances* **2015,** *1* (6), 1-6.

33.   Hambali, N. A.; Hashim, A. M., Synthesis of Zinc Oxide Nanostructures on Graphene/Glass Substrate via Electrochemical Deposition: Effects of Potassium Chloride and Hexamethylenetetramine as Supporting Reagents. *Nano-Micro Letters* **2015,** *7* (4), 317-324.

34.   Villarreal, C. C.; Pham, T.; Ramnani, P.; Mulchandani, A., Carbon allotropes as sensors for environmental monitoring. *Current Opinion in Electrochemistry* **2017,** *3* (1), 106-113.

35.   Malekpour, H.; Ramnani, P.; Srinivasan, S.; Balasubramanian, G.; Nika, D. L.; Mulchandani, A.; Lake, R.; Balandin, A. A., Thermal conductivity of graphene with defects induced by electron beam irradtiation. *Nanoscale* **2016,** *8* (30), 14608-14616.

36.   Ji, H. X.; Zhao, X.; Qiao, Z. H.; Jung, J.; Zhu, Y. W.; Lu, Y. L.; Zhang, L. L.; MacDonald, A. H.; Ruoff, R. S., Capacitance of carbon-based electrical double-layer capacitors. *Nature Communications* **2014,** *5*.

37.   Tay, S. E. R.; Goode, A. E.; Weker, J. N.; Cruickshank, A. A.; Heutz, S.; Porter, A. E.; Ryan, M. P.; Toney, M. F., Direct in situ observation of ZnO nucleation and growth via transmission X-ray microscopy. *Nanoscale* **2016,** *8* (4), 1849-1853.

38.   Liang, Z. W.; Cui, H.; Wang, K.; Yang, P. H.; Zhang, L.; Mai, W. J.; Wang, C. X.; Liu, P. Y., Morphology-controllable ZnO nanotubes and nanowires: synthesis, growth mechanism and hydrophobic property. *Crystengcomm* **2012,** *14* (5), 1723-1728.

39.   Nayeri, F. D.; Kolahdouz, M.; Asl-Soleimani, E.; Mohajerzadeh, S., Low temperature carving of ZnO nanorods into nanotubes for dye-sensitized solar cell application. *Journal of Alloys and Compounds* **2015,** *633*, 359-365.

40.   Hong, H. K.; Jo, J.; Hwang, D.; Lee, J.; Kim, N. Y.; Son, S.; Kirn, J. H.; Jin, M. J.; Jun, Y. C.; Erni, R.; Kwak, S. K.; Yoo, J. W.; Lee, Z., Atomic Scale Study on Growth and Heteroepitaxy of ZnO Monolayer on Graphene. *Nano Letters* **2017,** *17* (1), 120-127.

41.   Choi, W. M.; Shin, K. S.; Lee, H. S.; Choi, D.; Kim, K.; Shin, H. J.; Yoon, S. M.; Choi, J. Y.; Kim, S. W., Selective Growth of ZnO Nanorods on SiO2/Si Substrates Using a Graphene Buffer Layer. *Nano Research* **2011,** *4* (5), 440-447.

42.   Honda, M.; Okumura, R.; Ichikawa, Y., Direct growth of densely aligned ZnO nanorods on graphene. *Japanese Journal of Applied Physics* **2016,** *55* (8).

43.   Trampert, A.; Brandt, O.; Ploog, K. H., Chapter 7 Crystal Structure of Group III Nitrides. In *Semiconductors and Semimetals*, Pankove, J. I.; Moustakas, T. D., Eds. Elsevier: 1997; Vol. 50, pp 167-192.

44.   Ertekin, E.; Greaney, P. A.; Chrzan, D. C.; Sands, T. D., Equilibrium limits of coherency in strained nanowire heterostructures. *Journal of Applied Physics* **2005,** *97* (11).

45.   Wimbush, S. C.; Li, M. C.; Vickers, M. E.; Maiorov, B.; Feldmann, D. M.; Jia, Q. X.; MacManus-Driscoll, J. L., Interfacial Strain-Induced Oxygen Disorder as the Cause of Enhanced Critical Current Density in Superconducting Thin Films. *Advanced Functional Materials* **2009,** *19* (6), 835-841.

46.   Matsubara, T.; Sugimoto, K.; Okada, N.; Tadatomo, K., Atomic-scale investigation of structural defects in GaN layer on c-plane sapphire substrate during initial growth stage. *Japanese Journal of Applied Physics* **2016,** *55* (4).

47.   Faugier-Tovar, J.; Lazar, F.; Marichy, C.; Brylinski, C., Influence of the Lattice Mismatch on the Atomic Ordering of ZnO Grown by Atomic Layer Deposition onto Single Crystal Surfaces with Variable Mismatch (InP, GaAs, GaN, SiC). *Condensed Matter* **2017,** *2* (1).

48.   Dresselhaus, M. S.; Jorio, A.; Souza, A. G.; Saito, R., Defect characterization in graphene and carbon nanotubes using Raman spectroscopy. *Philosophical Transactions of the Royal Society a-Mathematical Physical and Engineering Sciences* **2010,** *368* (1932), 5355-5377.

49.   Alim, K. A.; Fonoberov, V. A.; Shamsa, M.; Balandin, A. A., Micro-Raman investigation of optical phonons in ZnO nanocrystals. *Journal of Applied Physics* **2005,** *97* (12).

50.   Ferrari, A. C., Raman spectroscopy of graphene and graphite: Disorder, electron-phonon coupling, doping and nonadiabatic effects. *Solid State Communications* **2007,** *143* (1-2), 47-57.

51.   Robertson, A. W.; Warner, J. H., Hexagonal Single Crystal Domains of Few-Layer Graphene on Copper Foils. *Nano Letters* **2011,** *11* (3), 1182-1189.

52.   Song, T., Graphene-Tapered ZnO Nanorods Array as a Flexible Antireflection Layer. *Journal of Nanomaterials* **2015**.

53.   Gokus, T.; Nair, R. R.; Bonetti, A.; Bohmler, M.; Lombardo, A.; Novoselov, K. S.; Geim, A. K.; Ferrari, A. C.; Hartschuh, A., Making Graphene Luminescent by Oxygen Plasma Treatment. *Acs Nano* **2009,** *3* (12), 3963-3968.

54.   Jia, S.; Sun, H. D.; Du, J. H.; Zhang, Z. K.; Zhang, D. D.; Ma, L. P.; Chen, J. S.; Ma, D. G.; Cheng, H. M.; Ren, W. C., Graphene oxide/graphene vertical heterostructure electrodes for highly efficient and flexible organic light emitting diodes. *Nanoscale* **2016,** *8* (20), 10714-10723.

55.   Adam, S.; Hwang, E. H.; Galitski, V. M.; Das Sarma, S., A self-consistent theory for graphene transport. *Proceedings of the National Academy of Sciences of the United States of America* **2007,** *104* (47), 18392-18397.

56.   Pinto, H.; Markevich, A., Electronic and electrochemical doping of graphene by surface adsorbates. *Beilstein Journal of Nanotechnology* **2014,** *5*, 1842-1848.

57.   Geng, W.; Zhao, X. F.; Liu, H. X.; Yao, X. J., Influence of Interface Structure on the Properties of ZnO/Graphene Composites: A Theoretical Study by Density Functional Theory Calculations. *Journal of Physical Chemistry C* **2013,** *117* (20), 10536-10544.

58.   Nguyen, V. H.; Hoang, T. X.; Dollfus, P.; Charlier, J. C., Transport properties through graphene grain boundaries: strain effects versus lattice symmetry. *Nanoscale* **2016,** *8* (22), 11658-11673.

59.   Yang, H.; Li, L.; Li, J. L.; Mo, Z. J., Selective growth of hierarchical ZnO nanorod arrays on the graphene nanosheets. *Journal of Physics D-Applied Physics* **2016,** *49* (1).

60.   Kim, Y. J.; Kim, S. S.; Park, J. B.; Sohn, B. H.; Yi, G. C., Controlled growth of inorganic nanorod arrays using graphene nanodot seed layers. *Nanotechnology* **2014,** *25* (13).

61.   Park, J. B.; Oh, H.; Park, J.; Kim, N. J.; Yoon, H.; Yi, G. C., Scalable ZnO nanotube arrays grown on CVD-graphene films. *Apl Materials* **2016,** *4* (10).

62.   Kilic, B.; Turkdogan, S., Fabrication of dye-sensitized solar cells using graphene sandwiched 3D-ZnO nanostructures based photoanode and Pt-free pyrite counter electrode. *Materials Letters* **2017,** *193*, 195-198.

63.   Gao, L. B.; Ren, W. C.; Xu, H. L.; Jin, L.; Wang, Z. X.; Ma, T.; Ma, L. P.; Zhang, Z. Y.; Fu, Q.; Peng, L. M.; Bao, X. H.; Cheng, H. M., Repeated growth and bubbling transfer of graphene with millimetre-size single-crystal grains using platinum. *Nature Communications* **2012,** *3*.

64.   Lin, C.-M.; Tsia, C.-Y.; Chang, W.-C. In *Dye-sensitized solar cells based on electrodeposited zinc oxide films - IEEE Conference Publication*, Nanoelectronics Conference (INEC), 2011 IEEE 4th International, Tao-Yuan, Taiwan, IEEE: Tao-Yuan, Taiwan, 2011.

65.   Choi, D.; Choi, M. Y.; Choi, W. M.; Shin, H. J.; Park, H. K.; Seo, J. S.; Park, J.; Yoon, S. M.; Chae, S. J.; Lee, Y. H.; Kim, S. W.; Choi, J. Y.; Lee, S. Y.; Kim, J. M., Fully Rollable Transparent Nanogenerators Based on Graphene Electrodes. *Advanced Materials* **2010,** *22* (19), 2187-+.

66.   Jiao, K. J.; Wu, X. F.; Duan, C. Y.; Zhang, D. W.; Wang, Y.; Chen, Y. F., Novel ALD-assisted growth of ZnO nanorods on graphene and its Cu2ZnSn(SxSe1-x)(4) solar cell application. *Physical Chemistry Chemical Physics* **2015,** *17* (6), 4757-4762.

Chapter III:

Electrodeposition of ZnO Nanorods on Graphene: Tuning the Topography for Application as Tin Oxide-Free Photoanode

Abstract

This work focuses on the growth of vertically-aligned zinc oxide nanorods on a graphene substrate by electrodeposition for photoanode application. This *in situ* growth technique has potential for fabrication of a wide variety of graphene heterostructures. Large area graphene was grown by chemical vapor deposition, stacked up to four atomic layers, and then transferred to glass to serve as a tin oxide-free transparent conductor (TC). ZVNRs were electrodeposited on the graphene-coated glass and the topography was controlled by changing the electrodeposition parameters of time, temperature, stirring, and seeding layer. The scanning electron microscopy of the ZVNR/G topography allowed an understanding of the mechanisms controlling the cathodic electrodeposition of nanocrystals on graphene. The effect of the ZVNRs' topography on the electron generation and transport was studied for photoanode application. The charge transfer resistance and kinetics of the materials as photoanodes were measured with the techniques of linear sweep voltammetry, open circuit voltage decay and electrochemical impedance spectroscopy. The optimization of ZnO growth resulted in an increase of the surface-to-volume ratio of the electrode from 10 to 250 um^{-1}. As a result, a 60-fold increase of electron lifetime and 10-fold increase in power output was achieved, for final short circuit current (J_{sc}) of 0.5mA/cm^2 and open circuit potential (V_{oc}) of 600mV.

4.1. Introduction

A photoelectrochemical cell (PEC) is a device that harvests sunlight to convert it into other forms of energy such as chemical or electrical. A PEC is based on a photoanode connected to a counter electrode via an electrolyte. The photoanode absorbs the photons and drives oxidation reactions of a mediator in the electrolyte, which are regenerated in the counterelectrode. Nanostructured wide-bandgap semiconductors, like TiO_2 or ZnO, spread over a TC are attractive as photoanodes due to their low cost and availability. The limited solar spectrum range that ZnO or TiO_2 absorbs in the UV is expanded by sensitizing the photoanodes with photoactive materials that absorb in the visible range of the sun spectrum, such as dyes [1]. A large portion of the photoanode cost corresponds to the choice of TC, typically doped tin oxide. Tin oxides are fragile materials derived from non-abundant sources, like cassiterite, which classifies as conflict mineral and can adversely affect water quality and human health [2-4]. Graphene is a sustainable alternative to tin oxides, as it can be obtained from a variety of organic sources, including waste byproducts. Pristine CVD-graphene with large domain size stands out as the most promising graphene variant for TC application, not only due to its superior optoelectronic properties, but because large area films can be produced in industrial scale [5].

ZnO and TiO_2 are the two most common wide-bandgap semiconductors for photoanodes with very similar bandgaps; however ZnO has an electron mobility that is two to three orders of magnitude larger[6]. ZnO is also more reactive and can be synthesized into crystalline form under mild conditions with a variety of shapes, which makes it more compatible for *in situ* growth on graphene, considering the high oxidation susceptibility of the latter. The vertically aligned ZnO nanorods (ZVNRs) offer a large surface area for light scattering and absorption. Their short radial distance promotes rapid transport of minority charge carriers towards the junction for exciton separation. ZVNRs also have lower electron transfer resistance through the semiconductor in comparison to nanoparticles assemblies where electrons must cross several interfaces with high probability of recombination [7-9]. **Therefore, understanding how the parameters for**

ZVNR *in situ* growth on graphene affect its topography and photoanode performance is fundamental for the future development of low-cost sustainable PECs, as illustrated in **Figure 4.1.**
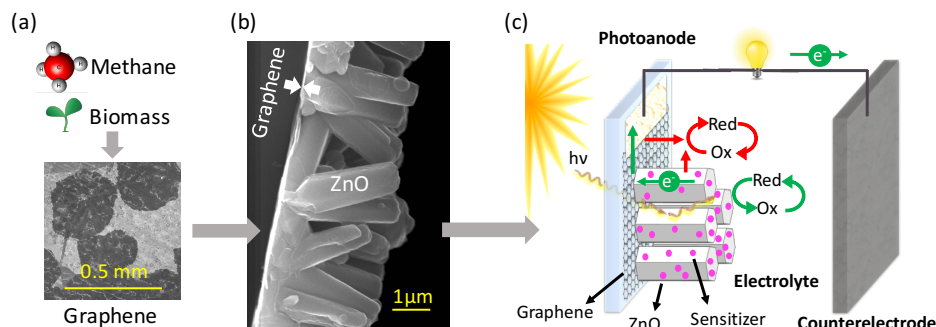
Figure 4.1.   Sustainable fabrication of tin-oxide free Photoanode: (a) Synthesis of high-quality graphene, a carbon-based TC produced from abundant renewable resources. (b) Electrodeposition of ZnO nanostructures on graphene to make a hybrid Photoanode. (c) Use of ZVNR/G hybrid as a photoanode, electron transfer processes occurring: arrows in green indicate power generating processes, arrows in red indicate power loss processes

Electrodeposition of nanostructured thin films has been gaining attention lately due to the high-end quality of the film, the great process and its advantages over other techniques like doctor-blade and chemical vapor deposition control [10]. Crystalline nanostructures can be obtained with electrodeposition at temperatures below 100˚C without further need for thermal treatments, which is a critical requirement for the development of flexible devices on polymeric substrates. This technique is an *in situ* deposition method, which results in reduced interfacial resistance. It is also facile and low-cost, as no expensive facilities or high energy processes are required. A systemic study of the electrodeposition of ZVNRs using NO_3^- as a precursor on tin oxide substrate was first reported in 2012 [11]. The reaction leading to oxide formation is the electrogeneration of a base (**Equation 4.1**) followed by dehydration (**Equation 4.2**):

$NO_3^- + H_2O + 2e^- \rightarrow NO_2^- + 2OH^-$ **Equation 4.1**

$Zn^{2+} + 2OH^- \xrightarrow{temp} ZnO + H_2O$ **Equation 4.2**
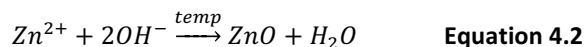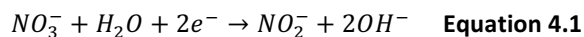
In a photoanode, the power conversion efficiency is strongly dependent on the surface area of the semiconductor, as this determines the junction area at which the photoelectrochemical reactions take place. For an array of ZVNRs, the surface area can be increased by reducing the diameter of the rods and

increasing their length. Several approaches are used to reduce the diameter of ZVNRs, being the use of seed layer, also called buffer layer, one of the most effective. This seed layer provides a dense source of nucleation centers for the growth of the ZVNRs [12].

Graphene variables like reduced graphene oxide [13] oxidized CVD-graphene [14] and pristine CVD-graphene [15] have been studied as conductive substrates for the fabrication of the ZVNR/graphene heterostructure (ZVNR/G). The mild growth conditions prevent graphene damage by oxidation. A negative bias applied seems to protect graphene from defect introduction, as it has been observed in electrochemical delamination from metallic foils [16]. We have demonstrated that cathodic electrodeposition on graphene offers a feasible *in situ* route to fabricate the ZVNR/G hybrid, while preserving the sp^2 structure of graphene [17]. The ZVNR grown on pristine CVD-graphene by electrodeposition has not been explored yet for tin oxide-free photoanodes.

In this work, we explore the effects of electrodeposition parameters on the ZVNR morphology and the performance of the hybrid as a photoanode in a DSC. The electrodeposition parameters investigated were temperature, time, stirring and the use of a seed layer. The photo-electron generation and transport in the ZVNR/G was studied via open circuit voltage decay (OCVD), electrochemical impedance spectroscopy (EIS), and linear sweep voltammetry (LSV). This study aims to explore the fundamentals of crystal growth in graphene as a sustainable conductive substrate, and elucidate the predominant mechanisms of power generation and loss of the heterostructure in solar energy harvesting application.

4.2. Experimental Procedures

4.2.1.   Graphene TC layer

A continuous graphene film was grown on Cu foil using ambient-pressure CVD, with diluted methane as carbon source ($\approx$90ppm) for one hour, following the method we reported recently to yield domain size up to 300μm [17, 18]. The graphene was spin-coated on one side with PMMA. The copper was etched in 0.3M $FeCl_3$ and cleaned with DI water. The floating graphene/PMMA film was stacked onto a second graphene/Cu film. The etch and stacking was repeated until 4-layered graphene (4LG) was obtained. The 4LG was then transferred onto a clean glass substrate, with the graphene in contact with the glass. The PMMA was dissolved in acetone, the graphene annealed in Ar/H_2 and 10/120nm Cr/Au contacts were e-beam evaporated.

4.2.2.   Electrodeposition of ZVNR on graphene

The ZVNR electrodeposition on graphene was performed using a CHI 660C electrochemical station in a three-electrode configuration, with graphene-on-glass as the working electrode, platinum mesh as the counter electrode, and Ag/AgCl$_{sat'd}$ as the reference electrode. PMMA was used as dielectric coating on the Cr/Au contact. For the ZVNR growth, a cathodic potential was applied to the graphene in 10mM $Zn(NO_3)_2$ aqueous solution to maintain a current density of 0.4 mA/cm^2, which had been optimized in our previous report to obtain well-aligned crystalline ZVNRs on graphene [17]. We studied the effect of three growth variables: temperature, time and stirring. The temperature studied varied between 70 and 80°C, the time was varied from 0.5 to 2 hr, and stirring and non-stirring conditions were compared. The $Zn(NO_3)_2$ solution was refreshed every 10 minutes for all experiments.

4.2.3.   Pre-deposition of seed layer

To pre-deposit a seed layer, a $Zn(OH)_x$ compact film was electrodeposited at -1.2 V from 50mM $Zn(NO_3)_2$ aqueous solution at room temperature, until a charge density of 30 mC/cm^2 was obtained. The film was converted into ZnO by annealing at 200˚C for 1hr [19, 20]. Other methods for seed layer deposition that were explored produced larger diameter ZVNRs are detailed in **Table 4.2**.

4.2.4.   Photoelectron transport characterization

The electron transport measurements were performed using a dye-sensitized solar cell (DSC) configuration. The photo-anode was sensitized through a 12-hour immersion in a 0.3 mM ethanoic solution of N3 dye (cis-Bis(isothiocyanato) bis(2,2'-bipyridyl-4,4'-dicarboxylato) ruthenium(II)) (Sigma-Aldrich). The counter-electrode was prepared by e-beam evaporation of a 40 nm/40 nm Ti/Pt film on a clean glass substrate. The photoanode and counter-electrode were clipped together to assemble the DSC, using a polydimethysiloxane spacer. The cell was filled with an electrolyte of acetonitrile and ethylene carbonate in 2:1 volume ratio, 0.1 M LiI, 0.03 M I_2, and 5%m/v $LiClO_4$. The DSCs were tested under a xenon lamp (USHIO UXL-75XE) with a power density of 100 mW/cm^2, calibrated with a Newport Power Meter 1918-R. Electrochemical characterization of the devices was performed with the CHI 660C in a two-electrode configuration.

The LSV was performed from 0.2 to -0.8V. The OCVD was measured by monitoring the open circuit voltage (V_{OC}) of the DSC after switching from illuminated to dark operation. Electron lifetime τ_n was calculated from the OCVD according to **Equation 4.3** [21]:

$$\tau_n = -\frac{k_B T}{n}\left(\frac{dV_{OC}}{dt}\right)^{-1} \qquad \textbf{Equation 4.3}$$

The EIS spectra was recorded under illumination in the frequency range between 0.1 Hz and 100 kHz, setting the bias voltage at the V_{OC} of the device and the amplitude at 10 mV. EIS of the photo-electrode was interpreted according to the most widely accepted model (**Figure 4.2**). The equivalent circuit of a DSC is

composed of the electron diffusion through ZnO (R_d) coupled to electron recombination reactions with the electrolyte (R_k) in a transmission line model, in series to the charge transfer resistance at the ZnO/G interface ($R_{ZnO/G}$) [22, 23].
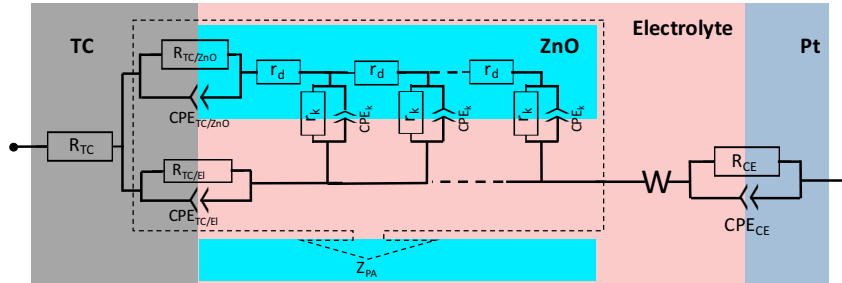
Figure 4.2.   Equivalent Circuit of the ZVNR/G DSC

4.3. Results

Table 4.1 details the electrodeposition parameters of stirring, seed layer, temperature (T) and time (t) studied for each sample and the morphology parameters of ZVNR density (ρ_{NR}) and diameter ($\varnothing_{NR}$) obtained from the image analysis of SEM micrographs.

Table 4.1.   ZVNRs electrodeposition parameters, density (ρ_{NR}) and diameter ($\varnothing_{NR}$)

	Stir	Seed layer	T (°C)	t (hr)	ρ_{NR} (cm^{-2})	$\varnothing_{NR}$ (nm)
1	✓	✕	70	0.5	1.8×10^8	475
2	✓	✕	75	0.5	3.4×10^8	364
3	✓	✕	80	0.5	3.5×10^8	360
4	✓	✕	80-75	2	1.9×10^8	790
5	✕	✕	80-75	2	5.5×10^8	487
6	✕	✓	80-75	2	4.3×10^9	134

4.3.1.   Effect of temperature and time

The electrodeposition bath temperature ranging from 70 to 80°C affects the topography of the ZVNRs, as shown in **Figure 4.3(a-c`)**. At 70˚C a sparse layer of randomly oriented ZVNR forms, while at 75˚C increased coverage and alignment is obtained, and the temperature at 80˚C causes even greater compactness and uniformity. The incomplete graphene coverage at 70˚C indicates that exclusion zones are

formed due to concentration depletion that hinder further nucleation near existing growing nuclei [24]. As higher temperatures are applied, mass transfer is more efficient, leading to complete coverage of the graphene surface. A higher nucleation density causes the ZVNR average diameter to reduce from 475nm at 70°C, to 364nm at 75°C and 360nm at 80°C. At the same time, the NR density increases from 1.8 /um^2 for 70°C, to 3.4/um^2 for 75°C and 3.5/um^2 for 80°C. Above 80°C, the ZnO crystal growth rate in the lateral directions is faster, and the VNRs' walls eventually merge into grain boundaries to form a continuous ZnO layer rather than a ZVNRs carpet.
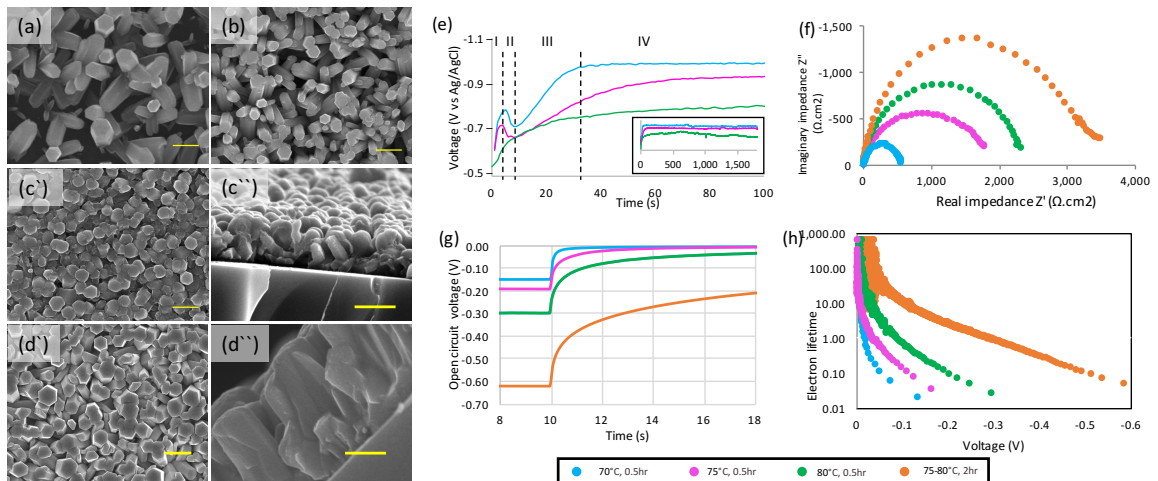
Figure 4.3.   SEM micrographs of ZnO NRs on graphene grown by electrodeposition at (a) 70˚C, (b) 75˚C and (c) 80˚C for 30min, and (d) at 75-80˚C for 2hr, scale bar 1μm. (e) Applied potential as a function of time for ZVNR electrodeposition on graphene at constant current density 0.4mA/cm^2. (f) EIS Nyquist plot, (g) V_{OC} decay and (h) calculated electron lifetime for DSCs fabricated with the different photoanodes.

Figure 4.3(e) shows the potential-time (V-t) curves for the electrodeposition of ZVNRs at the different temperatures . The potential range for the deposition is within the zone for ZnO formation in the Pourbaix diagram for the Zn/H_2O system [25]. The curve corresponds to a mass transfer-controlled process showing four distinct regions. In stage I, a sudden increase of the potential is related to the double charge layer formation. Stage II is a short period of potential reduction, during which independent nuclei appear and grow on the surface of the graphene. This growth continues until the formation of exclusion zones that virtually arrest further nucleation and a minimum potential is reached. Stage III is another region of

potential increase which is more extended than stage I. During stage III, the two opposing processes of independent nuclei growth and their overlap take place. This leads to electrode relative passivation due to gradual coverage of the conductive graphene, raising the overpotential required to maintain constant mass deposition. Finally, a plateau is reached in stage IV, in which the available graphene surface is either coated with ZnO or is an exclusion zone. During stage IV, steady growth occurs because a constant ionic concentration is maintained in the bulk of the electrolyte by refreshing the solution. Faster deposition rates in the [0001] direction lead to ZVNR formation [26, 27]. As a general trend, less overpotential is required at higher temperatures to maintain the galvanostatic conditions, due to the additional energy provided by the heat. The V-t curve obtained at 80°C lacks region II indicates that nucleation and overlapping occur almost instantaneously, and growth is not inhibited by exclusion zones at this temperature.

The heterostructure of ZVNR/G was used as the photoanode in a DSC. The EIS of the devices grown at the different temperatures are described by the Nyquist plots in **Figure 4.3(f)**, showing that as the graphene´s surface becomes more densely coated, a larger recombination resistance (R_k) results, due to blocking of the graphene. The transient photovoltage measurements in **Figure 4.3(g)** show that as the ZVNR film becomes more compacted, the cells produce a higher photovoltage under illumination. The heterostructure grown at 70°C yields a V_{oc} of 150mV, at 75°C it yields 190mV, and at 80°C it yields 300mV. A slower V_{oc} decay indicates that the electron lifetime τ_n is longer for the more compacted ZVNR films, as shown in **Figure 4.3(h)**. A more compacted film blocks the contact of the electrolyte with the graphene, increasing the recombination resistance and slowing down the photo-electron loss kinetics, as it has been observed in ZVNR/FTO photoanodes [28].

The desirable ZVNR morphology would be compacted at the bottom to prevent recombination losses from exposed graphene, but with gaps between the ZVNRs at the top to provide higher interfacial area at the junction of the device. Therefore, for the remainder of the growth experiments, we used 80°C during the first 10min of growth and then cooled down the solution to 75°C until the end of the ZVNR growth.

Extending the time of electrodeposition from 0.5hr to 2hr results in an increase of ZVNR dimensions, as reported previously on FTO [29]. The diameter increases from 360nm to 790nm, and the length increases from 0.9μm to 3.1μm, as observed in the SEM micrographs in **Figures 4.3(c'') and (d'')**. The lateral growth of the ZVNR occurs at slower rate than the longitudinal, because of the higher energy configuration of the 0001 planes. However, the slower growth in lateral directions still leads to the broadening of the ZVNR diameter at extended time, resulting in the merging of the ZVNR into a mostly continuous film of ZnO. **Figures 4.3(e-h)** show how the photoanode recombination resistance, photovoltage and electron lifetime increases because of the morphology, which is ascribed to the blocking of the graphene from the electrolyte, which prevented power loss events. The DSC V_{oc} doubles when the ZVNR were grown for 2hr instead of 30min.

Even though the higher temperature and longer growth time increase the photovoltage of the electrode, the photocurrent remains low, as illustrated in **Figure 4.4**.
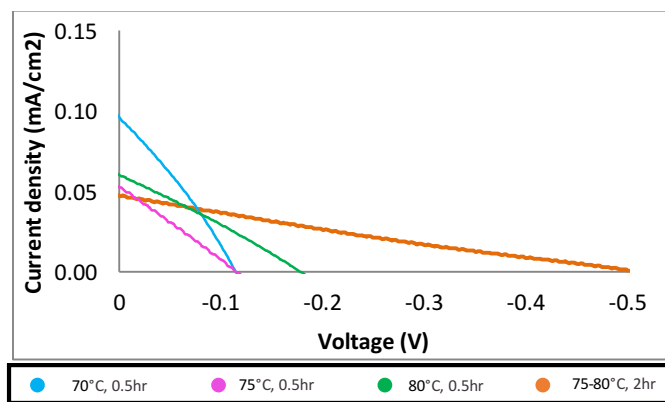
Figure 4.4. Linear sweep voltammetry for DSC fabricated with ZVNR/G photoelectrodes

4.3.1. Effect of stirring

The stirring conditions during electrodeposition were varied to modify the mass transfer during ZVNR growth. When the ZVNRs grow in stirred conditions, straight rods grow as shown in **Figure 4.5(a)**, while in unstirred conditions conical rods develop, shown in **Figure 4.5(b).** The length of the ZVNRs increases to 4.7μm in unstirred conditions, compared to 3.1 μm for stirred conditions, while the diameter is reduced from 790μm to 487μm, which is expected to maintain constant mass deposition, i.e. constant current density. The conical shape and the increased length are a result of increased Zn^+ concentration gradient. Anisotropic growth occurs mostly along the *c*-direction of the crystal in unstirred conditions because Zn^+ diffusion is significantly slower than OH^- generation. As the ratio of OH^- to Zn^+ increases in the immediate vicinity of the electrode, most Zn^+ ions are consumed at the tip of the rods, limiting lateral growth [11, 30]. In unstirred conditions, a 3-fold increase in ZVNR density is observed to yield $5x10^8$ ZVNRs/cm^2, compared to $1.9x10^8$ ZVNRs/cm^2 in stirred conditions.
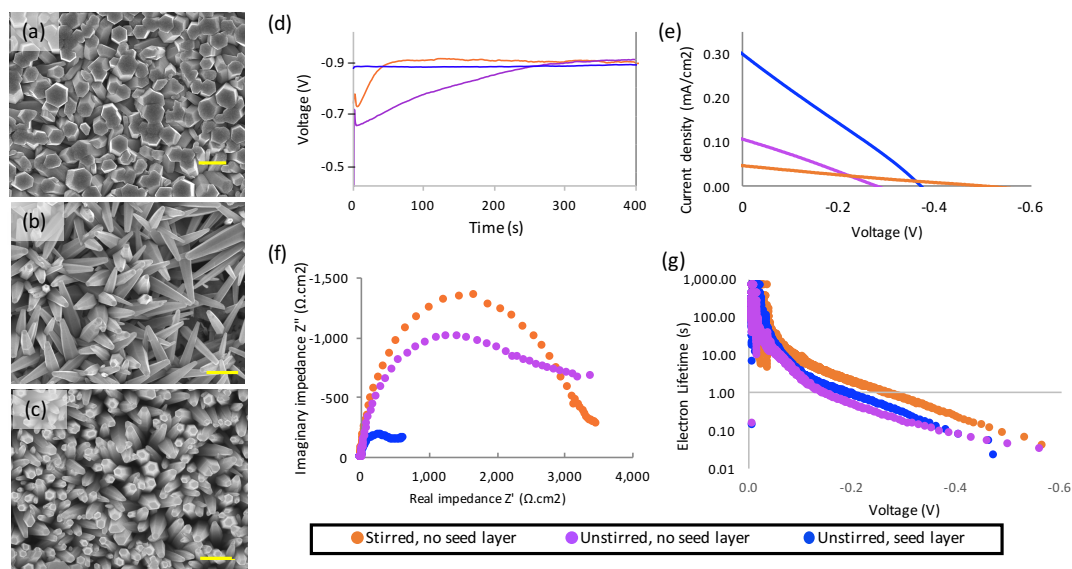
Figure 4.5. SEM images of ZVNR electrodeposited on graphene (a) non-stirred, (b) stirred and (c) with seed layer, scale bar 500 nm. (d) Applied potential as a function of time for ZVNR electrodeposition on graphene at constant current density 0.4mA/cm^2. (e) Linear sweep voltammetry, (f) EIS Nyquist plot and (g) electron lifetime for DSCs fabricated with the different photoanodes

The V-t curves for the growth of the ZVNRs in unstirred and stirred conditions are compared in **Figure 4.5(d).** Same growth mechanisms seems to occur at both conditions, with 4 distinct stages, as analyzed previously. However, in unstirred conditions, nuclei formation in stage II occurs at faster rates. The reduced diffusion of ions along the graphene surface in unstirred conditions probably accelerates electrocrystallization, leading to faster achievement the minimum potential, as exclusion zones form much faster. At the same time, nuclei growth in stage III occurs at much slower rates in unstirred compared to stirred conditions, and surface saturation takes 6 times longer. The slower mass transfer at the surface of the graphene when unstirred leads to slower deposition rate [31]. The potential plateau of stage IV has a similar value of ~-0.9V for unstirred and stirred conditions, as the current density and temperature are identical. Therefore, the stirring conditions do not modify the thermodynamics of the system, but only the mass transfer kinetics.
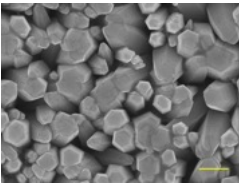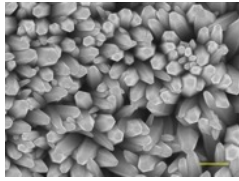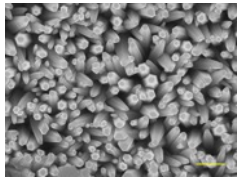
The conical shape and higher density of the ZNVRs grown in unstirred conditions leads to a photo-current twice as large as obtained for ZVNR grown under stirred conditions, as observed in **Figure 4.5(e)**. Better light scattering and larger surface area promotes occurrence of photochemical reactions. However, the lower recombination resistance reduces the electron lifetime, which in turn lowers the photovoltage (**Figures 4.5(f-g)**). This result indicates that the increased space between ZVNRs causes electrolyte infiltration and short circuiting between the redox mediator and the electrocatalytic graphene.

4.3.2.   Effect of seed layer

The high mobility of pristine CVD-graphene with large domains is one of its most desirable features for TC application. However, the surface of CVD-graphene is very smooth, providing lower nucleation rates and larger ZVNR diameter than those obtained in FTO [29], reduced graphene oxide (rGO) [13] and oxidized CVD-graphene [14]. We deposited a seed layer to increase ZVNR nucleation density without reducing optoelectronic performance of the pristine CVD-graphene. Three methods were compared for depositing the seed layer: (i) spincoating of ZnO NPs [32, 33], (ii) spincoating of zinc acetate [34] and (iii) electrodeposition

of ZnOH$_x$ [19], all followed by thermal treatment. **Table 4.2** shows the SEM, ZVNR diameter and methods (i), (ii) and (iii) result in ZVNRs diameters of 330, 274, and 135nm respectively, compared to the 487nm obtained without seed layer. Electrodeposition of seed layer is the method that yields the smaller ZVNR diameter, with one order of magnitude increase in density, as summarized in **Table 4.1** and consistent with results on FTO [12].

Table 4.2.   Methods for pre-deposition of seed layer and results.

Method	ZVNR diameter (nm)	SEM micrograph
(i) **Spin-coating ZnO NPs**: The NPs were prepared by forced-hydrolysis from the reaction of Zinc acetate with sodium hydroxide in 200proof ethanol [32]. This NPs suspension was spin-coated at 2000 rpm for 60s followed by annealing at 100˚C immediately and heated to 250˚C, followed by 5min annealing [33]. The spin coating and thermal annealing were repeated twice.	330 ± 140	
(ii) **Spin-coating Zinc Acetate solution:** A solution of 5mM zinc acetate was heated for 15min at 90˚C. The solution was spin-coated at 2000 rpm for 60s followed by annealing at 100˚C immediately and heated to 250˚C, followed by 5min annealing [34]. The spin coating and thermal annealing were repeated twice.	274 ± 121	
(iii) **Electrodeposition of Zn(OH)x:** A Zn(OH)x compact film was electrodeposited at -1.2 V vs Ag/AgCl from 50mM Zn(NO3)2 aqueous solution at room temperature followed by annealing at 200˚C [19].	132 ± 51	

*Scale bar 500nm

   Reducing the ZVNR diameter with the electrodeposited seed layer results in better light scattering, with ten-fold increase in transmittance at 550nm, as shown in **Figure 4.6.** Therefore, we focused on the electrodeposition as the method for depositing the seed layer.
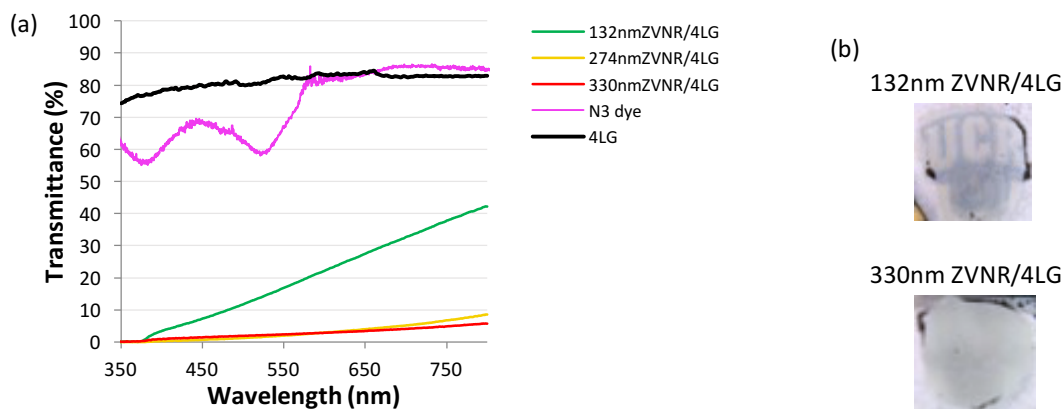
Figure 4.6. **(a) Transmittance of 4-layer graphene, N3 dye and ZVNR/G hybrid with different ZVNR diameter. (b) Photographs illustrating the transmittance of ZVNR/G films of different ZVNR diameter**

The presence of the seed layer on the graphene, modified the V-t curve of ZVNR growth as shown in **Figure 4.5(d)**. The V-t curve does not show the stages I , II and III previously observed , but starts directly at the plateau potential of ∼-0.9V. This indicates that the ZVNR electrodeposition on seed layer starts directly with growth, skipping the process of nucleation. The plateu potential with and without seed layer is the same due to identical thermodynamic conditions, as observed when comparing stirred and unstirred conditions.

The larger junction area of smaller dimeter-ZVNRs (**Figure 4.5(c)**) causes an overall three-fold increase in photocurrent generation and reduces the recombination resistance (**Figure 4.5(e-f)**). The photovoltage and electron lifetime remained high due to blocking of faster reactions at the graphene with the compact bottom layer of ZnO (**Figure 4.5(g)**). The combination of higher photocurrent and open circuit voltage results in increased maximum power generation from $8\mu W/cm^2$ without seed layer to $63\mu W/cm^2$ with seed layer.

The process of seed layer electrodeposition for ZVNR growth is detailed in **Figure 4.7(a).** At room temperature, the electrodeposition of a compact amorphous $Zn(OH)_x$ layer takes place. Then, the $Zn(OH)_x$ is decomposed into ZnO, a phase transition that occurs between 119 to 153˚C[19, 20], so, we performed the

thermal treatment at 200°C. The result is a compact film of ZnO NPs that control ZVNR growth and prevent shunt circuit contact with the TC.
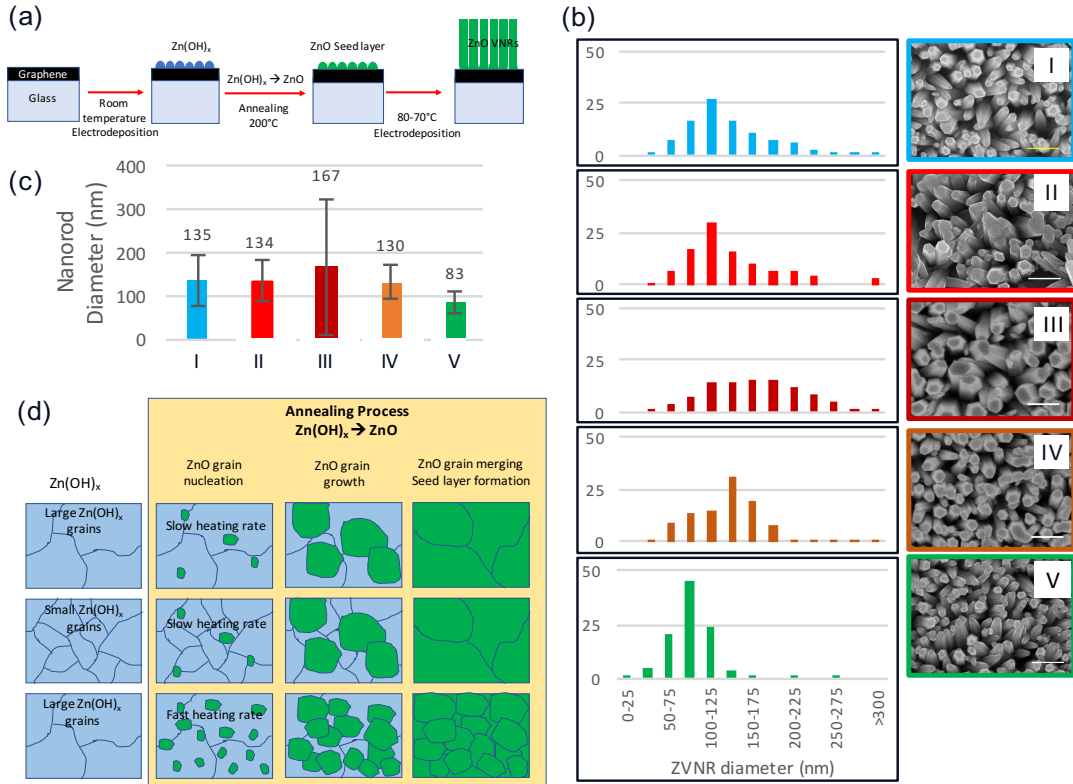
Figure 4.7.   a) Process of electrodeposition of seed layer and ZVNRs growth. b) Effect of seed layer deposition on the ZVNR diameter distribution and SEM imaging. Seed layer deposition variables I) control: 50mM $Zn(NO_3)_2$, stirred, -1.2V, 30mC/cm^2, slow heating, II) 200mM $Zn(NO_3)_2$, III) -1.3V, D) 25mC/cm^2, IV) fast heating c) Average ZVNR diameter obtained for each variable d) Mechanism of seed layer formation that controls the diameter of the ZVNR.

The seed layer deposition was optimized to further reduce the ZVNRs diameter, as detailed in **Figure 4.7(b-c)**. The initial conditions for the seed layer electrodeposition were 50mM $Zn(NO_3)_2$, -1.2V, to attain 30mC/cm^2 and thermal treatment heating rate of 5°C/min, which yield 134 nm diameter ZVNRs (sample I). The increase of seed layer nucleation rate was attempted, by increasing the concentration of $Zn(NO_3)_2$ to 200mM (sample II) and the potential to -1.3V (sample III), but these did not reduce of the ZVNR diameters either. The total charge was also reduced to 25mC/cm^2 (sample IV) to limit $Zn(OH)_x$ nuclei growth, but no reduction of the ZVNR diameter was observed either. As the variation of $Zn(OH)_2$ electrodeposition

conditions was not effective in reducing the ZVNR diameter, we opted for varying the thermal treatment instead, and thus control the phase transition from $Zn(OH)_2$ to ZnO (sample V). The heating rate of the material was accelerated by placing the sample directly in an oven at 200˚C. The resulting faster nucleation of ZnO from $Zn(OH)_2$ was effective in reducing the diameter to 83nm. Therefore, we present the mechanism for seed layer formation and illustrate it in **Figure 4.7(d)**. The deposition of $Zn(OH)_2$ does not determine the grain size for the seed layer, as it is an amorphous and unstable film [19]. Instead, it is the phase transition, essentially the ZnO nucleation stage from $Zn(OH)_x$, that determines the size of the seed layer grains, and therefore, controls the ZVNR diameter.

4.4. Conclusions

Pristine CVD-graphene with large domains is an attractive option as a TC due to its excellent optoelectronic properties. However, the preparation of graphene heterostructures to fabricate PEC poses challenges that need to be addressed to make this technology feasible. The smooth non-reactive surface of CVD-graphene delays nucleation, making it difficult to *in situ* grow very small nanocrystals like ZVNRs. Having very small nanocrystals is desirable because of their large junction area with the hole acceptor, that ultimately determines the photocurrent generation. At the same time the high catalytic activity of carbon results in electron recombination and power loss when it meets the electrolyte or other hole acceptor material.

Electrodeposition is a promising *in situ* method for growth of crystalline materials on graphene. We have studied the experimental correlations between the ZVNR electrodeposition parameters and the corresponding performances of the heterostructure as a photo-electrode, and summarized them in **Figure 4.8**. The ZVNR film can be made compacted and dense by increasing temperature (2-3) and time (4), to evenly cover the graphene surface and block recombination losses with the electrolyte. The blocking of graphene improved charge collection of the photoanode, with a longer electron lifetime, larger photovoltage and higher recombination resistance. However, the reduction of surface area when the film becomes more compact limits the photocurrent generated because of hindered light scattering. Non-stirred conditions (5) promoted formation of longer conical rods and the use of a seed layer (6) reduced the ZVNR diameter. These two variables together resulted in a greater surface to volume ratio of ZVNR, for improved light scattering and higher photocurrent generation, while retaining high photovoltage, for a total ten-fold improvement in power conversion. We explored the mechanism of seed layer electrodeposition to further reduce the ZVNR diameter. We found that the final diameter of the ZVNR is controlled by the seed layer process, and depends on the phase transition from $Zn(OH)_x$ to ZnO during thermal treatment, rather than on the electrodeposition parameters.
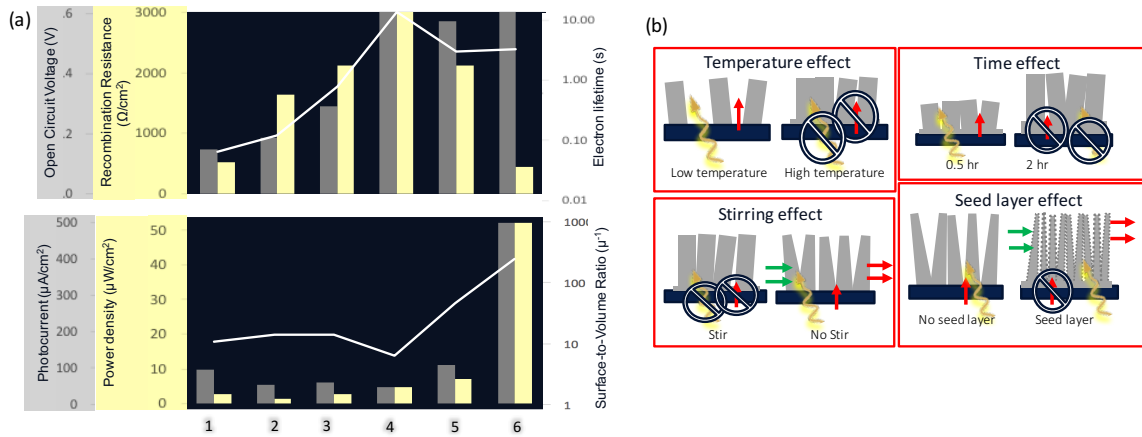
Figure 4.8. **(a) Performance parameters for DSCs prepared with ZVNR/G photoanodes: 1) 70, 2)75˚C and 3)80˚C grown stirred for 30min with and no seed layer, 4) time increased to 1hr at 75-80˚C, 5) stirring was removed, 6) seed layer was pre-deposited. (b) Illustration of how the electrodeposition parameters affect the mechanisms of power generation (green arrows) and loss (red arrows) in ZVNR/G photoanode in a DSC**

Despite the attempts to improve the photoanode performance, the power conversion efficiency of the DSC remained low (0.06%), which we attribute to low surface area of the ZnO. Alternative electrodeposition methods to fabricate ZnO NPs/Graphene heterostructures could provide much higher surface area for more frequent occurrence of photoelectric events and better photovoltaic performance, such as the codeposition of ZnO with Eosin Y dye, followed by etching of the dye[35].

4.5. References

1.   Mathew, S.; Yella, A.; Gao, P.; Humphry-Baker, R.; Curchod, B. F. E.; Ashari-Astani, N.; Tavernelli, I.; Rothlisberger, U.; Nazeeruddin, M. K.; Gratzel, M., Dye-sensitized solar cells with 13% efficiency achieved through the molecular engineering of porphyrin sensitizers. *Nature Chemistry* **2014,** *6* (3), 242-247.

2.   Badding, M. A.; Fix, N. R.; Orandle, M. S.; Barger, M. W.; Dunnick, K. M.; Cummings, K. J.; Leonard, S. S., Pulmonary toxicity of indium-tin oxide production facility particles in rats. *Journal of Applied Toxicology* **2016,** *36* (4), 618-626.

3.   Polgreen, L., Congo's Riches, Looted by Renegade Troops. *New York Times* 2008, p 14.

4.   comission, S. a. e., Final Rule-CO**NFLICT MINERALS** 2012.

5.   Xu, X. Z.; Zhang, Z. H.; Dong, J. C.; Yi, D.; Niu, J. J.; Wu, M. H.; Lin, L.; Yin, R. K.; Li, M. Q.; Zhou, J. Y.; Wang, S. X.; Sun, J. L.; Duan, X. J.; Gao, P.; Jiang, Y.; Wu, X. S.; Peng, H. L.; Ruoff, R. S.; Liu, Z. F.; Yu, D. P.; Wang, E. G.; Ding, F.; Liu, K. H., Ultrafast epitaxial growth of metre-sized single-crystal graphene on industrial Cu foil. *Science Bulletin* **2017,** *62* (15), 1074-1080.

6.   Zhang, Q. F.; Dandeneau, C. S.; Zhou, X. Y.; Cao, G. Z., ZnO Nanostructures for Dye-Sensitized Solar Cells. *Advanced Materials* **2009,** *21* (41), 4087-4108.

7.   Kayes, B. M.; Atwater, H. A.; Lewis, N. S., Comparison of the device physics principles of planar and radial p-n junction nanorod solar cells. *Journal of Applied Physics* **2005,** *97* (11), 114302-1-11.

8.   Lewis, N. S., Toward cost-effective solar energy use. *Science* **2007,** *315* (5813), 798-801.

9.   Mu, Q. H.; Li, Y. G.; Zhang, Q. H.; Wang, H. Z., Template-free formation of vertically oriented TiO2 nanorods with uniform distribution for organics-sensing application. *Journal of Hazardous Materials* **2011,** *188* (1-3), 363-368.

10.   Mamaghani, K. R.; Naghib, S. M., The Effect of Stirring Rate on Electrodeposition of Nanocrystalline Nickel Coatings and their Corrosion Behaviors and Mechanical Characteristics. *International Journal of Electrochemical Science* **2017,** *12* (6), 5023-5035.

11.   Khajavi, M. R.; Blackwood, D. J.; Cabanero, G.; Tena-Zaera, R., New insight into growth mechanism of ZnO nanowires electrodeposited from nitrate-based solutions. *Electrochimica Acta* **2012,** *69*, 181-189.

12.   Elias, J.; Tena-Zaera, R.; Levy-Clement, C., Electrodeposition of ZnO nanowires with controlled dimensions for photovoltaic applications: Role of buffer layer. *Thin Solid Films* **2007,** *515* (24), 8553-8557.

13.   Yin, Z.; Wu, S.; Zhou, X.; Huang, X.; Zhang, Q.; Boey, F.; Zhang, H., Electrochemical Deposition of ZnO Nanorods on Transparent Reduced Graphene Oxide Electrodes for Hybrid Solar Cells. *Small* **2010,** *6* (2), 307-312.

14.   Xu, C.; Lee, J. H.; Lee, J. C.; Kim, B. S.; Hwang, S. W.; Whang, D., Electrochemical growth of vertically aligned ZnO nanorod arrays on oxidized bi-layer graphene electrode. *Crystengcomm* **2011,** *13* (20), 6036-6039.

15.   Hambali, N. A.; Yahaya, H.; Mahmood, M. R.; Terasako, T.; Hashim, A. M., Synthesis of zinc oxide nanostructures on graphene/glass substrate by electrochemical deposition: effects of current density and temperature. *Nanoscale Research Letters* **2014,** *9*.

16.   Gao, L. B.; Ren, W. C.; Xu, H. L.; Jin, L.; Wang, Z. X.; Ma, T.; Ma, L. P.; Zhang, Z. Y.; Fu, Q.; Peng, L. M.; Bao, X. H.; Cheng, H. M., Repeated growth and bubbling transfer of graphene with millimetre-size single-crystal grains using platinum. *Nature Communications* **2012,** *3*.

17.   Villarreal, C. C.; Pirzada, D.; Wong, A. N.; Vi, D.; Pham, T.; Mulchandani, A., Characterisation of the heterojunction microstructure for electrodeposited vertical ZnO nanorods on CVD-graphene. *Materials Research Express* **2018,** *5* (8).

18.   Malekpour, H.; Ramnani, P.; Srinivasan, S.; Balasubramanian, G.; Nika, D. L.; Mulchandani, A.; Lake, R.; Balandin, A. A., Thermal conductivity of graphene with defects induced by electron beam irradtiation. *Nanoscale* **2016,** *8* (30), 14608-14616.

19.   Zarebska, K.; Kwiatkowski, M.; Gniadek, M.; Skompska, M., Electrodeposition of Zn(OH)(2), ZnO thin films and nanosheet-like Zn seed layers and influence of their morphology on the growth of ZnO nanorods. *Electrochimica Acta* **2013,** *98*, 255-262.

20.   Wang, M. S.; Jiang, L. X.; Kim, E. J.; Hahn, S. H., Electronic structure and optical properties of Zn(OH)(2): LDA+U calculations and intense yellow luminescence. *Rsc Advances* **2015,** *5* (106), 87496-87503.

21.   Zaban, A.; Greenshtein, M.; Bisquert, J., Determination of the electron lifetime in nanocrystalline dye solar cells by open-circuit voltage decay measurements. *Chemphyschem* **2003,** *4* (8), 859-864.

22.   Sarker, S.; Ahammad, A. J. S.; Seo, H. W.; Kim, D. M., Electrochemical Impedance Spectra of Dye-Sensitized Solar Cells: Fundamentals and Spreadsheet Calculation. *International Journal of Photoenergy* **2014**.

23.   Bisquert, J., Theory of the impedance of electron diffusion and recombination in a thin layer. *Journal of Physical Chemistry B* **2002,** *106* (2), 325-333.

24.   Scharifker, B.; Hills, G., THEORETICAL AND EXPERIMENTAL STUDIES OF MULTIPLE NUCLEATION. *Electrochimica Acta* **1983,** *28* (7), 879-889.

25.   Wipperman, K.; Schultze, J. W.; Kessel, R.; Penninger, J., THE INHIBITION OF ZINC CORROSION BY BISAMINOTRIAZOLE AND OTHER TRIAZOLE DERIVATIVES. *Corrosion Science* **1991,** *32* (2), 205-230.

26.   Nasirpouri, F., Electrodeposition of Nanostructured Materials. *Electrodeposition of Nanostructured Materials* **2017,** *62*, 1-325.

27.   Goux, A.; Pauporte, T.; Chivot, J.; Lincot, D., Temperature effects on ZnO electrodeposition. *Electrochimica Acta* **2005,** *50* (11), 2239-2248.

28.   Son, D. Y.; Bae, K. H.; Kim, H. S.; Park, N. G., Effects of Seed Layer on Growth of ZnO Nanorod and Performance of Perovskite Solar Cell. *Journal of Physical Chemistry C* **2015,** *119* (19), 10321-10328.

29.   Lin, Y.; Yang, J. Y.; Zhou, X. Y., Controlled synthesis of oriented ZnO nanorod arrays by seed-layer-free electrochemical deposition. *Applied Surface Science* **2011,** *258* (4), 1491-1494.

30.   Wan, W. T.; Zhu, L. P.; Hu, L.; Chen, G. F.; Mi, W. B.; Ye, Z. Z., Investigation of morphology evolution of Cu-ZnO nanorod arrays and enhancement of ferromagnetism by codoping with N. *Physics Letters A* **2014,** *378* (37), 2763-2767.

31.   Sarma, S.; Tatiparti, V.; Ebrahimi, F., Potentiostatic versus galvanostatic electrodeposition of nanocrystalline Al-Mg alloy powders. *Journal of Solid State Electrochemistry* **2012,** *16* (3), 1255-1262.

32.   Bera, D.; Qian, L.; Sabui, S.; Santra, S.; Holloway, P. H., Photoluminescence of ZnO quantum dots produced by a sol-gel process. *Optical Materials* **2008,** *30* (8), 1233-1239.

33.   Greene, L. E.; Law, M.; Goldberger, J.; Kim, F.; Johnson, J. C.; Zhang, Y. F.; Saykally, R. J.; Yang, P. D., Low-temperature wafer-scale production of ZnO nanowire arrays. *Angewandte Chemie-International Edition* **2003,** *42* (26), 3031-3034.

34.   Hsieh, C. T.; Yang, S. Y.; Lin, J. Y., Electrochemical deposition and superhydrophobic behavior of ZnO nanorod arrays. *Thin Solid Films* **2010,** *518* (17), 4884-4889.

35.   Minoura, H.; Yoshida, T., Electrodeposition of ZnO/dye hybrid thin films for dye-sensitized solar cells. *Electrochemistry* **2008,** *76* (2), 109-117.

Chapter IV:

Engineering of the ZnO/Protein/Electrolyte Interface for a Bacteriorhodopsin-Sensitized Solar Cell

Abstract

Bacteriorhodopsin (bR) is a protein found in the phototrophic system of *Halobacterium* purple membrane and is studied in this work for the bio-photoanode of a bR-sensitized solar cell (bR-SC). bR is a sustainable alternative to traditional synthetic dyes, which are expensive and, in many cases, toxic. However, the functional interfacing of bR with the semiconductor and electrolyte are not well-understood yet. To get more insight on how the interfaces are affected by fabrication parameters we studied bR-SCs using nanostructured ZnO on fluorine-doped tin oxide (ZnO/FTO). The photoactivity of the bR films thorough the experiments was assessed with ultraviolet visible absorption spectroscopy (UV-VIS) and the morphology of the bR film on ZnO was characterized using Scanning Electron Microscopy (SEM). The photoelectrochemical performance of the bR-SCs was determined by open circuit voltage (Voc) chronopotentiometry, linear sweep voltammetry (LSV), and electrochemical impedance spectroscopy (EIS). The protein immobilization mechanism was studied by comparing three different physical methods: dropcasting, pheniltriethoxysilane (PTES) chemical functionalization, and electrophoretic sedimentation. The photoanodes prepared by electrophoresis yielded the highest V_{oc}, attributed to the uniform orientation of the bR, followed by dropcasting where the random orientation of bR resulted in lower V_{oc}. The PTES dielectric layer caused the largest charge transfer resistance at the photoanode/electrolyte interface (R_{PA}) and the slowest kinetics of charge transfer (k_{PA}). Nevertheless, the R_{PA} of the bR-photoanodes in an iodide/triiodide (I^-/I_3^-) aqueous electrolyte were relative high ($>10^5$ $\Omega.cm^2$) for the three methods, in comparison with the values commonly reported for synthetic dyes ($<10^2$ $\Omega.cm^2$), and bleaching of the retinal was also observed. Therefore, partial delipidation of bR was investigated to improve interfacial interaction

with the ZnO substrate. The redox mediator selection was also investigated by comparing ferri/ferrocyanide $(Fe[(CN)_6]^{3-/4-})$ and hydroquinone/benzoquinone (HQ/BQ) to the traditional I^-/I_3^- mediator, considering their biocompatibility and good energy alignment with the bR-SC elements. The highest bR photoresponse was observed for HQ/BQ mediator. Therefore, the presence of protons in the HQ/BQ electrolyte and the addition of surfactants were examined for this system. The presence of a proton source and a surfactant improved bR film stability, enhanced the bR-SC power output and reduced the R_{PA}. This work provides a framework for the future advancement of bR-SCs and the integration of biomolecules as functional elements in solid/liquid bionanointerfaces.

5.1. Introduction

Several natural phototrophic systems that harvest energy from sunlight in living organisms are being explored to develop sustainable biophotovoltaic devices[1-4]. The protein bR embedded in the cell purple membrane of *Halobacterium* is a model system that has been studied for a few decades due to the transduction mechanisms it performs and its better stability in comparison to photosynthetic systems[5, 6]. With a thickness of ≈5nm and a quantum yield efficiency of almost 100%, bR is considered the most stable of all membrane proteins studied so far[7]. The extremely halophilic archaeon *Halobacterium* is a heterotroph organism under aerobic condition, but, when resources become scarce it induces biogenesis of purple membranes and turns phototrophic. When bR is photoexcited, it pumps protons from the cytoplasmic to the extracellular side of the membrane and creates an electrochemical gradient. The energy stored in such transmembrane electrochemical gradients is central to the bioenergetics of phototrophic and non-phototrophic living beings. Therefore, understanding the light harvesting, exciton formation and transfer of electrons and ions in a bR-SC is a significant contribution to bioelectronics. The interactions between biomolecules and nanomaterials is still not fully understood and the development of fully synthetic or hybrid bioinspired devices is still in its infancy[8].

The purple membranes are two-dimensional hexagonal lattices of bR trimers as illustrated in **Figure 5.1(a)**. bR is a 27kDa, seven alpha helices protein composed of 1:1 complex of bacterioopsin (Bop) and the retinal chromophore as shown in **Figure 5.1(b)** [9]**.** The bR aminoacid sequence is shown in **Figure 5.1(c)**. The photocycle starts when the retinal bound to Lys-216 (yellow circle) via a protonated Schiff base linkage is photo-excited and undergoes conformational isomerization. The 200 kJ/mol absorbed by the system cause destabilization, leading to the deprotonation of the Schiff base. The cycle goes on with further formation and breakage of proton conduction paths, where donor/acceptor amino acids are glutamic and aspartic acid (brown circles). After re-protonation, the retinal re-isomerizes to the initial stage thermally. bR can undergo many photocycles before it denatures, making it feasible for artificial non-living systems where protein regeneration doesn't occur [10].
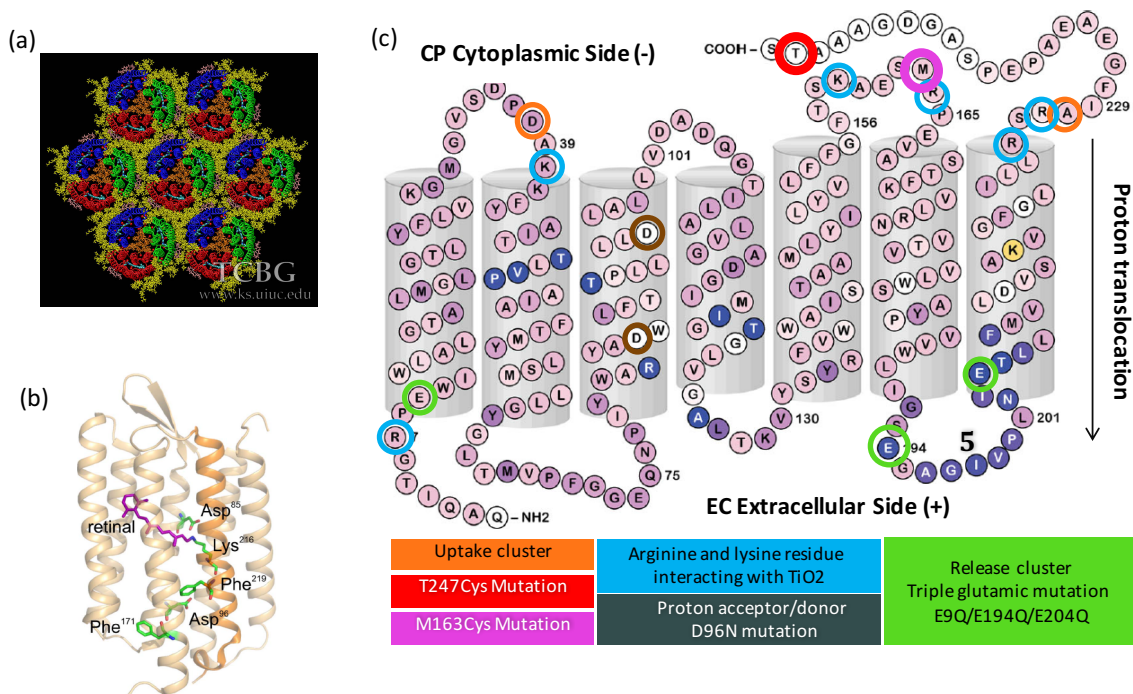
Figure 5.1.   (a) Lattice of bR trimers in purple membrane[11]. (b) Cartoon representation of the 3D structure of BR. The retinal chromophore (purple) is covalently bond via a Schiff base to Lys-216 [12] taken from Geibel, S 2013 CC-BY 4.0 (c) Amino acid sequence of the BR protein. Adapted from Wagner, N 2013 CC-BY 4.0[10]

The use of bR as a solar energy-harvesting element in biophotovoltaic devices has been attempted in multiple ways. The most promising results in terms of efficient energy conversion have been obtained when bR is incorporated in electrochemical cells with liquid electrolyte, rather than in thin film solid-state devices. The photovoltage of solid–state devices is in the order of 10^{-1}-10^1 mV [13], although some studies reported photovoltages as high as 300mV for 170um thick films [14]. However, the poor conductivity of BR in solid state (10^{-7} S/cm) [15] results in low power output with photocurrents in the order of nA and pA [16]. In solid state no translocation of proton occurs and the photocycle is different and slower [17, 18]. Wet devices inspired in the organism physiology have been reported, using bR-impregnated porous membranes to separate two chambers containing aqueous solutions [19, 20] or proton selective membrane separating two aqueous half-cells, one with BR suspension. Even though the addition of plasmonic Ag NPs in the bR half-cell induced faster bR cycle and increased the photocurrent by 50-fold, the power output of such membrane-separated photocells is low [21, 22].

bR is a biocompatible, biodegradable, non-toxic and environmentally friendly alternative to synthetic dyes used in dye-SCs and it is easy to produce industrially[23, 24]. It complies with the stability, high quantum yield, and extended excited state lifetime required for a sensitizer[25]. Unlike synthetic organic dyes, bR is water stable, and transitioning into aqueous SCs is desirable to reduce their cost, flammability and volatilization of toxic compounds[26]. A timeline of the development of bR-SC is detailed in **Table 5.1.** The first bR-SC was proposed in 2009 by the group of Renugopalakrishnan, based on the lowest-unoccupied molecular orbital (LUMO) of bR that is located at -3.8eV, favorable for electron injection into the conduction band of TiO_2 at -4.2eV, and its highest-unoccupied molecular orbital (HOMO) that is located at -5.2eV, suitable for being reduced by the I^-/I_3^- pair. The wild type protein was compared to mutant E9Q/E149Q/E204Q (green circles **Figure 5.1(c)**) designed promote binding to the TiO_2 and favor electron transfer, from which the mutant bR-SC had a better performance, but it was also less chemically and thermally stable than the wild type [27]. bR sensitized photoanodes have been studied to produce solar H_2

and shown photocurrents significantly higher than previous studies [28, 29]. Several variables to improve the cell performance have been studied: the treatment of the TiO_2 with $TiCl_4$ to increase the porosity of the NPs [30], the use of nanofiber scattering layer to enhance the optical path length, the time and temperatures of bR incubation on TiO_2 [31], the combination with bacterioruberin pigment from the same organism [32], the immobilization of bR by Langmuir-Blodgett method on ZnO NP [33], the TiO_2 morphology [34] and the substitution of liquid electrolyte by gel electrolyte [35]. The bR-SC with the highest PCE of 0.49%[35] and stability for more than 3 months[31] demonstrates that bR can yield performance comparable to synthetic dyes when the platform is properly designed. A proposed advance is the combination of bR with QDs to improve cell performance[36, 37].

Table 5.1. Summary of structure and performance of BR-sensitized solar cells reported in literature

Ref	Transparent conductor, Counter electrode	Semiconductor	Electrolyte	Light source	J_{sc} (mA/cm^2)	V_{oc} (V)	n (%)	FF (%)
27	FTO, Al/FTO	Sprayed TiO_2 nanorods 0.5g P25 30nm Degussa in 20ml EtOH:MeOH 1:1 15um	0.1 M LiI, 0.03 M I_2, 0.5 M KCl Tris buffer pH 8	Xe, 40mW/cm^2	0.04, 0.03, 0.09	0.39	NA	NA
30	FTO, Pt and C	TiO_2 paste treated with $TiCl_4$	I^-/I_3^- (Solaronix, Iodolyte AN-50)	AM1.5 Solar simulator	0.28	0.51	0.09	62
32	FTO, Pt	TiO_2 paste treated with $TiCl_4$, sensitized with BR and bacterioruberin (r)	I^-/I_3^- (Sharifsolar)	AM1.5 Solar simulator	0.45 (BR+r) 0.4(BR) 0.25(r)	0.57 (BR+r) 0.51(BR) 0.61(r)	0.16 (BR+r) 0.11(BR) 0.08 (r)	62
33	FTO, Pt	ZnO NPs paste (Sharifsolar)	I^-/I_3^- (Solaronix)	AM1.5 Solar simulator	0.39	0.5	0.1	52
34	Ti, Pt wire, AgCL ref	TiO2 NPs paste (Sharifsolar)	Phosphate buffer pH8	Xe 110W	0.64@0.5V	Onset -0.59	16.5	NA
		TiO_2 Nanotubes anodization			0.12@0.5V	Onset -0.58	1.9	NA
31	FTO, Pt	TiO_2 paste (Platisol T/SP Solaronix), treated with $TiCl_4$+scattering layer TiO_2 nanofibers	I^-/I_3^- (Solaronix)	AM 1.5 Solar simulator	1	0.533	0.35	66
35	FTO/Pt	TiO_2 NPs paste	I^-/I_3^- polymer gel electrolyte 5% acetamide [38]	85 mW/cm^2 solar simulator	1.08	0.67	0.49	58

The bR-SC is a heterojunction device formed between the donor (bR) and the acceptor (ZnO, TiO_2)[27]. Even though this is not the natural tranduction mechanism performed by the bR phototropic system, it has proven more efficient. The electrochemical gradient generated by BR in the bacteria is only 200mV [39], and

values up to 570mV were obtained in bR-SC, demonstrating that rational novel designs of energy transduction can expand the natural capabilities of biosystems.

The interface of ZnO/bR plays a crucial role in the performance of the bR-SC. ZnO has high ionic bonding (60%) and isoelectric point (9.5) which makes it have a strong electrostatic attraction and binding of low isoelectric proteins [40, 41] and it is stable at pH 7.3 in biological media [42]. The conduction band of ZnO aligns well for electrons to be injected from the LUMO of bR (see **Figure 5.2**). The technique of protein immobilization on the electrode surface has been shown to significantly affect the cell output of solid state devices[43, 44]. In contrast to TiO_2 bR-SC reports[27, 31], simple electrostatic binding by incubating the ZnO/FTO electrode in aqueous suspension of bR does not result in bR immobilization. Despite of the high isoelectric point (IEP) of 9.5 for ZnO and the low IEP and electric dipole of bR of 5 [45], deviations from the ideal electrostatic map of bR charged amino acids may take place locally[27], making the development of a strong electrostatic bond difficult. Covalent bonding and Langmuir-Blodgett techniques have been reported for bR immobilization on ZnO [46, 47].
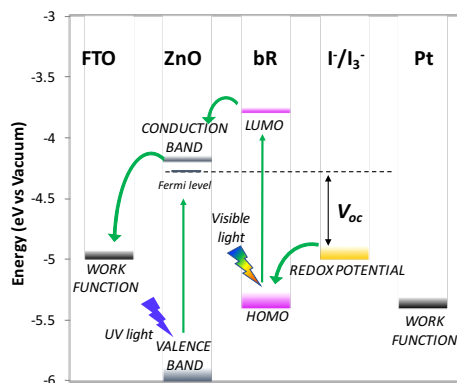
Figure 5.2.   Energy level diagram for a bR-SC

The bR/electrolyte interface is also crucial for the bR-SC performance. It is necessary to find alternative redox mediators to I^-/I_3^- due to its low solubility in water and corrosiveness. The electron shuttles in biological systems are sulfur, aromatic rings and metallic atoms. The chemistry of the thiol group for SCs has been highlighted in literature, with redox pairs such as cysteine/cysteine[48] or disulfide/thiolate[49].

$[Fe(CN)_6]^{3-/4}$ pair[50-53] and quinones [54, 55] are biocompatible mediators that have been studied for SCs. have also been studied as electron mediators in Dye-SCs and in bio-photoelectrochemical cells fabricated with bacterial reaction centre[56, 57] and photosystem II [58]. The combination of the Fe-containing cytochrome *c*, with quinones and synthetic dyes have been combined as mediators in SCs too, inspired in the proton-coupled electron transfer (PCET) occurring in photosynthesis [59, 60]. Even though the link between redox processes and transmembrane proton gradients is the unifying concept in bioenergetics, it has been mostly disregarded in the design of biophotovoltaics. PCET is the movement of an electron from one site to another accompanied by proton transfer. PCET and the transport of protons over tens of angstroms are important in all living cells because they are a fundamental link between redox processes and the establishment of transmembrane gradients of proton electrochemical potential, known as proton-motive force, which is the unifying concept in bioenergetics. PCET has attracted attention from the scientific community recently as an approach to extend the lifetime of charge-separated states and help with kinetic competition between power generation and charge recombination processes [61, 62]. Beside the chromophores for light absorption and electron donors and acceptors, an artificial photoelectrochemical cell incorporating PCET must have the and proton donors and acceptors[61]. Electron and proton low resistance current pathways ("wires") need to be developed across the entire system [61]. Coupling electron transfer processes with proton currents helps to extend the lifetime of charge-separated states as it competes with recombination reactions.

The wettability of the SC photoanodes influences the charge transfer at the bR/electrolyte interface. *Excessive hydrophilicity of the SC surface favors sensitizer molecule desorption, thus decreasing the photocurrent and the stability over time; on the other hand, highly hydrophobic dyes do not allow the complete wettability of the electrode which, in turn, results in a less effective regeneration process for aqueous electrolytes. An optimum between these two extremes has not been achieved so far, and the creation of an intimate photoanode/electrolyte interface will be one of the main research goals in the coming yearsThe addition of surfactants has been demonstrated to improve SC performance[26, 63].*

In this work, we engineered the interfaces of ZnO/bR/electrolyte hterostructure for bR-SCs. The ZnO/bR interface was studied by comparing three different methods for purple membrane immobilization: dropcasting, electrophoretic sedimentation, and chemical functionalization with PTES, and by using partial delipidation of bR to improve protein-ZnO ontact. The bR/electrolyte interface was studied by comparing three different redox mediators I^-/I_3^-, $[Fe(CN)_6]^{3-/4}$ and HQ/BQ. The proton presence in the electrolyte was investigated in the HQ/BQ system to get more insight on PCET processes and the effect of surfactant addition was assessed to improve the wettability of the photoanode. The functionality of the bR films was verified by UV-Vis and their morphology was characterized with SEM. The bR-SCs R_{PA} and k_{PA} were measured through EIS and their photovoltaic performance was evaluated with V_{OC} chronopotentiometry and LSV.

5.2. Experimental Procedures

5.2.1.   bR-photoanodes preparation

Fluorine-doped tin oxide (FTO) coated glass (~7Ω/sq) (Sigma-Aldrich) was cleaned with distilled water water, sonicated in acetone, rinsed with isopropyl alcohol and dried under nitrogen. Then it was annealed at 400˚C and cooled down followed by immersion in HNO_3 40% for 2min. A thin film of ZnO NPs was deposited on the conductive part of FTO. The ZnO paste was composed of 1:1 ratio of commercially available ZnO NPs 40-100 nm (Alfa Aesar Nanotek #44899) and 10-30nm (US Research Nanomaterials #US35909). The paste was prepared by sonicating the NPs with 2-butanol in 1:6 weight ratio and 3% acetic acid as dispersant. This paste was applied by slip-casting a layer of 15 μl/cm^2 on the TC and evaporating the solvent at 50°C. Afterwards, they were annealed in a heating furnace (OTF-1200x, MTI Corp) at 450˚C for 30 minutes. A PDMS dielectric spacer of 50 μm thickness was casted on top of the ZnO/FTO before immobilizing the bR to avoid exposing the protein to high temperatures of PDMS curing, leaving a 1cm^2 photoactive area exposed. The ZnO/FTO electrodes were subjected to UV-ozone treatment for 30min to

increase its hydrophilicity right before bR immobilization, using a Hi Q Engineering UltraViolet Ozone Cleaner.

The wild type strain NRC-1 and mutant D96N bR were studied in its purple membrane and partially delipidated forms. The purple membrane was provided by Dr. Senthil Prasad from the CSIR-IMTECH research institute from India. The partially delipidated form was provided by Dr. Renugopalakrishnan from Northeastern University. The bR was purified before using it by centrifuging at 12000 rpm for 30 min followed by supernatant extraction and refilling, process that was repeated three times. The protein was suspended in 5mM tris buffer solution pH 8 or deionized (DI) water with concentration 2mg/ml.

Three methods were studied for protein immobilization on the ZnO/FTO substrate, using 30 μl/cm^2 of the bR suspension. For dropcasting, the bR was deposited at room temperature on the ZnO/FTO substrate and dried. For the PTES technique, the ZnO/FTO substrate was incubated in PTES 100% (Sigma-Aldrich) in a 50 °C water bath for 1 hour. Then, the bR was deposited on the ZnO/FTO and incubated for 12 hours. For electrophoretic sedimentation, the bR was suspended in DI and injected between the ZnO/FTO substrate and an FTO counter electrode separated by the PDMS dielectric. The electric field was applied for 12 min using a semiconductor parameter analyzer HP 4155A, as illustrated in **Figure 5.3**. After the immobilization process, the substrates were rinsed with a buffer solution and with DI water to remove the weakly adhered protein from the ZnO surface.
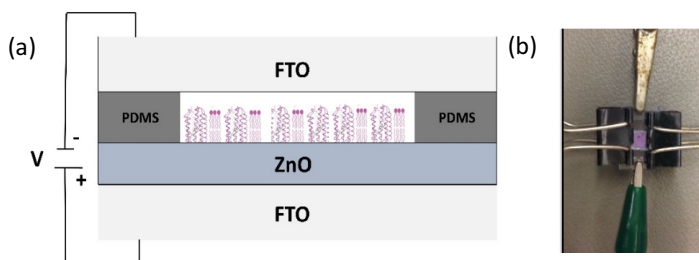
Figure 5.3.   Experimental setup for BR immobilization on ZnO by electrophoretic sedimentation (a) schematics and (b) photograph.

Scanning electron microscope (SEM) was used to characterize the BR-ZnO interface using a FEI NanoSEM 450 with voltages between 5 and 20 kV. UV-Vis absorbance was acquired using a spectrophotometer DU 800, Beckman Coulter. UV-Vis absorbance for suspensions was taken in quartz cuvette. UV-Vis absorbance of bR on glass was taken on glass slides previously cleaned with soap, acetone and IPA, then 30 μl of bR (2mg/ml in 5mM Tris buffer pH8) was deposited on each slide, and air dried, process that was repeated twice. UV-Vis absorbance of bR/ZnO/FTO and blank ZnO/FTO was taken from the prepared photoanodes.

5.2.2.   Electrolyte preparation and characterization

The I^-/I_3^- redox pair was studied in aqueous and organic media. The I^-/I_3^- aqueous electrolyte was composed of 0.1 M LiI, 0.03M I_2, and 0.5 M KCl in aqueous solution. The I^-/I_3^- acetonitrile electrolyte was composed of 0.1 M LiI, 0.03M I_2, and LiClO$_4$ in 2:1 ratio of acetonitrile to ethylene carbonate. The aqueous $[Fe(CN)_6]^{3-/4-}$ electrolyte was composed of 200mM $K_4Fe(CN)_6$ and 20mM $K_3Fe(CN)_6$, 50mM KCl in Tris Buffer 40mM pH 8. The HQ/BQ electrolyte for bR-SCs was prepared in acetonitrile 0.2 M HQ and 0.1M LiClO$_4$ and BQ was produced by linear sweep voltammetry. The cyclic voltammetry of the electrolytes was performed with CHI 760C electrochemical station at a rate of 100mV/s and the data of the third consecutive cycle was used for displaying and extracting the electrochemical data. The working electrode was Pt disk and the counter electrode was Pt mesh. The reference electrode for aqueous electrolytes was Ag/AgCl filled with saturated KCl (Ag/AgCl$_{Sat'dKCl}$), and for organic electrolytes it was Ag/Ag$^+$ filled with 0.01M AgNO$_3$ and 0.1M tetrabutylammonium perchlorate (TBAP) in ACN (Ag/Ag$^+_{0.01MAgNO3/0.1MTBAP/ACN}$). The Ag/AgCl$_{Sat'dKCl}$ reference electrode has a fixed relative potential of 0.199V vs NHE, but the Ag/Ag$^+_{0.01MAgNO3/0.1MTBAP/ACN}$ reference electrode has different potential vs NHE depending on its filling solution. To calibrate the Ag/Ag$^+_{0.01MAgNO3/0.1MTBAP/ACN}$ reference electrode, formal potentials were determined versus ferrocenium/ferrocene (Fc$^+$/Fc) as a reference system, and then versus normal hydrogen electrode (NHE) with a value established for $E_{1/2,Fc+/Fc}$=0.64 V vs NHE in acetonitrile and 25 °C [55, 64]. The $E_{1/2,Fc+/Fc}$ was measured

in 0.01M Ferrocene, 0.01M TBAP electrolyte. The $E_{1/2,Fc/Fc+}$= -5mV vs Ag/Ag$^+_{0.01MAgNO3/0.1MTBAP/ACN}$ = 630mV vs NHE, therefore the potential of Ag/Ag$^+_{0.01MAgNO3/0.1MTBAP/ACN}$ is 635mV with respect to NHE.

5.2.3.   Counter electrode preparation

The counter electrode used for I$^-$/I$_3^-$ and [Fe(CN)$_6$]$^{3-/4-}$ was a Pt(40nm)/Ti(40nm) film e-beam evaporated on glass using Temescal BJD 1800. Three additional counter electrodes were compared for the HQ/BQ system: (1) graphite/FTO, (2) PEDOT:PSS/FTO and (3) PtNPs/Ptfilm. The (1) graphite/FTO electrode was prepared by using pencil 6B on cleaned FTO substrate. The (2) PEDOT:PSS/FTO was used because of PEDOT's high activity with quinones[55] and was prepared by spincoating the PEDOT:PSS on FTO cleaned and pretreated with UV-Vis for 5min[65].The (3) PtNPs/Ptfilm electrode was prepared by dropcasting 10 mM H$_2$PtCl$_6$ ethanoic solution on the e-beam evaporated Pt(40nm)/Ti(40nm) film for one, two or three times at 150˚C and annealing to 500˚C for 1hr in air. Cyclic voltammetry was applied to compare the electrocatalytic activities of the four materials for HQ/BQ electrolyte, using the fabricated electrodes as working electrodes, Pt mesh as counter electrode and Ag/Ag$^+_{0.01MAgNO3/0.1MTBAP/ACN}$ as reference electrode.

5.2.4.   Photoelectrochemical characterization of bR-SCs

The bR-photoanodes were used as working electrodes in a bR-SC electrochemical solar cell. Two replicates were tested for each variable to assess reproducibility. Blank cells, ZnO/FTO without bR, were tested as control. The photoanode with the PDMS spacer was clipped with the counter electrode and the electrolyte was injected in between through two pre-drilled holes in the counter-electrode. Electrochemical measurements were taken under an irradiation intensity of 100 mW/cm^2 from an USHIO Xe 75W lamp connected to an LPS-220B (OBB®) lamp power supply. UV radiation was filtered with a pass filter for some experiments. To determine the performance of bR-SCs, a CHI 760C potentiostat was used to apply LSV, V$_{oc}$ chronopotentiometry and EIS. LSV was measured from 0 to -500mV with a rate of 100 mV/s. The V$_{oc}$ of the cell was monitored when switching the light on and off using an automated shutter. EIS was measured

under illumination, within a frequency range of 0.1 Hz to 10^5 Hz, at the V_{oc} of the cell and an amplitude of 10 mV. The experimental EIS data was analyzed by fitting an equivalent circuit model, as described in Chapter 1 [66-68] with an error less than 10%.

5.3. Results

The absorbance of wild type bR purple membrane suspended in phosphate buffer is shown in **Figure 5.4**. The peak in a range of 500 to 600 nm corresponds to the absorbance of the protonated Schiff-base retinal chromophore encapsulated within the protein. The peaks between 250 to 300 nm correspond to aromatic amino acids (Tyr, Phe, Trp). The ratio of absorbance at A280/A570 is 2.6.
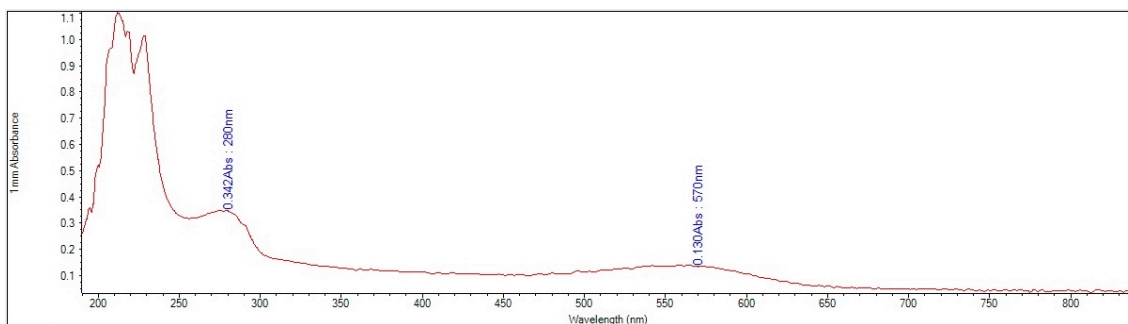
Figure 5.4.   UV-Vis absorbance of NRC-1 wid type BR suspension in water (0.225mg/ml)

The morphology of the bR purple membranes dropcasted on ZnO/FTO can be observed in the SEM micrographs in **Figure 5.5(a-d)**. The bR coating is dense, continuous and uniformly distributed on the ZnO substrate. Even though the PM fragments are soft material and conform to the surface morphology, they do not penetrate deep into the mesoporous layer of ZnO. The bR forms a multilayer lamellar 1-3 µm thick coating on the ZnO surface. The presence and functionality of the protein on the substrate are confirmed in the UV-Vis aborbance of **Figure 5.5(e)**. After immobilization on the substrate, the retinal peak at 550 nm is still evident, confirming not only the presence of bR on the surface, but also the stable photoresponse of the retinal molecule. This peak is not observed in the ZnO/FTO reference.
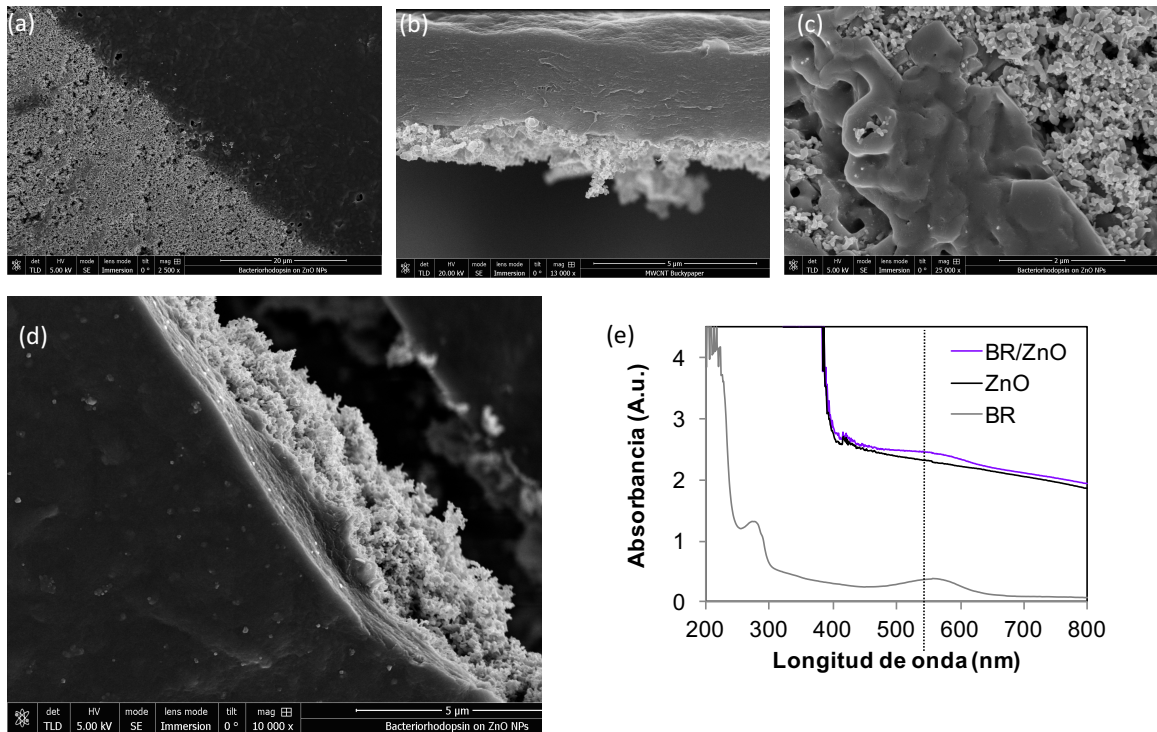
Figure 5.5. **(a-d) SEM micrographs of bR purple membane on ZnO, (e) UV-Vis spectrometry curve for the suspended BR, the ZnO/FTO substrate, and the BR/ZnO/FTO heterostructure.**

5.3.1. *Effect of protein immobilization method*

We studied the R_{PA}, f_{PA} and photovoltaic performance of bR-SCs prepared by different physical methods for immobilization of wild-type bR purple membranes on ZnO. In dropcasting, rapid dehydration of bR in ambient air caused peeling of the ZnO as shown in **Figure 5.6(a)**, while drying in saturated humidity effectively impregnated the bR to the ZnO without mechanical failure of the film, as shown in in **Figure 5.6(b)**, indicting that slow drying rate is necessary to ensure stability of the bR/ZnO/FTO interface.
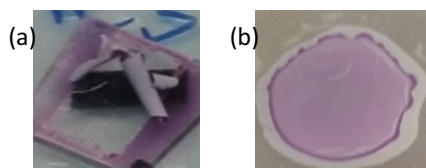
Figure 5.6. **Samples prepared by the dropcasting method dried in (a) ambient air and (b) saturated humidity**

To improve the binding of the hydrophobic purple membranes, the surface of ZnO was made hydrophobic too, by chemical functionalization with PTES, as shown in **Figure 5.7(a)**. When the un-treated ZnO surface was functionalized with PTES, the contact angles did not change (~ 30°) and the bR film was not homogeneous (**Figure 5.7(b)**). When a pre-treatment of UV/ozone and hydration was applied to ZnO before PTES functionalization, the contact angle increased to 77° and a more uniform layer of bR was obtained (**Figure 5.7(c)**). During silanization, hydroxylation of the PTES molecule occurs in the presence of water molecules; therefore, hydration of the surface is a determinant factor in the functionalization process [69].
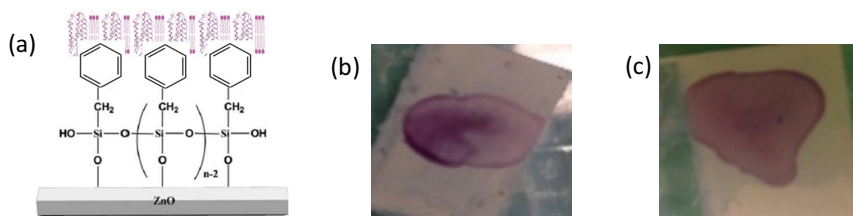
Figure 5.7.   bR immobilization on functionalized ZnO using PTES molecules, (a) molecular structure, (b) bR film on ZnO/FTO with PTES functionalization without pre-treatment of the ZnO, and (c) with pre-treatment of the ZnO with UV-ozone and hydration

To obtain selective bR orientation, the electrophoretic method was used, by applying a positive electric potential on the ZnO to attract the cytoplasmic side of the bR, which contains the C-terminus of the protein that 7 is more negative at pH and contains carboxyl groups that could bind to the ZnO, orientation that has been demonstrated to yield the largest photoresponse[44]. The evolution of the process, from suspended purple membranes to an immobilized film, is shown in **Figure 5.8(a)**. In this method, the purple membrane film quality depends on the applied electric field, as illustrated in **Figure 5.8(b-d)**. An applied electric field of 30 V/cm caused few molecules of bR to be immobilized. When the electric field was increased to 50 V/cm, the deposition was much more efficient. At 60 V/cm, bubbles are formed due to water electrolysis, causing damage the ZnO film. The deposition was not completely uniform with this method and it had poor reproducibility, probably because the uneven ZnO slip-casted film resultd in local variation of electric field.
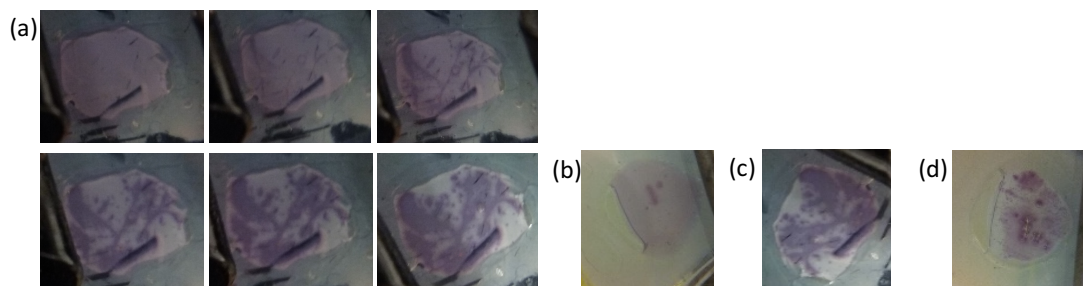
Figure 5.8. **(a) bR immobilization applying ES technique with 50 V/cm, picture taken every 2 minutes. Samples prepared by the electrophoretic sedimentation applying an electric field (b) 30, (c) 50 and (d) 60 V/cm**

The SC performance depends on charge transfer at the photoanode interface, described by the R_{PA} and f_{PA}. To compare the effect of immobilization on the electron transfer, EIS was perform for the bR-SCs using aqueous I^-/I_3^- electrolyte. The EIS Nyquist and Bode plots are shown in **Figures 5.9(a-b)**. The R_{PA} and (f_{PA}) is summarized for each immobilization method in **Table 5.2**. The resistance of the transparent conductor (R_{TC}) and charge transfer resistance at the counter electrode (R_{CE}) are less than 40 $\Omega.cm^2$ for all the samples, indicating that they are not the limiting factor of the cell. In contrast, R_{PA} fitted values were around 200 kΩ, similar to previous reports [70, 71]. The high impedance shown by the BR-SCs could be explained by the multilayer film observed in the SEM micrograph in **Figure 5.5(d)**, as multiple bR layers increase the photocurrent up to a suitable number after which the response begins to fall [71]. The electrophoresis and dropcasting methods resulted in cells with comparable R_{PA}, as the interface is very similar in structural terms; however, it is observed that f_{PA} is faster for electrophoresis, indicating that the selective orientation of the protein produces faster electron transfer. In the case of the PTES chemical immobilization, R_{PA} is 50% higher, and f_{PA} is slower. Although the PTES ligand facilitates protein immobilization on the substrate, it also increases the electrical resistance of the system, functioning as a dielectric layer[69].

Table 5.2.   Charge transfer resistance R_{PA} and rate f_{PA} for bR-SC fabricated by different immobilization metods

		Electrophoresis	Dropcasting	PTES
Charge transfer resistance	R_{PA} ($k\Omega.cm^2$)	197	195	270
Charge transfer rate	f_{PA} (Hz)	1.65	0.45	0.22
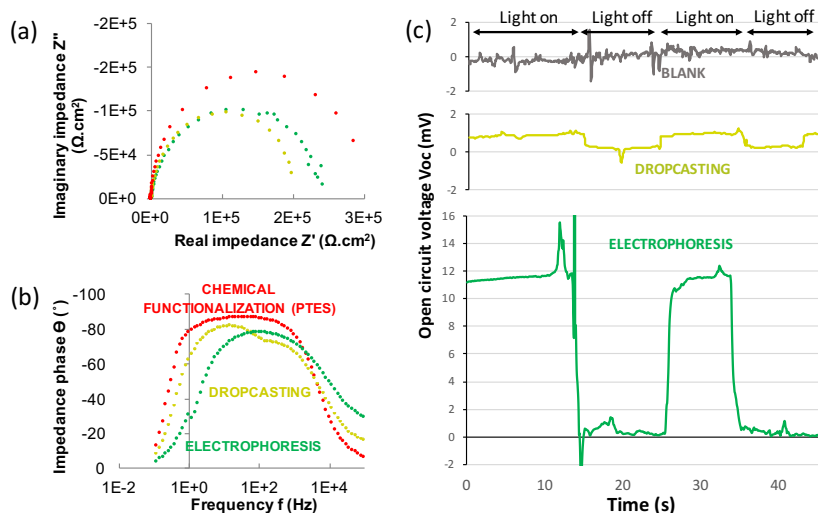
Figure 5.9.   Photoelectrochemical characterization of bR-SCs fabricated using different immobilization techniques and filled with aqueous I^-/I_3^- electrolyte. (a) EIS Nyquist and (b) Bode phase diagram. (c) V_{OC} chronopotentiometry

The V_{OC} chronopotentiometry of the bR-SCs measured using UV-filter is shown in **Figure 5.9(c)**. The blank cell did not produce any photo-response, in contrast to bR-SCs that generated photo-voltage upon illumination. The photovoltage of the bR-SC is maintained as long as the light is on, indicating a continuous electron pumping, in contrast to to other bR devices where only transient phorovoltage peaks are produced there is a variation in the illumination[44]. This photo-voltage results from the charge density differences between the extracellular side and the cytoplasmic side of the bR protein formed when the retinal molecule pumps protons from one side of the purple membrane to the other. The bR-photoanode fabricated by electrophoresis produces a photovoltage 12 times larger than by dropcasting. As illustrated in **Figure 5.1(c)**, proton pumping in bR is unidirectional, from the cytoplasmic side to the extracellular side. The electrochemical gradient formed is a vector, and the sum of all vectors in the bR film results in the total V_{OC} of the cell, therefore, bR orientation is a critical aspect for its application in photovoltaics. The electric field

applied during electrophoresis causes uniform orientation of the membranes on the substrate, due to the dipolar moment of the biomolecule, and maximizes the sum of vectors to produce a larger photovoltage. The random orientation in dropcasting results in opposing vectors that lead to field compensation and reduction of net charge transfer. Similar results have been reported for a bR solid-state device, where films with selective orientation have shown photocurrent of 820 pA, in comparison to 15 pA for randomly oriented films[20].

5.3.2.   Effect of partial delipidation of bR

To obtain functional interfacing of natural membrane proteins with synthetic materials it is important to determine if the protein should be kept membrane-bound or be separated from the lipids. The protein gains stability from the lipid matrix when expressed in the native organism and its isolation considerably decreases the biochemical and thermodynamic stability. On the other hand, the purified bR is a smaller particle and may have less steric hindrance and more accessibility to bind to the ZnO, with closer distance to substrate for improved charge transfer. We compare the film morphology of purple membranes and partially delipidated bR dropcasted on ZnO NPs with photographs and SEM micrographs in **Figures 5.10(a-d)**. The photographs show that purple membranes form agglomerates on the surface of the ZnO, while the partially delipidated bR forms a continuous homogeneous film. The cross-sectional SEM shows a clear interfacial separation between ZnO and purple membranes, while a more intimate contact and slightly deeper penetration is observed for the partially delipidated bR inde the pores of the ZnO film. In either case, the bR forms a film on top of the ZnO, instead of penetrating the pores. The bR is considered one of the smallest intrinsic proteins with a molecular weight of only 24,000 Da, globular monomers have diameters of 3-5nm[72, 73] therefore, the largest bR trimer size could be 15nm. Depositing 30 ul of bR suspension with concentration 2mg/ml the in estimated bR density is 2.5×10^{-9} mol/cm^2 of ZnO geometrical area. For a nanostructured ZnO electrode made with 30nm NPs and 20 μm thickness, the surface area to geometrical area ratio is approximately 1000:1[74], therefore the bR density is estimated to be 2.5×10^{-12}

mol/cm^2 of ZnO surface area. For the protein formate dehydrogenase with MW from Desulfovibrio gigas, with a total molecular weight of 134kDa, a densely packed monolayer was formed on a freshly polished pyrolytic graphite edge electrode with a concentration of 3.7x10^{-12} mol/cm^2 surface area[75].
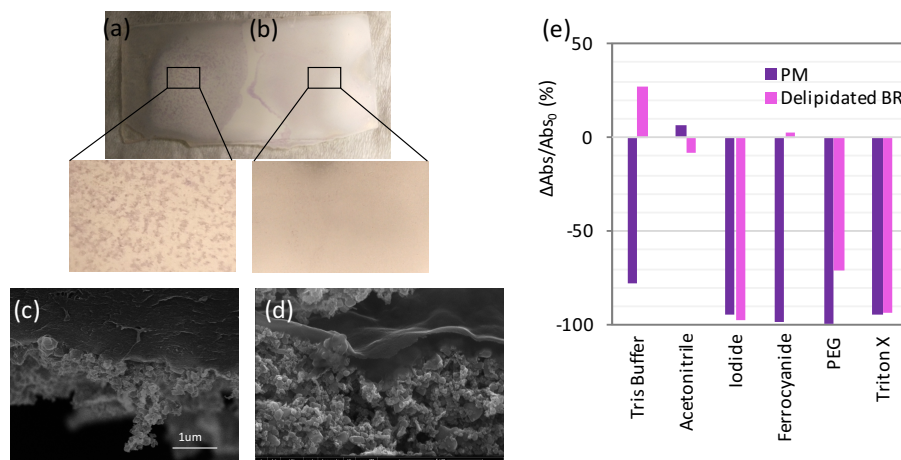
Figure 5.10. Photographs of (a)purple membrane and (b) partially delipidated bR on ZnO NPs. Cross-sectional SEM micrographs of (c) purple membrane and (d) partially delipidated bR on ZnO NPs. (e) Stability of purple membranes and partially delipidated bR thin films on glass in electrolyte components measured as ΔAbs ∕Abs$_0$ of the retinal

We compared the stability of purple membrane and partially delipidated bR films dropcasted on glass towards different electrolyte components. The UV-Vis absorbance of retinal (~550nm) was measured for the films before and after immersing for 2hrs in acetonitrile and aqueous solutions of tris buffer, I$^-$/I$_3^-$, [Fe(CN)$_6$]$^{3-/4-}$, PEG and TritonX. **Figure 5.10(e)** summarizes the normalized change of absorbance of the retinal peak, $\Delta Abs/Abs_0$, given by Equation 1.

$$\Delta Abs/Abs_0 = \frac{Abs - Abs_0}{Abs_0} \qquad \text{Equation 1}$$

For purple membrane films, the retinal absorbance decreased between 80 and 100% in all aqueous solutions, and 10% in acetonitrile. For partially-delipidated bR the absorbance decreased by 90-100% in I$^-$/I$_3^-$ and Triton X, by 70% in PEG and remained stable in acetonitrile and tris buffer and [Fe(CN)$_6$]$^{3-/4}$. The UV-Vis results indicate that the partially delipidated bR films are more stable on oxide than the purple membranes. The photographs and SEM micrographs also indicate a better interaction for the partially delipidated bR with ZnO than the purple membranes. The partial delipidation of the membrane protein

improves the contact between the bR and the oxide substrate, which we attribute to reduction of protein hydrophobicity and exposure of more aminoacids residues for additional interaction with oxide surface.

5.3.3. Effect of redox mediator selection

The LSV of bR-SCs fabricated with I^-/I_3^- ACN electrolyte in **Figure 5.11(a)** shows that the use of organic solvent higher V_{oc} (~200mV) than aqueous electrolytes (~10mV) and short-circuit current (J_{sc}) of ~150μA with unfiltered light. However, when the UV light was filtered, the bR-SC produced a J_{sc} equal to that obtained in dark conditions, which indicates that bR is not producing any photocurrent in I^-/I_3^- ACN electrolyte. Furthermore, the bR lost its purple color after testing the device as shown in **Figure 5.11(b-c)**. Therefore, the bR seemed to not be photoelectrically active in the I^-/I_3^- ACN electrolyte, which can be attributed to the bleaching of the retinal, and the high R_{PA}. Therefore, the use of $[Fe(CN)_6]^{3-/4-}$ and HQ/BQ alternative mediators was compared to I^-/I_3^- acetonitrile electrolyte.
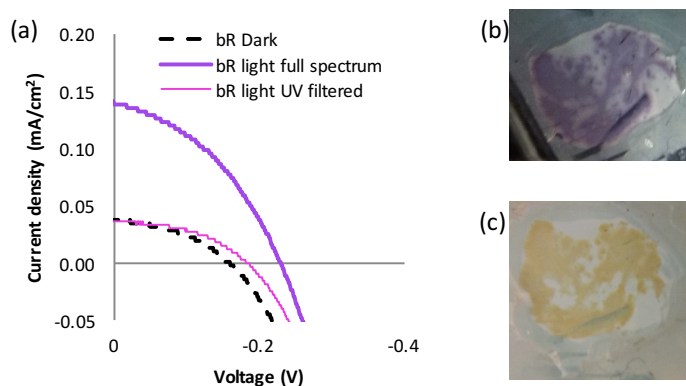
Figure 5.11. (a) Linear sweep voltammetry curve for purple membrane bR-SC with I^-/I_3^- in acetonitrile electrolyte. Photographs of bR-photoanode (a) before and (b) after testing the bR-SC

The cyclic voltammetry of I^-/I_3^- acetonitrile electrolyte is shown in **Figure 5.12(a)**, displaying two redox reactions, described by Equations 1 and 2[76].

$3I^- \rightleftharpoons I_3^- + 2e^-$ Equation 1

$2I^- \rightleftharpoons I_2 + 2e^-$ Equation 2

For I^-/I_3^- acetonitrile electrolyte $E_{1/2,1}$=0.56 V vs NHE = -5 V vs vacuum, and $E_{1/2,2}$=1.14 V vs NHE = -5.58 V vs vacuum. The cyclic voltammetry of $[Fe(CN)_6]^{3-/4-}$ aqueous electrolyte is shown in **Figure 5.12(b)** and displays only one redox reaction, with $E_{1/2}$=0.439 V vs NHE= -4.88 V vs vacuum, which is consistent with literature[77].
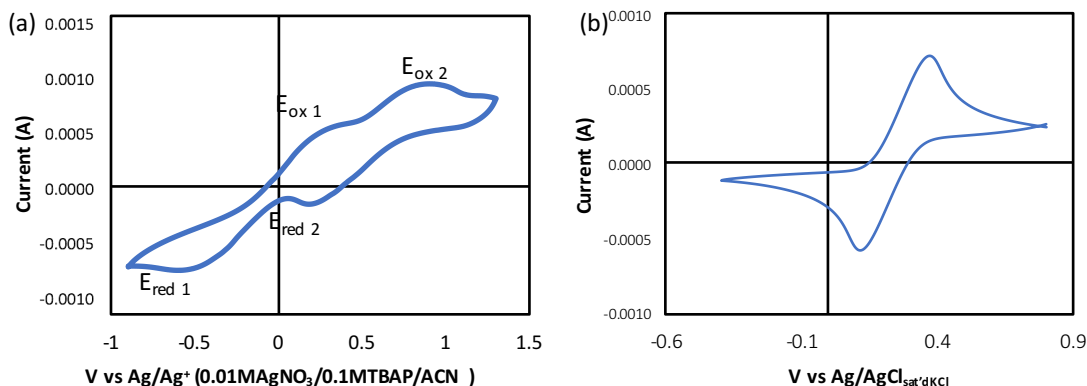
Figure 5.12. Cyclic voltammetry for (a) I^-/I_3^- acetonitrile electrolyte and (b) $[Fe(CN)_6]^{3-/4-}$ aqueous electrolyte

The electrocatalytic activity of platinum has been reported to be poor for HQ/BQ [55, 78]. Therefore, we compared graphite/FTO, PEDOT:PSS/FTO and Pt/Ti film by cyclic voltammetry in the HQ/BQ electrolyte in **Figure 5.13(a)**. The only material that produced REDOX peaks was the Pt film, but its non-faradaic current density was lower than the other materials. The electrochemical data from the CV is summarized in **Table 5.3.** The peak separation in Pt film ΔE=280 indicates non-reversibility of the reactions. Anionic intermediates of quinones can interact strongly by hydrogen bonding with other species, forming a quinhydrone-like complex (dimer) via strong hydrogen bonds and be adsorbed in the electrode surfaces[79, 80]. We increased the surface area of the Pt film by depositing Pt NPs on top, which maintained its electrocatalytic activity and increased the non-faradaic current. The number of Pt NPs layer optimization is shown in **Figure 5.13(b)**. As the number of Pt NPs layers applied was increased, the non-faradaic current increased, the peak separation became narrower, with a ΔE=135 for three layers, and a positive shift of the reduction potential E_{red} is observed, indicating improvement of the electrocatalytic properties for HQ/BQ system and a decrease of overpotential for BQ reduction, which is beneficial for its application as counter electrode in the HB/BQ bR-SC. For HQ/BQ electrolyte $E_{1/2}$=0.9V vs NHE= -5.3 V vs vacuum. The redox

potentials for the I^-/I_3^- ACN, $[Fe(CN)_6]^{3-/4-}$ and HQ/BQ electrolytes obtained by cyclic voltammetry are summarized with the energy levels of the materials in the bR-SCs in **Figure 5.14**. Good matching is predicted for the three mediators as donors, and the bR/ZnO acceptor, which is important for achieving molecular-wire behaviour[81].

Table 5.3. Electrochemical data of HQ/BQ acetonitrile electrolyte obtained by cyclic voltammetry

	Eox (mV vs NHE)	Ered (mV vs NHE)	E1/2 (mV vs NHE)	ΔE (mV)
Ref[55]	1256	715	985.5	541
Evap Pt	1025	745	885	280
PtNPs 1L	1015	706	861	309
PtNPs 2L	980	777	879	203
PtNPs 3L	965	830	898	135
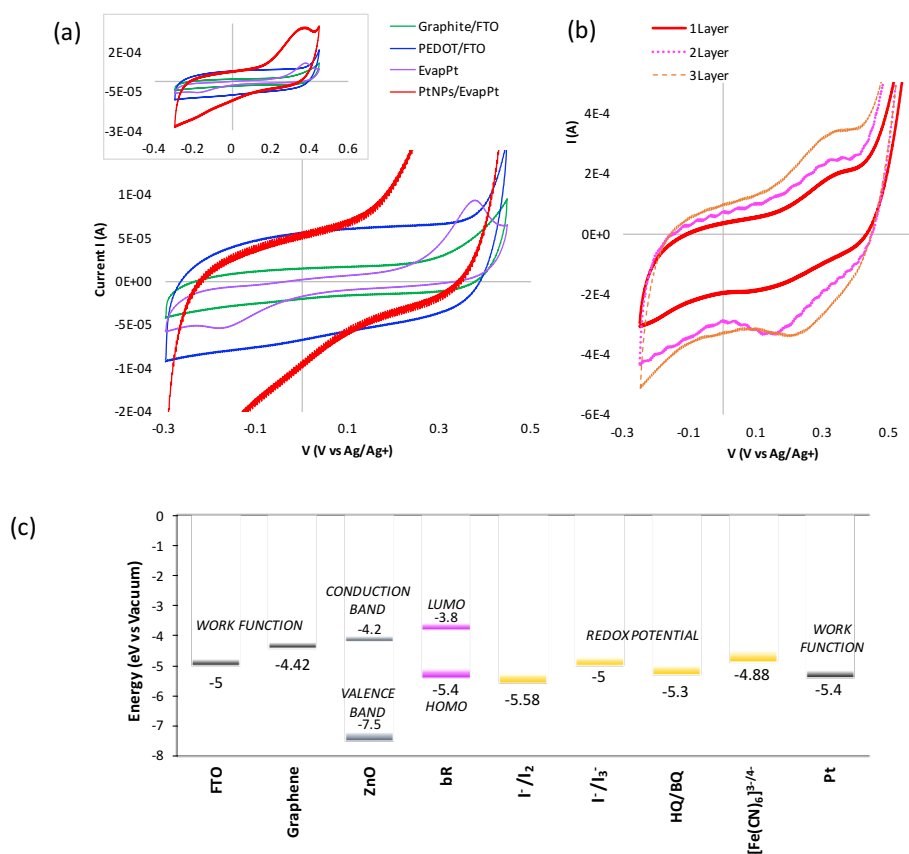
Figure 5.13. Cyclic voltammetry of HQ/BQ electrolyte using as electrodes (a) graphite/FTO, PEDOT:PSS/FTO, Pt film and 1-layer PtNPs/Ptfilm and (b) 1-, 2-, and 3-layer of Pt NPs on Pt film (c) Energy level alignment in the SC including the redox potential of I^-/I_3^- (ACN), $[Fe(CN)_6]^{3-/4-}$ and HQ/BQ mediators

The photovoltage produced with bR-SCs was compared to blank cells for each mediator in **Figure 5.14(a-c)**. For I^-/I_3^- the photovoltage was relatively high, ~200mV, but the addition of bR did not provide any additional photovoltage, indicating that bR is not performing a photoelectric function in the I^-/I_3^- ACN electrolyte. For the $[Fe(CN)_6]^{3-/4-}$, the photovoltage was slightly higher for the bR-SC compared to a blank cell, but the total photovoltage was low, ~10mV. Three order of magnitude faster recombination rates, but causes a positive shift of CB that counteract this effect (Duffy 2000). Substitution of the intrinsically slow two electron I^-/I_3^- redox couple with a one electron redox couple like $[Fe(CN)_6]^{3-/4}$ can increase recombination losses [50]. For the HQ/BQ, the photovoltage was relatively high for the blank cell, ~225mV, and even larger photovoltage was obtained for bR-SCs, ~275mV. Therefore, there is good energy alignment of the photoanode with HQ/BQ and the bR is performing a photoelectric function in this system.
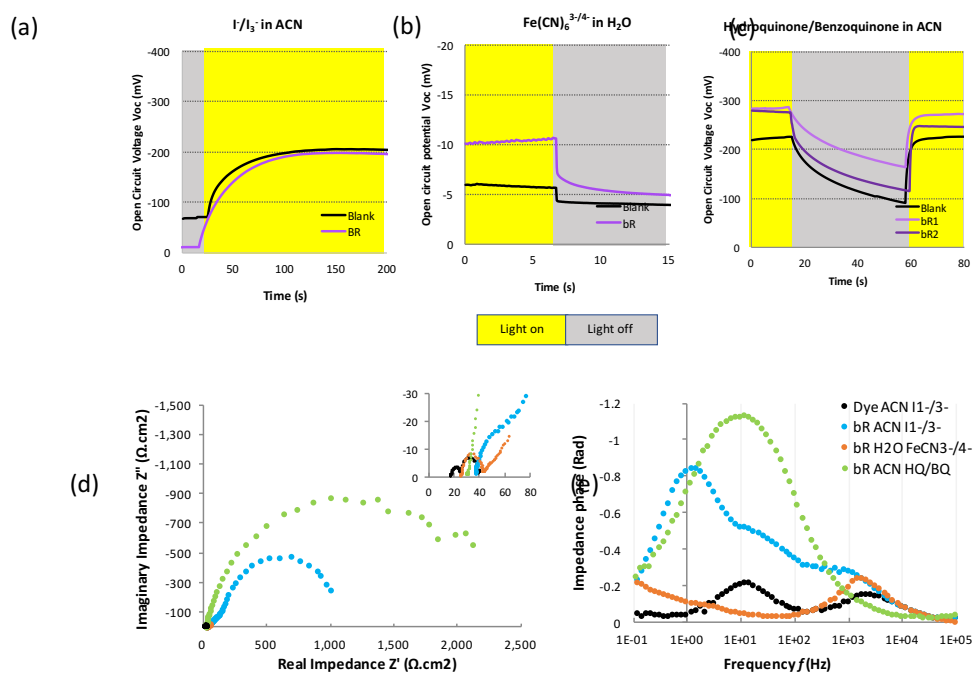
Figure 5.14. Photovoltage response of bR-SC and blank cells fabricated with different redox mediators (a) I^-/I_3^- (b) $[Fe(CN)_6]^{3-/4-}$ and (c) HQ/BQ. EIS (d) Nyquist and (e) Bode phase plot for Dye-SC and bR-SCs fabricated with I^-/I_3^-, $[Fe(CN)_6]^{3-/4-}$ and HQ/BQ mediators

The effect of redox mediator in the charge transfer at the bR-photoanode/electrolyte interface is analyzed with the EIS Nyquist and Bode phase plots of **Figure 5.14(d-e)**. $[Fe(CN)_6]^{3-/4-}$ does not display an

element of charge transfer in the medium-low frequency, which might be causing the low photovoltages observed. HQ/BQ resembled more the events of iodide/triiodide, but with higher R_{PA}. It has been reported that quinones reduce recombination resistance compared to $Co^{2+}/^{3+}$tris(bpy)reference electrolyte and down shift of conduction band of TiO_2[55].

5.3.4.   Effect of solvent composition and surfactant addition in the electrolyte

Different surfactants have been reported in aqueous SCs electrolyte to improve wettability of the hydrophobic nano-TiO_2. The addition of 0.1% Tween 20 to a dye-SC with aqueous $[Fe(CN)_6]^{3+/4+}$ electrolyte enabled the electrolyte to wet the hydrophobic TiO_2 dyed film and reproducible photovoltaic performance[50]. Cholic acid, also known as chenodeoxycholic acid, has been used as surfactant in dye-SCs and increased the efficiency by 30%[63, 82]. We compared the stability of a partially delipidated bR film dropcasted on glass towards four different surfactants: Tween 20, Triton X, PEG and sodium cholate, a salt of cholic acid, molecules illustrated in **Figure 5.15(a)**. The UV-Vis absorbance of the film before and after immersing it for 2hrs in a 2mM surfactant aqueous solution is shown in **Figure 5.15(b)**. The absorbance peaks of the aromatic aminoacids between 200-300nm and of the retinal at 550 nm are visible for all samples before immersing in the solution, but most of them vanish afterwards, except for sodium cholate. The normalized change of absorbance, $\Delta Abs/Abs_0$, given by Equation 1, for aromatic aminoacids and retinal peaks is summarized in **Figure 5.15(c)** for each surfactant solution and DI water. The absorbance decreased by almost 100% for DI water and tween 20 solutions, between 80-90% for Triton X, around 60% for PEG and only 10% for sodium cholate. The decrease in absorbance occurs for both aromatic aminoacids and retinal peaks indicating that the mechanism is not retinal bleaching, but caused by denaturing of the protein or deattachment of protein from the glass surface. The absorbance only remains stable after immersion in sodium cholate solution, even more stable than pure DI water. Sodium cholate may be filling up empty spaces on the hydrophobic glass and prevent hydrolysis of the bR-glass bond[26]. Therefore,

we selected sodium cholate as the optimum surfactant to improve the wettability of the electrolyte in the hydrophobic ZnO/FTO platform of the bR-SC.
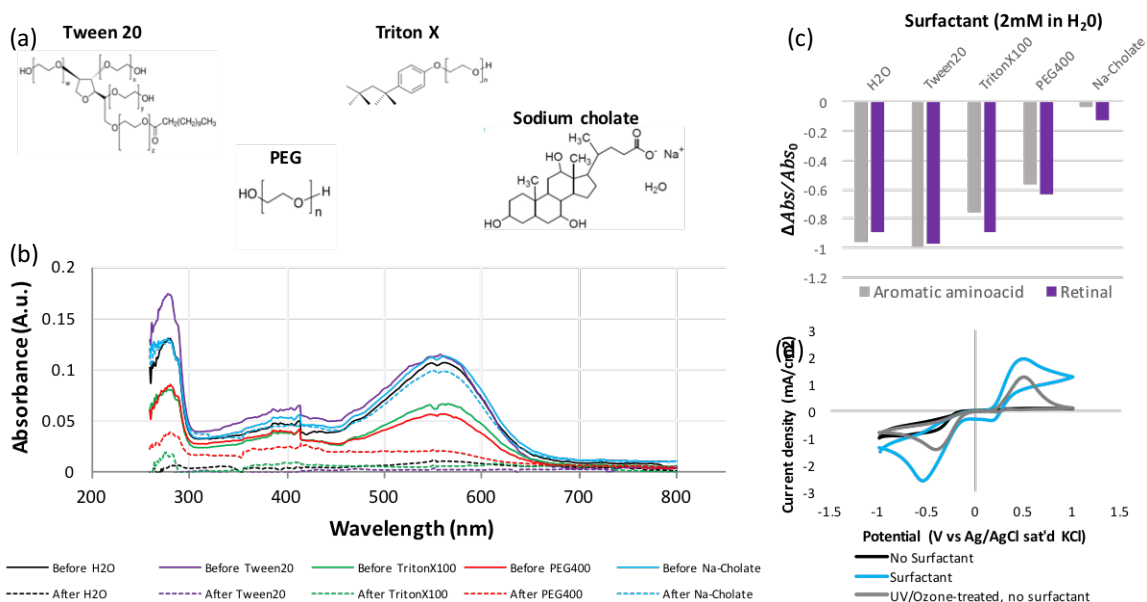
Figure 5.15. (a) Molecular structure of surfactants compared, (b) UV-Vis absorbance of delipidated D96N mutant bR before and after exposing to the surfactant solution, (c) bR film stability measured for each surfactant as ΔAbs /Abs_0 and (d) effect of surfactant addition in CV of ZnO/FTO photoanode in aqueous $[Fe(CN)_6]^{3-/4-}$ solution

To ensure that sodium cholate helps in the charge transfer efficiency between the photoanode and redox mediators in aqueous electrolyte we performed a cyclic voltammetry (CV) of a blank ZnO/FTO in aqueous $[Fe(CN)_6]^{3-/4-}$. The CV is shown for a non-treated electrode with and without surfactant, as well as for a UV/Ozone treated electrode without surfactant. When no surfactant is added and no treatment is applied, the current is very low, and no oxidation peak is observed. After adding the 2mM surfactant, the current increases and the redox peaks become well-defined. The surfactant addition outperforms UV-ozone treatment. UV/ozone treatment is temporal effect[83], and bR itself could make the electrode hydrophobic. The surfactant improves the wettability, therefore the charge transfer efficiency between the hydrophobic ZnO NPs and an aqueous electrolyte.

The effect of electrolyte solvent composition and addition of surfactant on bR-SC performance was studied with partially delipidated bR dropcasted on ZnO/FTO. The HQ/BQ electrolytes were prepared using

different solvent composition: dry ACN, ACN with 10% DI water (ACN-H2O) and ACN-H2O with 2mM sodium

cholate (ACN-H2O-NaCh). The blank and sensitized ZnO with partially delipidated bR of mutant D96N were

compared. The LSV and maximum power output (P_{max}) of each cell are depicted in **Figures 5.16(a-b)**. For

the dry ACN, the mutant bR produced larger J_{sc} and P_{max} than the blank. When 10% DI water was added to

the electrolyte, the J_{sc} and P_{max} was more than triplicated for both blank and D96N cells. When the

surfactant was added in 2 mM concentration the J_{sc} slightly decreased, but the fill factor was larger,

therefore the P_{max} increased slightly. bR-SCs fabricated with wild-type and D96N mutant bR showed very

similar LSV J_{sc}=0.1mA/cm^2 and P_{max}= 3 μW/cm^2. The performance of our bR/ZnO SC is similar to that first

reported for bR/TiO$_2$ SC[27] and much higher than solid-state devices and membrane-separated

photoelectrochemical cells. The ZnO in the electrode and the protons in the electrolyte increase the charge

separation life and prevent charge recombination as they act as successive energy gradients that quickly

shuttle electrons away from the excitation site to more stable sites[8].
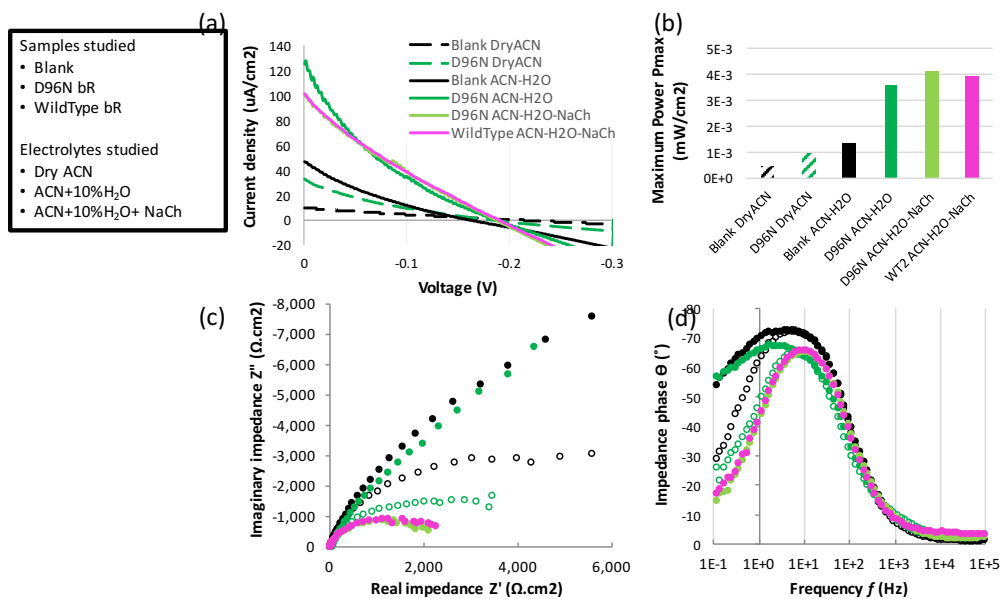
Figure 5.16. (a) LSV, (b) maximum power output, (c) EIS Nyquist and (d) Bode plots

The $R_{PA\ and}$ k_{PA} between the bR-photoanode and the HQ/BQ electrolyte were studied by EIS, and the

Nyquist and Bode plots for each cell are illustrated in **Figure 5.16 (c-d)**. The D96N bR-SC had smaller R_{PA} and

faster k_{PA} than the blank cell in dry ACN, demonstrating that the bR with HQ/BQ mediator is performing photo-induced electron transfer. When 10% water was added to the electrolyte (ACN-H2O), the bR-SC also showed lower R_{PA} than the blank, but the impedance for both blank and bR-SC increased, especially in the low frequency range, correlated to an increase in the Warburg diffusion impedance (W). After sodium cholate was added to the ACN-H2O electrolyte, the W was reduced, resulting in the smallest impedance semicircles in the Nyquist plots. The sodium cholate effectively improved the interface contact in the presence of water by increasing wettability of the electrolyte and diffusion of electroactive species, as it has been reported to help prevent adsorption of hydroquinone on the oxide surface[80]. No significant difference was observed between wild-type and D96N mutant bR-SCs in the EIS measurements, and the R_{PA} was effectively reduced to 2,000 Ω/cm^2 for HQ/BQ ACN electrolyte with water and surfactant.

The charge transfer mechanisms in non-aqueous media depend strongly on the presence or absence of proton donor/acceptors. In the absence of proton donor/acceptors, the hydroquinone undergoes two successive one-electron steps (**Figure 5.17(a)**). In the presence of proton donor/acceptors, the electron transfer process is coupled with the proton transfer processes (**Figure 5.18(b)**)[84, 85]. A hypothesis on the PCET processes taking place in the bR-SC with the HQ/BQ system is illustrated in **Figure 5.18(c)**. On the photoanode the HQ oxidizes to BQ and increase the local H^+ concentration, transferring electrons to the photoanode and protons to the retinal pumping process. The oxidized BQ diffuses to the counter electrode where it will converted back to HQ, resulting in a complete recycling process. The concentration asymmetry that the photon absorption initiates produces a photovoltage according to Equation 2, similar to the PCET mechanisms of photoelectrochemical devices proposed in literature [62, 86].

$$E = E^0 + \frac{RT}{2F}\ln\frac{[BQ][H^+]^2}{[HQ]}$$
\hspace{2cm} Equation 2
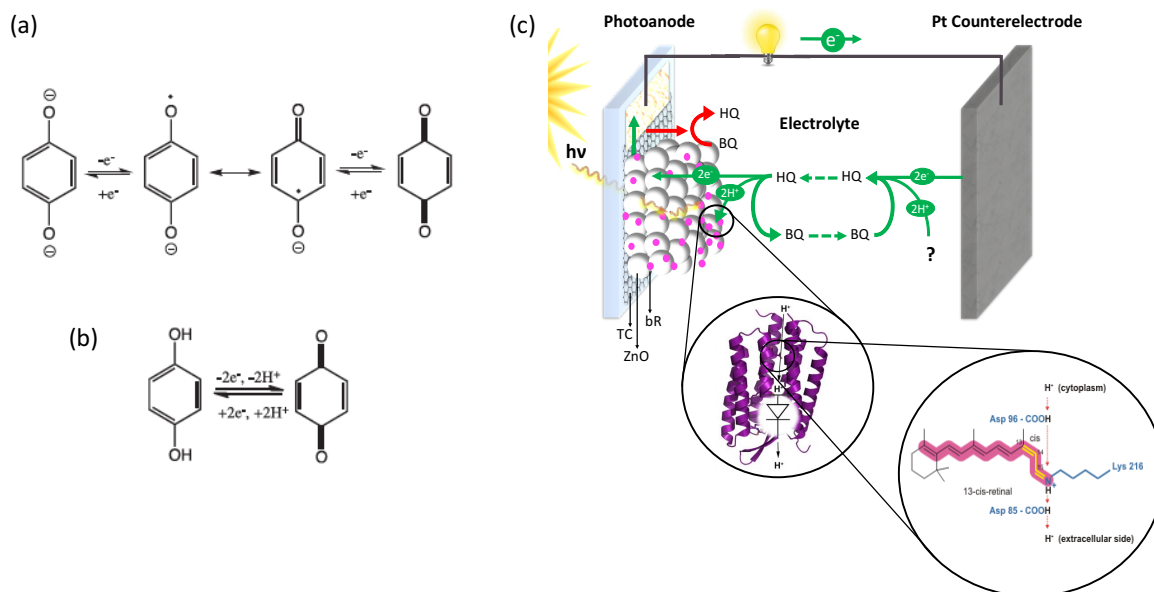
Figure 5.17. (a) Proton-coupled electron transfer in bR-SC using hydroquinone/benzoquinone redox system, (b) redox reactions for HQ/BQ system

5.4. Conclusions

The interfaces in a ZnO/bR/electrolyte were engineered for a bR-SC. Three different techniques were studied for purple membrane immobilization on a film of nanostructured ZnO. The EIS and LSV photoelectrochemical characterization of the bR-SCs reveal that the electrophoretic technique results in faster transfer rate of photoelectrons and photovoltage 12 times as high as dropcasting. The uniform orientation of the protein maximizes the sum of electrochemical gradient vectors. The chemical functionalization of ZnO with PTES increased the charge transfer resistance and reduced the transfer rate, acting as a dielectric layer. UV-Vis absorbance showed the characteristic absorption peaks of the bR retinal molecule immobilized on ZnO. SEM cross-section micrograph show a 1-3um thick purple membrane layer on top of the ZnO, not penetrating inside the pores. The charge transfer resistance at the ZnO/bR/electrolyte interface was in the order of 200,000 Ω/cm^2 in aqueous I^-/I_3^- electrolyte, therefore several approaches were explored to reduce it. The partial delipidation of bR improved the stability of bR

films and a more intimate contact with the ZnO, attributed to reduction of bR hydrophobicity and exposure of more functional groups from the bR aminoacid sequence for interacting with the oxide substrate. The $[Fe(CN)_6]^{3-/4-}$ and HQ/BQ redox pairs were investigated as alternatives to I^-/I_3^- due to their similarity to electron mediators in nature, good energy alignment with the bR/ZnO biophotoanode and they have been demonstrated for SCs in literature. HQ/BQ showed the largest bR-induced photovoltage for a total V_{oc} =275mV. Addition of 10% water, a proton donor, in the HQ/BQ ACN electrolyte triplicated the J_{sc} and P_{max} of the bR-SCs, indicating the possibility of PCET taking place. However, the water addition also increased the W electrolyte diffusion resistance in the hydrophobic surface of the electrode. Adding sodium-cholate as surfactant reduced the W and slightly increased the power generation. bR-SCs fabricated with wild-type and D96N mutant bR showed very similar LSV and EIS curves with J_{sc}=0.1mA/cm^2 and P_{max}= 3 μW/cm^2. The charge transfer resistance at the ZnO/bR/electrolyte interface was effectively reduced to 2,000 Ω/cm^2 in HQ/BQ ACN electrolyte with water and surfactant. The performance of our bR/ZnO SC is similar to that reported for bR/TiO$_2$ SC[27] and much higher than solid-state devices and membrane-separated photoelectrochemical cells. The ZnO in the electrode and the protons in the electrolyte increase the lifetime of charge separation and prevent charge recombination as they act as successive energy gradients that quickly shuttle electrons away from the excitation site to more stable sites.

5.5. Future work

In comparison to synthetic dyes, the cells reported in this investigation generate a relatively low power attributed to the high R_{PA} values. We will continue developing the design of a bR biophotovoltaic cell and exploring different approaches to improve its photoconversion efficiency. bR/TiO$_2$ SCs are reported to have higher power output than our cells, however they do not report for comparison the results for blank cells. We will study the new bR/quinone system using TiO$_2$ instead of ZnO to understand how does the semiconductor selection is affecting the performance. We will investigate quinone derivatives for lower

activation energy of charge and proton transfer at the ZnO/bR/electrolyte interface[55] as well as addition of other proton donor and acceptors and the immobilization of mediators in the electrode to overcome the limitations of diffusion[87]. We will use nanostructured ZnO with larger pores morphology that increases the bR/ZnO heterojunction area and a regular surface for homogeneous electrophoretic deposition. We will study other forms of covalent functionalization of the bR on the ZnO that can improve the control on the bR orientation with respect to the ZnO to improve the electrical wiring of the system[44, 81]. We will combine bR with other photoactive biomolecules and synthetic particles, like QDs, to capture a broader range of the solar spectrum and create low resistance electron and proton fast transfer pathways.

5.6. References

1.   Xie, X. J.; Bakker, E., Creating electrochemical gradients by light: from bio-inspired concepts to photoelectric conversion. *Physical Chemistry Chemical Physics* **2014,** *16* (37), 19781-19789.

2.   Meunier, C. F.; Yang, X. Y.; Rooke, J. C.; Su, B. L., Biofuel cells Based on the Immobilization of Photosynthetically Active Bioentities. *Chemcatchem* **2011,** *3* (3), 476-488.

3.   Hug, H.; Bader, M.; Mair, P.; Glatzel, T., Biophotovoltaics: Natural pigments in dye-sensitized solar cells. *Applied Energy* **2014,** *115*, 216-225.

4.   Sekar, N.; Ramasamy, R. P., Photosynthetic Energy Conversion: Recent Advances and Future Perspective. *Electrochemical Society Interface* **2015,** *24* (3), 67-73.

5.   Vázquez, R. S. *Influencia de la movilidad de las hélcies en la función de la bacteriorodopsina*; 2009; p 194.

6.   Wang, B. H.; Wang, D. J.; Fu, Z. Q.; Cui, Y.; Li, T. J., MODIFICATION AND PHOTOSENSITIZATION OF SIZE-QUANTIZED PARTICULATE CDS FILM PHOTOELECTRODES WITH BACTERIORHODOPSIN (BR). *Journal of Photochemistry and Photobiology a-Chemistry* **1995,** *90* (2-3), 167-170.

7.   Pandey, P. C., Bacteriorhodopsin - Novel biomolecule for nano devices. *Analytica Chimica Acta* **2006,** *568* (1-2), 47-56.

8.   LaVan, D. A.; Cha, J. N., Approaches for biological and biomimetic energy conversion. *Proceedings of the National Academy of Sciences of the United States of America* **2006,** *103* (14), 5251-5255.

9.   Reynolds, J. A.; Stoeckenius, W., MOLECULAR-WEIGHT OF BACTERIORHODOPSIN SOLUBILIZED IN TRITON X-100. *Proceedings of the National Academy of Sciences of the United States of America* **1977,** *74* (7), 2803-2804.

10.   Wagner, N. L.; Greco, J. A.; Ranaghan, M. J.; Birge, R. R., Directed evolution of bacteriorhodopsin for applications in bioelectronics. *Journal of the Royal Society Interface* **2013,** *10* (84).

11.   Tajkhorshid, E., Bacteriorhodopsin (bR) and the purple membrane. 2006.

12.   Geibel, S.; Loerinczi, E.; Bamberg, E.; Friedrich, T., Voltage Dependence of Proton Pumping by Bacteriorhodopsin Mutants with Altered Lifetime of the M Intermediate. *Plos One* **2013,** *8* (9).

13.   Li, L. S.; Xu, T.; Zhang, Y. J.; Jin, J.; Li, T. J.; Zou, B. S.; Wang, J. P., Photovoltaic characteristics of BR/p-silicon heterostructures using surface photovoltage spectroscopy. *Journal of Vacuum Science & Technology a-Vacuum Surfaces and Films* **2001,** *19* (4), 1037-1041.

14.   Chen, Z. P.; Lewis, A.; Takei, H. Y.; Nebenzahl, I., BACTERIORHODOPSIN ORIENTED IN POLYVINYL-ALCOHOL FILMS AS AN ERASABLE OPTICAL STORAGE MEDIUM. *Applied Optics* **1991,** *30* (35), 5188-5196.

15.   Alfinito, E.; Pousset, J.; Reggiani, L.; Lee, K., Photoreceptors for a light biotransducer: a comparative study of the electrical responses of two (type-1) opsins. *Nanotechnology* **2013,** *24* (39).

16.   Jin, Y.; Honig, T.; Ron, I.; Friedman, N.; Sheves, M.; Cahen, D., Bacteriorhodopsin as an electronic conduction medium for biomolecular electronics. *Chemical Society Reviews* **2008,** *37* (11), 2422-2432.

17.   Wang, W. W.; Knopf, G. K.; Bassi, A. S., Photoelectric properties of a detector based on dried bacteriorhodopsin film. *Biosensors & Bioelectronics* **2006,** *21* (7), 1309-1319.

18.   Collins, A. M.; Kaus, N. H. M.; Speranza, F.; Briscoe, W. H.; Rhinow, D.; Hampp, N.; Mann, S., Assembly of poly(methacrylate)/purple membrane lamellar nanocomposite films by intercalation and in situ polymerisation. *Journal of Materials Chemistry* **2010,** *20* (41), 9037-9041.

19.   Al-Aribe, K. M.; Knopf, G. K.; Bassi, A. S. In *Organic photovoltaic cells based on photoactive bacteriorhodopsin proteins*, Conference on Microfluidics, BioMEMS, and Medical Microsystems XI, San Francisco, CA, 2013
Feb 03-05; San Francisco, CA, 2013.

20.   Nicolini, C.; Erokhin, V.; Paddeu, S.; Sartore, M., Towards a light-addressable transducer bacteriorhodopsin-based. *Nanotechnology* **1998,** *9* (3), 223-227.

21.   Li-Kang, C.; Chun-Wan, Y.; El-Sayed, M. A., Bacteriorhodopsin-based photo-electrochemical cell. *Biosensors & Bioelectronics* **2010,** *26* (2), 620-6.

22.   Yen, C.-W.; Hayden, S. C.; Dreaden, E. C.; Szymanski, P.; El-Sayed, M. A., Tailoring Plasmonic and Electrostatic Field Effects To Maximize Solar Energy Conversion by Bacteriorhodopsin, the Other Natural Photosynthetic System. *Nano Letters* **2011,** *11* (9), 3821-3826.

23.   Miercke, L. J. W.; Ross, P. E.; Stroud, R. M.; Dratz, E. A., PURIFICATION OF BACTERIORHODOPSIN AND CHARACTERIZATION OF MATURE AND PARTIALLY PROCESSED FORMS. *Journal of Biological Chemistry* **1989,** *264* (13), 7531-7535.

24.   Lee, S. Y.; Chang, H. N.; Um, Y. S.; Hong, S. H., Bacteriorhodopsin production by cell recycle culture of Halobacterium halobium. *Biotechnology Letters* **1998,** *20* (8), 763-765.

25.   Roy-Mayhew, J. D.; Aksay, I. A., Graphene Materials and Their Use in Dye-Sensitized Solar Cells. *Chemical Reviews* **2014,** *114* (12), 6323-6348.

26.   Bella, F.; Gerbaldi, C.; Barolo, C.; Gratzel, M., Aqueous dye-sensitized solar cells. *Chemical Society Reviews* **2015,** *44* (11), 3431-3473.

27.   Thavasi, V.; Lazarova, T.; Filipek, S.; Kolinski, M.; Querol, E.; Kumar, A.; Ramakrishna, S.; Padros, E.; Renugopalakrishnan, V., Study on the Feasibility of Bacteriorhodopsin as Bio-Photosensitizer in Excitonic Solar Cell: A First Report. *Journal of Nanoscience and Nanotechnology* **2009,** *9* (3), 1679-1687.

28.   Allam, N. K.; Yen, C.-W.; Near, R. D.; El-Sayed, M. A., Bacteriorhodopsin/TiO2 nanotube arrays hybrid system for enhanced photoelectrochemical water splitting. *Energy & Environmental Science* **2011,** *4* (8), 2909-2914.

29.   Balasubramanian, S.; Wang, P.; Schaller, R. D.; Rajh, T.; Rozhkova, E. A., High-Performance Bioassisted Nanophotocatalyst for Hydrogen Production. *Nano Letters* **2013,** *13* (7), 3365-3371.

30.   Janfaza, S.; Molaeirad, A.; Mohamadpour, R.; Khayati, M.; Mehrvand, J., Efficient bio-nano hybrid solar cells via purple membrane as sensitizer. *BioNanoScience* **2014,** *4* (1), 6.

31.   Mohammadpour, R.; Janfaza, S., Efficient Nanostructured Biophotovoltaic Cell Based on Bacteriorhodopsin as Biophotosensitizer. *Acs Sustainable Chemistry & Engineering* **2015,** *3* (5), 809-813.

32.   Molaeirad, A.; Janfaza, S.; Karimi-Fard, A.; Mahyad, B., Photocurrent generation by adsorption of two main pigments of Halobacterium salinarum on TiO2 nanostructured electrode. *Biotechnology and Applied Biochemistry* **2015,** *62* (1), 121-125.

33.   Molaeirad, A.; Rezaeian, N., Oriented assembly of bacteriorhodopsin on ZnO nanostructured electrode for enhanced photocurrent generation. *Biotechnology and Applied Biochemistry* **2014**, 5.

34.   Naseri, N.; Janfaza, S.; Irani, R., Visible light switchable bR/TiO2 nanostructured photoanodes for bio-inspired solar energy conversion. *Rsc Advances* **2015,** *5* (24), 18642-18646.

35.   Chellamuthu, J.; Nagaraj, P.; Chidambaram, S. G.; Sambandam, A.; Muthupandian, A., Enhanced photocurrent generation in bacteriorhodopsin based bio-sensitized solar cells using gel electrolyte. *Journal of Photochemistry and Photobiology B-Biology* **2016,** *162*, 208-212.

36.   Renugopalakrishnan, V.; Barbiellini, B.; King, C.; Molinari, M.; Mochalov, K.; Sukhanova, A.; Nabiev, I.; Fojan, P.; Tuller, H. L.; Chin, M.; Somasundaran, P.; Padros, E.; Ramakrishna, S., Engineering a Robust Photovoltaic Device with Quantum Dots and Bacteriorhodopsin. *Journal of Physical Chemistry C* **2014,** *118* (30), 16710-16717.

37.   Barbiellini, B.; Das, S.; Renugopalakrishnan, V.; Somasundaran, P., Electromagnetic Field in Hybrid Quantum Plasmonic-Photonic Systems. *Condensed Matter* **2018,** *3* (2), 10.

38.   Pavithra, N.; Asiri, A. M.; Anandan, S., Fabrication of dye sensitized solar cell using gel polymer electrolytes consisting poly(ethylene oxide)-acetamide composite. *Journal of Power Sources* **2015,** *286*, 346-353.

39.   Juretic, D.; Zupanovic, P., Photosynthetic models with maximum entropy production in irreversible charge transfer steps. *Computational Biology and Chemistry* **2003,** *27* (6), 541-553.

40.   Willander, M.; Khun, K.; Ibupoto, Z. H., ZnO Based Potentiometric and Amperometric Nanosensors. *Journal of Nanoscience and Nanotechnology* **2014,** *14* (9), 6497-6508.

41.   Ibupoto, Z. H.; Jamal, N.; Khun, K.; Willander, M., Development of a disposable potentiometric antibody immobilized ZnO nanotubes based sensor for the detection of C-reactive protein. *Sensors and Actuators B-Chemical* **2012,** *166*, 809-814.

42.   Zhou, J.; Xu, N. S.; Wang, Z. L., Dissolving behavior and stability of ZnO wires in biofluids: A study on biodegradability and biocompatibility of ZnO nanostructures. *Advanced Materials* **2006,** *18* (18), 2432-+.

43.   Min, J. H.; Choi, H. G.; Choi, J. W.; Lee, W. H.; Kim, U. R., Photocurrent of bacteriorhodopsin films deposited by electrophoretic method. *Thin Solid Films* **1998,** *327*, 698-702.

44.   Koyama, K.; Yamaguchi, N.; Miyasaka, T., ANTIBODY-MEDIATED BACTERIORHODOPSIN ORIENTATION FOR MOLECULAR DEVICE ARCHITECTURES. *Science* **1994,** *265* (5173), 762-765.

45.   Topoglidis, E.; Cass, A. E. G.; O'Regan, B.; Durrant, J. R., Immobilisation and bioelectrochemistry of proteins on nanoporous TiO2 and ZnO films. *Journal of Electroanalytical Chemistry* **2001,** *517* (1-2), 20-27.

46.   Rezaeian, N.; Molaeirad, A.; Janfaza, S., Nano-bio Hybrid Material Based on Bacteriorhodopsin and ZnO for Bioelectronics Applications *International Journal of Bio-Inorganic Hybrid Nanomaterials* **2014,** *3* (4), 7.

47.   Molaeirad, A.; Rezaeian, N., Oriented assembly of bacteriorhodopsin on ZnO nanostructured electrode for enhanced photocurrent generation. *Biotechnology and Applied Biochemistry* **2015,** *62* (4), 489-493.

48.   Cheng, M.; Yang, X.; Li, S.; Wang, X.; Sun, L., Efficient dye-sensitized solar cells based on an iodine-free electrolyte using L-cysteine/L-cystine as a redox couple. *Energy & Environmental Science* **2012,** *5* (4), 6290-6293.

49.   Wang, M.; Chamberland, N.; Breau, L.; Moser, J.-E.; Humphry-Baker, R.; Marsan, B.; Zakeeruddin, S. M.; Grätzel, M., An organic redox electrolyte to rival triiodide/iodide in dye-sensitized solar cells. *Nature Chemistry* **2010,** *2* (5), 385.

50. Daeneke, T.; Uemura, Y.; Duffy, N. W.; Mozer, A. J.; Koumura, N.; Bach, U.; Spiccia, L., Aqueous Dye-Sensitized Solar Cell Electrolytes Based on the Ferricyanide-Ferrocyanide Redox Couple. *Advanced Materials* **2012,** *24* (9), 1222-1225.

51. Jr., K. W. F., A high efficiency single‐crystal CdSe photoelectrochemical solar cell and an associated loss mechanism. *Applied Physics Letters* **1998,** *40*, 275.

52. Kato, M.; Sato, H.; Yagi, I.; Sugiura, M., Bio-inorganic hybrid photoanodes of photosystem II and ferricyanide-intercalated layered double hydroxide for visible-light-driven water oxidation. *Electrochimica Acta* **2018,** *264*, 386-392.

53. Chen, G. P.; LeBlanc, G.; Jennings, G. K.; Cliffel, D. E., Effect of Redox Mediator on the Photo-Induced Current of a Photosystem I Modified Electrode. *Journal of the Electrochemical Society* **2013,** *160* (6), H315-H320.

54. Cheng, M.; Yang, X. C.; Zhang, F. G.; Zhao, J. H.; Sun, L. C., Efficient Dye-Sensitized Solar Cells Based on Hydroquinone/Benzoquinone as a Bioinspired Redox Couple. *Angewandte Chemie-International Edition* **2012,** *51* (39), 9896-9899.

55. Flores-Díaz, N.; Soto-Navarro, A.; Freitag, M.; Lamoureux, G.; Pineda, L. W., Neutral organic redox pairs based on sterically hindered hydroquinone/benzoquinone derivatives for dye-sensitized solar cells. *Solar Energy* **2018,** *167*, 76-83.

56. Katz, E. Y.; Shkuropatov, A. Y.; Shuvalov, V. A., ELECTROCHEMICAL APPROACH TO THE DEVELOPMENT OF A PHOTOELECTRODE ON THE BASIS OF PHOTOSYNTHETIC REACTION CENTERS. *Bioelectrochemistry and Bioenergetics* **1990,** *23* (3), 239-247.

57. Zaitsev, S. Y.; Solovyeva, D. O.; Nabiev, I. R., Nanobiohybrid structures based on the organized films of photosensitive membrane proteins. *Russian Chemical Reviews* **2014,** *83* (1), 38-81.

58. Yehezkeli, O.; Tel-Vered, R.; Wasserman, J.; Trifonov, A.; Michaeli, D.; Nechushtai, R.; Willner, I., Integrated photosystem II-based photo-bioelectrochemical cells. *Nature Communications* **2012,** *3*.

59. Woronowicz, K.; Ahmed, S.; Biradar, A. A.; Biradar, A. V.; Birnie, D. P., III; Asefa, T.; Niederman, R. A., Near-IR Absorbing Solar Cell Sensitized With Bacterial Photosynthetic Membranes. *Photochemistry and Photobiology* **2012,** *88* (6), 1467-1472.

60. Hvasanov, D.; Peterson, J. R.; Thordarson, P., Self-assembled light-driven photosynthetic-respiratory electron transport chain hybrid proton pump. *Chemical Science* **2013,** *4* (10), 3833-3838.

61. Mora, S. J.; Odella, E.; Moore, G. F.; Gust, D.; Moore, T. A.; Moore, A. L., Proton-Coupled Electron Transfer in Artificial Photosynthetic Systems. *Accounts of Chemical Research* **2018,** *51* (2), 445-453.

62. Xie, X. J.; Bakker, E., Photoelectric Conversion Based on Proton-Coupled Electron Transfer Reactions. *Journal of the American Chemical Society* **2014,** *136* (22), 7857-7860.

63. Murakami, T. N.; Saito, H.; Uegusa, S.; Kawashima, N.; Miyasaka, T., Water-based dye-sensitized solar cells: Interfacial activation of TiO2 mesopores in contact with aqueous electrolyte for efficiency development. *Chemistry Letters* **2003,** *32* (12), 1154-1155.

64. Pavlishchuk, V. V.; Addison, A. W., Conversion constants for redox potentials measured versus different reference electrodes in acetonitrile solutions at 25 degrees C. *Inorganica Chimica Acta* **2000,** *298* (1), 97-102.

65.		García-Hernández, C.; García-Cabezón, C.; Martín-Pedrosa, F.; De Saja, J. A.; Rodríguez-Méndez, M. L., Layered composites of PEDOT/PSS/nanoparticles and PEDOT/PSS/phthalocyanines as electron mediators for sensors and biosensors. *Beilstein J Nanotechnol* **2016,** *7*, 1948-59.

66.		Kern, R.; Sastrawan, R.; Ferber, J.; Stangl, R.; Luther, J., Modeling and interpretation of electrical impedance spectra of dye solar cells operated under open-circuit conditions. *Electrochimica Acta* **2002,** *47* (26), 4213-4225.

67.		Qing, W.; Moser, J. E.; Gratzel, M., Electrochemical impedance spectroscopic analysis of dye-sensitized solar cells. *Journal of Physical Chemistry B* **2005,** *109* (31), 14945-53.

68.		Sarker, S.; Ahammad, A. J. S.; Seo, H. W.; Kim, D. M., Electrochemical Impedance Spectra of Dye-Sensitized Solar Cells: Fundamentals and Spreadsheet Calculation. *International Journal of Photoenergy* **2014**.

69.		Allen, C. G.; Baker, D. J.; Albin, J. M.; Oertli, H. E.; Gillaspie, D. T.; Olson, D. C.; Furtak, T. E.; Collins, R. T., Surface Modification of ZnO Using Triethoxysilane-Based Molecules. *Langmuir* **2008,** *24* (23), 13393-13398.

70.		Jonghyun, S.; Pallab, B.; Jian, X.; Gyorgy, V., *Optics Letters* **2004,** *29* (19).

71.		Wei. Wei, W.; George K, K.; Amarjeet S, B., Photoelectric properties of a detector based on dried bacteriorhodopsin film. *Biosensors and Bioelectronics* **2005,** *21*, 1309-1319.

72.		Gulikkrzywicki, T.; Seigneuret, M.; Rigaud, J. L., MONOMER-OLIGOMER EQUILIBRIUM OF BACTERIORHODOPSIN IN RECONSTITUTED PROTEOLIPOSOMES - A FREEZE-FRACTURE ELECTRON-MICROSCOPE STUDY. *Journal of Biological Chemistry* **1987,** *262* (32), 15580-15588.

73.		Peters, R.; Cherry, R. J., LATERAL AND ROTATIONAL DIFFUSION OF BACTERIORHODOPSIN IN LIPID BILAYERS - EXPERIMENTAL TEST OF THE SAFFMAN-DELBRUCK EQUATIONS. *Proceedings of the National Academy of Sciences of the United States of America-Biological Sciences* **1982,** *79* (14), 4317-4321.

74.		Law, M.; Greene, L. E.; Johnson, J. C.; Saykally, R.; Yang, P. D., Nanowire dye-sensitized solar cells. *Nature Materials* **2005,** *4* (6), 455-459.

75.		Reda, T.; Plugge, C. M.; Abram, N. J.; Hirst, J., Reversible interconversion of carbon dioxide and formate by an electroactive enzyme. *Proceedings of the National Academy of Sciences of the United States of America* **2008,** *105* (31), 10654-10658.

76.		Boschloo, G.; Hagfeldt, A., Characteristics of the Iodide/Triiodide Redox Mediator in Dye-Sensitized Solar Cells. *Accounts of Chemical Research* **2009,** *42* (11), 1819-1826.

77.		Kolthoff, I. M.; Tomsicek, W. J., The oxidation potential of the system potassium ferrocyanide-potassium ferricyanide at various ionic strengths. *Journal of Physical Chemistry* **1935,** *39* (7), 945-954.

78.		Monge-Romero, I. C.; Suarez-Herrera, M. F., Electrocatalysis of the hydroquinone/benzoquinone redox couple at platinum electrodes covered by a thin film of poly(3,4-ethylenedioxythiophene). *Synthetic Metals* **2013,** *175*, 36-41.

79.		Zhu, X. Q.; Wang, C. H.; Liang, H., Scales of Oxidation Potentials, pK(a), and BDE of Various Hydroquinones and Catechols in DMSO. *Journal of Organic Chemistry* **2010,** *75* (21), 7240-7257.

80.		Uematsu, T.; Shimomura, E.; Torimoto, T.; Kuwabata, S., Evaluation of Surface Ligands on Semiconductor Nanoparticle Surfaces Using Electron Transfer to Redox Species. *Journal of Physical Chemistry C* **2016,** *120* (29), 16012-16023.

81.   Davis, W. B.; Svec, W. A.; Ratner, M. A.; Wasielewski, M. R., Molecular-wire behaviour in p-phenylenevinylene oligomers. *Nature* **1998,** *396* (6706), 60-63.

82.   Click, K. A.; Schockman, B. M.; Dilenschneider, J. T.; McCulloch, W. D.; Garrett, B. R.; Yu, Y. Z.; He, M. F.; Curtze, A. E.; Wu, Y. Y., Bilayer Dye Protected Aqueous Photocathodes for Tandem Dye-Sensitized Solar Cells. *Journal of Physical Chemistry C* **2017,** *121* (16), 8787-8795.

83.   Khranovskyy, V.; Ekblad, T.; Yakimova, R.; Hultman, L., Surface morphology effects on the light-controlled wettability of ZnO nanostructures. *Applied Surface Science* **2012,** *258* (20), 8146-8152.

84.   Guin , P. S.; Das, S.; Mandal , P. C., Electrochemical Reduction of Quinones in Different Media: A Review. *International Journal of Electrochemistry* **2011,** *2011* (816202), 22.

85.   Rafiee, M.; Nematollahi, D., Voltammetry of electroinactive species using quinone/hydroquinone redox: A known redox system viewed in a new perspective. *Electroanalysis* **2007,** *19* (13), 1382-1386.

86.   Megiatto, J. D.; Mendez-Hernandez, D. D.; Tejeda-Ferrari, M. E.; Teillout, A. L.; Llansola-Portoles, M. J.; Kodis, G.; Poluektov, O. G.; Rajh, T.; Mujica, V.; Groy, T. L.; Gust, D.; Moore, T. A.; Moore, A. L., A bioinspired redox relay that mimics radical interactions of the Tyr-His pairs of photosystem II. *Nature Chemistry* **2014,** *6* (5), 423-428.

87.   Choi, J. W.; Fujihira, M., Molecular-scale biophotodiode consisting of a green fluorescent protein/cytochrome c self-assembled heterolayer. *Applied Physics Letters* **2004,** *84* (12), 2187-2189.

Conclusions

Breakthroughs and Limitations in the Development of a Biophotovoltaic System Built from Renewable Carbon

The transition from current energy sources is a need for sustaining the development of our society and preventing an increase in global temperature. The substitution of fossil fuels with alternative energy sources does not necessarily reduce the emissions of greenhouse gases (GHGs), unless the technology is properly designed, using materials that are not only functional, but sustainable. In the case of photovoltaics, the use of silicon technology represents a large generation of GHGs due to the manufacturing of the silicon wafer. Other emerging technologies also required energy-intensive processes and non-abundant minerals. Considering that the negative impacts of PV technology are mainly derived from material selection and manufacturing processes, **new advanced technology that uses abundant, renewable and biodegradable materials, as well as cleaner processing, needs to be developed for the sustainable future of solar energy conversion**.

We have explored graphene as a transparent conductor (TC) for solar cells, a 2D nanomaterial that can be synthesized from renewable carbon sources. In the first chapter, we worked on the performance of graphene as TC. The graphene synthesis was optimized to produce large-area films of high conductivity, which must hold two characteristics: be mostly single-layer and have very large domain size (0.5mm). This is achieved by using copper substrates with 99.8% purity and 90ppm methane in Ar as precursor. We found that a relative low purity is necessary for nucleation of the graphene with such diluted carbon source. This single-layer graphene, however, is not conductive enough for use as TC. To solve this problem, we increased the material thickness, by stacking up this high-quality graphene films up to 4 layers (4LG), reducing the sheet resistance from 1000 Ω/ to 300 Ω/ .

The 4LG was compared to traditional FTO as TC for the photoanode in a model photovoltaic system, a dye-sensitized solar cell (DSC) made with ZnO nanoparticles (NPs). The results demonstrate that such 4LG can compete in performance with FTO for application as TC, yielding cells with the same power conversion efficiency, even though the thickness of 4LG was only 0.3% of the FTO thickness. 4LG is more transparent to all the solar spectrum resulting in cells with larger open circuit potential and short-circuit current. However, the sheet resistance of graphene resulted in internal losses for the graphene DSCs, demonstrated by a lower fill factor in comparison to FTO cells. Another important limitation of graphene is its chemical instability in oxidative environments, as we found that the ZnO/graphene hybrid had to be annealed (400˚C) in inert atmosphere, otherwise it would lose its condutivity. Replacing traditional tin oxides with graphene as TCs would allow to reduce the costs of raw materials, shrink the weight and thickness of the devices and mitigate the environmental and social impact of their production, while meeting industry's technical requirements to advance towards flexible portable devices. The approach of stacking high quality pristine CVD-graphene is promising to produce TCs for large scale applications, with higher $\sigma_{dc/op}$ than rGO or CNT, and lower cost than metal grids. Despite of this, two current technical aspects limit the further application of graphene as TC: (a) high sheet resistance and (b) tendency to oxidation at high temperatures in air.

In the second and third chapter, we explore electrodeposition on graphene as a method for its interfacing with the wide-bandgap semiconductor ZnO. The graphene-ZnO platform can be applied for a variety of photovoltaic devices configurations, including dye-, quantum dots- and bio-sensitized solar cells, organic-inorganic heterojunction cells, perovskites and furthermore. It can be fabricated on traditional glass substrates, but also on flexible polymer films which could reduce the volume and weight of the devices. We have effectively and reproducibly grown a continuous carpet of single-crystalline and highly texturized ZnO vertically-aligned nanorods (ZVNRs) *in situ* on graphene by electrodeposition. The graphene-ZVNRs heterostructure is characterized with a novel approach from the two sides of the interface formed between the 2D graphene and the 3D ZVNRs array to monitor the stability of the sp^2 carbon lattice in graphene

towards cathodic electrodeposition. The Raman shift spectra recorded from both sides of the junction demonstrate that the electrodeposition conditions prevent graphene oxidation and the sp^2 network remains intact. The method demonstrated for Raman spectroscopy of 2D-3D heterojunctions is recommended as a novel tool for characterization of heterojunctions with similar configurations.

In sensitized solar cells (SCs), having a large junction area of the graphene-ZnO platform with the hole acceptor is desirable for a high photocurrent generation. We observed that the smooth non-reactive surface of CVD-graphene delays nucleation, hindering the *in situ* growth of ZVNRs with very small diameter. Therefore, in the third chapter we further studied the experimental correlations between the ZVNR electrodeposition parameters and the corresponding performances of the heterostructure as a photo-electrode, with the objective of reducing the ZVNR diameters. The ZVNR film can be made more compact and dense by increasing temperature and time, to evenly cover the graphene surface and block recombination losses between electrocatalytic graphene and the electrolyte. However, the reduction of surface area when the film becomes more compact limits the photocurrent generated because of hindered light scattering. Non-stirred conditions promoted formation of longer conical rods and the use of a seed layer reduced the ZVNR diameter. These two variables together resulted in a greater surface to volume ratio of ZVNR, for improved light scattering and higher photocurrent generation, while retaining high photovoltage, for a total ten-fold improvement in power conversion. Finally, the use of seed layer further reduced the ZVNR diameter to ~80nm. Despite of these diameter reduction, the rod morphology resulted in low surface area and poor performance of the DSCs, compared to ZnONPs/graphene. The cathodic electrodeposition for *in situ* growth of crystalline materials like ZnO on graphene has several advantages, including relative fast deposition rates, low processing temperatures for use of polymeric flexible substrates, affordability, simplicity and more importantly, preservation of the sp^2 lattice of graphene. Alternative electrodeposition methods to fabricate ZnONPs/Graphene heterostructures is an interesting field of research to provide much higher surface area for better photovoltaic performance.

In chapter IV, the interfaces in a ZnO/bacteriorhodopsin/electrolyte were engineered for a bR-SC. Three different techniques were studied for purple membrane immobilization on a film of ZnO NPs. The photoelectrochemical characterization of the bR-SCs reveal that the bR film prepared by electrophoretic technique on ZnO results in faster transfer rate of photoelectrons and photovoltage 12 times as high as dropcasting, due to uniform orientation of the protein that maximizes the sum of electrochemical gradient vectors. In the meanwhile, the chemical functionalization of ZnO with PTES increased the charge transfer resistance and reduced the transfer rate, acting as a dielectric layer. The deposition of bR did not affect its photo-activity, but SEM cross-section micrographs show that bR does not penetrate inside the pores of the ZnO NPs film. The charge transfer resistance at the ZnO/bR/electrolyte interface was in the order of 200,000 Ω/cm^2 in aqueous I^-/I_3^- electrolyte, therefore several approaches were explored to reduce it. The partial delipidation of bR improved the stability of bR films and a more intimate contact with the ZnO, attributed to reduction of bR hydrophobicity and exposure of more functional groups in bR for interacting with the oxide substrate. The $[Fe(CN)_6]^{3-/4-}$ and HQ/BQ redox pairs were investigated as alternatives to I^-/I_3^- due to their similarity to electron mediators in nature, good energy alignment with the bR/ZnO biophotoanode and their previous demonstration for SCs in literature. HQ/BQ showed the largest bR-induced photovoltage for a total V_{oc} =275mV. Addition of 10% water, a proton donor, in the HQ/BQ ACN electrolyte triplicated the short-circuit current and power conversion efficiency of the bR-SCs, indicating the possibility of proton-coupled electron transfer taking place. However, the water addition also increased the electrolyte diffusion resistance (W) in the hydrophobic surface of the electrode. Adding sodium-cholate as surfactant reduced the W and slightly increased the power generation. bR-SCs fabricated with wild-type and D96N mutant bR showed very similar photoelectrochemical response, which was unexpected because the D96N mutant has slower photocycle than bR. The charge transfer resistance at the ZnO/bR/electrolyte interface was effectively reduced to 2,000 Ω/cm^2 in HQ/BQ ACN electrolyte with water and surfactant. The performance of our bR/ZnO SC is similar to that reported for bR/TiO$_2$ SC[26] and much higher than solid-state bR devices

and membrane-separated bR photoelectrochemical cells. The ZnO in the electrode and the protons in the electrolyte increase the lifetime of charge separation and prevent charge recombination as they act as successive energy gradients that quickly shuttle electrons away from the excitation site to more stable sites.

This dissertation has discussed the application of two carbon-based materials from renewable sources in the photoanode of solar cells: graphene and bacteriorhodopsin. Their technical feasibility to replace traditional materials like tin oxides, in the case of graphene, and synthetic dyes, in the case of bacteriorhodopsin, has been demonstrated. Carbon is an abundant material in the surface of our planet, in fact, the increase of concentration in the atmosphere has become a major concern due to the burning of fossil fuels. Further research in the field is required to overcome the limitations here identified, such as reduction of sheet resistance of graphene, development of methods for oxide deposition on graphene that do not require heat treatment and result in large surface area of the oxide and reduction of electron transfer resistance at the interface of electrolyte-bacteriorhodopsin-oxide. The research in this field will continue by the author, together with an interdisciplinary and international team of collaborators looking to finally achieve the goal of an efficient biophotovoltaic cell from renewable carbon fabricated with low-energy processes.